UNIVERSITY OF CALIFORNIA SAN DIEGO

Iron under Extreme Conditions:

Nano and Microstructural Effects

A dissertation submitted in partial satisfaction of the requirements for the degree

Doctor of Philosophy

in

Materials Science and Engineering

by

Gaia Righi

Committee in charge:

Professor Marc A. Meyers, Chair
Professor Farhat Beg
Professor Nicholas Boechler
Professor Javier Garay
Professor Vitali Nesterenko

2022

This dissertation of Gaia Righi is approved, and it is acceptable in quality and form for publication on microfilm and electronically.

University of California San Diego

2022

DEDICATION

To my mother and father.

Senza il vostro supporto non sarei mai arrivata dovo sono oggi.

TABLE OF CONTENTS

LIST OF FIGURES

LIST OF TABLES

ACKNOWLEDGEMENTS

This material is based upon work supported by the LLNL Academic Collaboration Team University Program (ACT-UP) award (subcontract B639114) and the Department of Energy, National Nuclear Security Administration under Award Number(s) DE-NA0003842. Part of this work was performed under the auspices of the U.S. Department of Energy by Lawrence Livermore National Laboratory under Contract DE-AC52-07NA27344. Part of this work was supported by DOE Office of Science, Fusion Energy Sciences under Contract No. DE-SC0021061: the LaserNetUS initiative at the Omega Laser Facility. Part of this work was performed at the Dynamic Compression Sector (DCS), which is operated by Washington State University under the U.S. Department of Energy (DOE)/National Nuclear Security Administration award no. DE-NA0003957. The DCS uses resources of the Advanced Photon Source; a DOE Office of Science User Facility operated for the DOE Office of Science by Argonne National Laboratory under contract no. DE-AC02-06CH11357.

We acknowledge the highly professional support team at the Jupiter Laser Facility at Lawrence Livermore National Laboratory, Dynamic Compression Sector at the Advanced Photon Source, National Ignition Facility at Lawrence Livermore National Laboratory, and Omega Laser Facility at the Laboratory for Laser Energetics. SEM and EBSD were conducted at the Nano3 User Facility and the Materials Research Center at the

University of California, San Diego (UCSD). We gratefully acknowledge computer resources form Livermore Computing.

I would like to thank Dr. Hye-Sook Park and Dr. Robert Rudd for their invaluable mentorship during my research work with LLNL; Dr. Carlos Ruestes on his guidance and contribution regarding molecular dynamics simulations; Dr. Camelia Stan, Dr. Suzanne Ali, Dr. Matt Hill, Dr. Richard Briggs, and Dr. Samantha Clarke for their counsel and instruction in my experimental work; Dr. Tom Lockard for his counsel and instruction in my computational work; and Dr. Marc Meyers for his guidance, mentorship, and the opportunity to fully engage in this fascinating work.

I am thankful for the advice of thesis committee members, Professor Farhat Beg, Professor Nicholas Boechler, Professor Javier Garay, and Professor Nesterenko.

Chapter 4, in part, is a reprint of material as it appears in: Righi, G., Ruestes, C. J., Stan, C. V., Ali, S. J., Rudd, R. E., Kawasaki, M., Park, H.-S., Meyers, M. A. Towards the ultimate strength of iron: spalling through laser shock. Acta Materialia 215 (2021). The dissertation author was the primary investigator and author of this paper.

Chapter 5, in part, is a reprint of material that is being prepared for publication: Righi, G., Briggs, R., Deluigi, O., Stan, C., Singh, S., Clarke, S., Bringa, E., Smith, R., Park, H.-S., Meyers, M. A. Spalling and x-ray diffraction in iron: a study of the ε-α reverse

phase transition. Physical Review B (2022). In prep. The dissertation author was the primary investigator and author of this paper.

Chapter 6, in part, is a reprint of material as it appears in: Righi, G., Lockard, T. E., Rudd, R. E., Meyers, M. A., Park, H.-S. Design of high-pressure iron Rayleigh-Taylor strength experiments for the National Ignition Facility. Journal of Applied Physics 131 (2022). The dissertation author was the primary investigator and author of this paper.

VITA

2017 Bachelor of Science, Materials Engineering, California Polytechnic State University

2018 Master of Science, Materials Science and Engineering, University of California San Diego

2022 Doctor of Philosophy, Materials Science and Engineering, University of California San Diego

PUBLICATIONS

Righi, G., Ruestes, C. J., Stan, C. V., Ali, S. J., Rudd, R. E., Kawasaki, M., Park, H.-S., Meyers, M. A. Towards the ultimate strength of iron: spalling through laser shock. Acta Materialia 215 (2021).

Righi, G., Lockard, T.E., Rudd, R.E., Meyers, M.A., Park, H.-S. Design of high-pressure iron Rayleigh-Taylor strength experiments for the National Ignition Facility. Journal of Applied Physics 131 145902 (2022).

Righi, G., Briggs, R., Deluigi, O., Stan, C., Singh, S., Clarke, S., Bringa, E., Smith, R., Park, H.-S., Meyers, M. A. Spalling and x-ray diffraction in iron: a study of the ε-α reverse phase transition. Physical Review B (2022). In prep.

ABSTRACT OF THE DISSERTATION

Iron under Extreme Conditions: Nano and Microstructural Effects

by

Gaia Righi

Doctor of Philosophy in Materials Science and Engineering

University of California San Diego 2022

Professor Marc A. Meyers, Chair

The role of microstructure on material properties is a foundational principle in materials science. The processing of a material will change its microstructure which, in turn, will change its properties. Understanding the strength of condensed matter at ultrahigh pressures and strain rates is challenging. The material's behavior changes unexpectedly and, in some conditions, may be surprisingly insensitive to the initial microstructure, which is contrary to the results of conventional static and quasi-static experiments. Therefore,

experiments are needed in these extreme regimes to better understand and model material properties. Iron is a largely used material in many applications but it is also relevant to geophysical phenomena. Accurately quantifying iron strength would aid in geophysical modeling of planet impact and formation, the understanding of more complex and relevant structural iron alloys, and fundamental material modeling at high strain rates. As a material, it is especially interesting in its pure form because it goes through phase transitions that change its mechanical properties. So, by understanding a relatively simple material like iron, one can begin to gain insight into more complex phase-changing materials that are more universally used.

Quasi-static and dynamic compression of iron was performed to determine microstructural effects on iron strength at various, increasing strain rates. Quasi-static compression strength experiments obey the well-known Hall-Petch relationship in which strength increases with decreasing grain size. Contrarily, the spall strength under dynamic compression increases with increasing grain size. This is due to spallation being a failure process that is dominated by defects. It has also been found that the timescale of the reverse phase transformation is only 8 ns and completes before spall. Preliminary results of iron strength under the highest pressures achievable suggest that it is higher than models are predicting and insensitive to initial microstructure. The high-pressure phase transformation in iron is thought to be a crucial factor in its high-pressure behavior. A measured reduction in grain size is thought to contribute to this microstructural insensitivity during compression. Hydrodynamic simulations are also used to design and predict results for these various high-pressure laser-driven experiments.

Chapter 1: Introduction

1.1 Motivation

Material behavior in extreme environments is of great importance for a variety of applications, including inertial confinement fusion (ICF), geophysical modelling, and other defense-related projects. In these circumstances, materials are subject to incredibly high pressures (500 GPa – 15,000 TPa) and temperatures (10,000 K – 40 million K) that fundamentally change their behavior. Additionally, space exploration programs have begun to grow, with SpaceX leading the way in commercial space flight and NASA recently landing the Mars rover, Perseverance. NASA also has missions to explore asteroids like Bennu, Psyche, and the Jupiter Trojans. In these applications it is even more crucial to accurately model and design spacecrafts based on our current knowledge of material strength under extreme conditions. Understanding the fundamental behavior of materials, especially for a commonly used metal like iron, will help advance many fields for the advancement of humankind.

It is necessary to fully understand material strength and failure at the extreme conditions experienced in situations like space travel, spallation, or meteorite and planet formation. The high-pressure strength of iron plays a role in the behavior of the many iron alloys that are used in these applications as well as planetary core formation. Iron is the major component of the Earth's solid inner core, of other terrestrial planets in our solar system, e.g., Mars, and even of exoplanets. Hence, determining the strength of iron at

extreme conditions is crucial to understand the rheology of the planetary core. The pressure, temperature conditions of 100 GPa and 1000 K – 3000 K are directly relevant to the Earth's core-mantle boundary as well as the Martian core. If iron under extreme pressure is inherently weak and easily susceptible to solid-state convection or flow, then core anisotropy may have manifested much earlier in Earth's history than previously thought. Understanding the onset and evolution of our geodynamo is intimately tied to inception and growth of the inner core as the liquid outer core cools and precipitates crystalline metal. The physical and chemical properties of the inner core for any terrestrial planet, particularly strength, are crucial for understanding how life could have evolved on Earth and for setting the stage for habitability on terrestrial exoplanets.

Failure at high strain rate is also a cause for concern in many applications such as ballistics and space travel. Under large tensile forces materials can fail through spallation, in which fragments are ejected from a surface at incredibly high velocity. Armor, tanks, and space shuttles need to be able to withstand the high velocity impact of projectiles or space particulate. Traditionally, flyer plates and gas guns are used to determine behavior during spall. These experimental methods provide a close comparison to low strain rate instances, but lasers are able to probe a higher strain rate regime that may more closely model more explosive events.

Micro-, nano-, and atomic structure is a fundamental aspect of material science and combined with processing, properties, and performance creates the Materials Paradigm.

The structure of a material, from the atomic to the macroscale, influences performance. At the atomic scale, the constituent atoms create the base structure that is repeated throughout a material which gives rise to much of its mechanical, electrical, and thermal properties. At the nanoscale, structural anomalies, or defects, begin to play a larger role in the material's macroscale properties. For example, dislocations are one of the primary defects at this length scale and they are present in almost all metals. Microstructure also plays an important role in a material's mechanical properties – grains are the main contributor to strengthening at ambient conditions. Grain boundaries are an integral part of the material structure-properties-processing-performance tetrahedron and need to be studied at various pressure-temperature conditions. Iron is a soft metal that undergoes phase transitions at high pressure and temperature. These structural changes lead to significant changes in both material microstructure and physical properties. So, scientifically, iron is also interesting to study because of its complex, evolving, structure that ultimately will change its behavior at different conditions.

1.2 Research Objective and Methodology

The objective to this research is to expand the knowledge on high-strain-rate behavior of iron. The extreme environment generated by laser shock compression changes the constitutive behavior of materials so it is important to understand both the failure and strength behavior of iron, a ubiquitous material in our modern age.

The goal is to address the following points:

1. What is the high-strain-rate spall behavior in iron?
    a. What are the grain size and strain rate effects in this extreme tension regime?
    b. How does the phase transition affect the failure behavior?
    c. What is the phase transition behavior upon release?
2. What is the high-pressure strength in iron?
    a. What is the strength of iron at Earth core conditions?
    b. Is there a grain size effect at this ultra-high pressure and temperature regime?
    c. How can we resolve discrepancies in previous experimental work?
3. How can iron strength measurements be used to validate and develop constitutive models?

Shock experiments are performed at various national laser facilities: Jupiter Laser Facility of Lawrence Livermore National Laboratory, Dynamic Compression Sector of the Advanced Photon Source, Omega Laser Facility at the Laboratory for Laser Energetics, and the National Ignition Facility of Lawrence Livermore National Laboratory. Experimental behavior of iron samples as quantified through various in-situ diagnostic techniques (VISAR, diffraction, radiography) in addition to post-shock characterization via Scanning Electron Microscopy and Electron Backscatter Diffraction. Shock experiments at the smaller laser facilities were used to investigate spall behavior in iron, including grain size effects on spall strength and phase transition timescale. Ramp compression

experiments at the larger facilities were conducted to determine iron strength at high pressures (>100 GPa), including the existence of temperature effects.

Chapter 2: Background

2.1 Iron

2.1.1 Properties

Iron is a lustrous grey transition metal with atomic number 26 (Fig. 2-1). In its pure form it is relatively weak and readily oxidizes so it is mostly used as an alloying element. Major properties of iron are listed in Table 2-1.

Figure 2-1. Pure iron chips, electrolytically refined and high purity (6N) 1 cm^3 iron cube [1].

Iron has at least four different crystal structures: α, γ, δ, and ϵ. The ambient phase, α, is body-centered cubic (BCC) but transforms to the face-centered cubic (FCC) phase (γ) at high temperatures (Fig. 2-2). There is a narrow high temperature range in which the δ

(BCC) phase is also stable. At high pressures, the ambient pressure phases transform to ϵ-Fe, which is hexagonal close-packed (HCP).

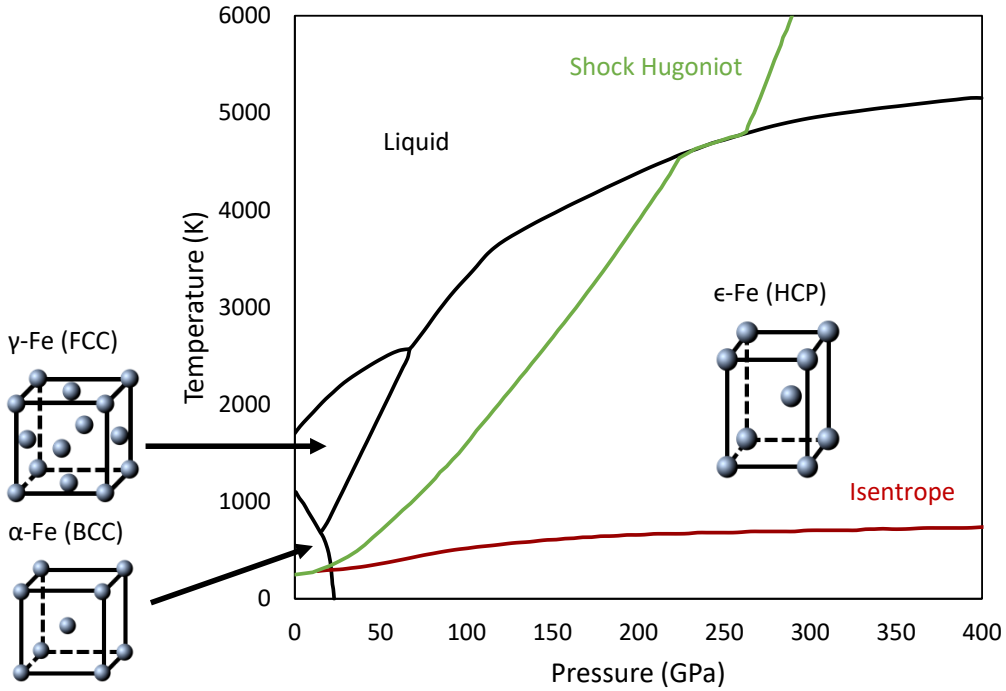

Figure 2-2. Iron pressure-temperature phase diagram showing isentrope and shock Hugoniot. Phases of iron are shown as representative unit cells. Not shown is small high-temperature δ-phase.

In the rare cases that pure iron is needed for an application, it can be produced by four different processes: vacuum treatment of liquid steel, electrolysis, conversion of iron to iron-carbonyls and subsequent dissociation, or conversion of iron to iron chloride and subsequent purification [2]. The majority of iron is used for alloying so modern industrial iron production uses blast furnaces to reduce iron ore into pig iron, which contains large

amounts of carbon [3]. Further processing of the pig iron to remove impurities produces the basis for all alloy steels.

Table 2-1. General properties of iron [1]

Physical Properties	
Density (g/cm^3)	7.874
Melting point (K)	1811
Mechanical Properties	
Elastic Modulus (GPa)	211
Shear Modulus (GPa)	82
Bulk Modulus (GPa)	170
Poisson ratio	2.91
Vickers Hardness (MPa)	608
Other	
Longitudinal sound speed (m/s)	5970
Thermal expansion coefficient (μm/m°C)	11.8
Thermal conductivity (W/mK)	80.4
Electrical resistivity (nΩm)	96.1
Crystal structures	α: Body-centered cubic ϵ: Hexagonal close-packed γ: Face-centered cubic δ: Body-centered cubic

2.1.2 Importance

In materials science, it is known that the dependence of iron strength on crystal orientation and polycrystalline texture is significant [4]. This type of anisotropic behavior is certainly not new to the field but can help inform on elastic constants and plasticity behavior at the proper pressure/temperature conditions in order to better understand the core anisotropy and constrain core dynamic models. Iron is also the basis for many commonly used structural materials like steels and high entropy alloys (Fig. 2-3) and by understanding its extreme behavior, one can begin to systematically investigate more complex ferritic materials at high pressure. Pure iron is used in lab settings or, commercially, in applications that take advantage of its magnetic properties, such as magnets, Magnetic Resonance Imagers, and electric motors [1]. Steels (iron plus up to 2 wt% carbon) are, by mass, the most used material [5]. Stainless steels are ubiquitous since their discovery in early 20^{th} century, now used in architectural applications, medical equipment, and consumer goods [6]. Stainless steels are iron-based alloys with chromium as well as other combinations of silicon, nickel, carbon, nitrogen, and manganese [6]. Cast iron is another popular category of iron alloy, with 2-6.7 wt% carbon and significant amount of silicon [5].

Figure 2-3. (a) Pure iron used in magnets. (b) Medium carbon steel used in main engine shafts and landing gear of airplanes [7]. (c) Stainless steel (A-218) used in main engine of space shuttles [8].

Iron also plays an important role in geophysical phenomena. The solid inner and liquid outer core of the Earth are primarily composed of iron with some nickel and trace light elements (Fig. 2-4a). The solid inner core was first discovered in 1936 by Inge Lehmann when seismology measurements were taken during an earthquake [9]. The strength of iron at core conditions is generally either ignored or extrapolated for geophysical modelling, but in reality, strength can influence core formation from planet-forming collisions (Fig. 2-4b). An accurate measure of iron strength can shed light on the structure of the inner core, which is thought to have a strong effect on core formation and geodynamo theory (a theory on how celestial bodies generate a magnetic field) [10]. The lattice preferred orientation (LPO) of the inner core is strongly influenced by the material's bulk properties and could have major consequences on core rheology [11]. The higher the iron strength, the longer the time required to form the LPO, possibly altering the timeline of Earth formation and biogenesis. There is no feasible way to directly probe core

conditions (360 GPa, 6000 K, 10^{-8} s^{-1}), however, laser-driven experiments are advantageous in that core pressure and temperature can simultaneously be achieved relatively easily. So, although the experiments described herein occur at much higher strain rates, the scarcity of benchmarks on iron strength in general drive these investigations that can provide any additional information on deformation behavior of iron at high pressure and temperature. Additionally, strength can influence the formation of metallic craters and meteorites. Iron is found in 5.7% of fallen meteorites [12] and Psyche, a large, highly metallic asteroid in the Main Belt, is thought to be the remnant core of a disrupted early planet [13]. Understanding the behavior of materials at these extreme conditions is crucial to understand these early planetary forming phenomena and planetary interiors in general.

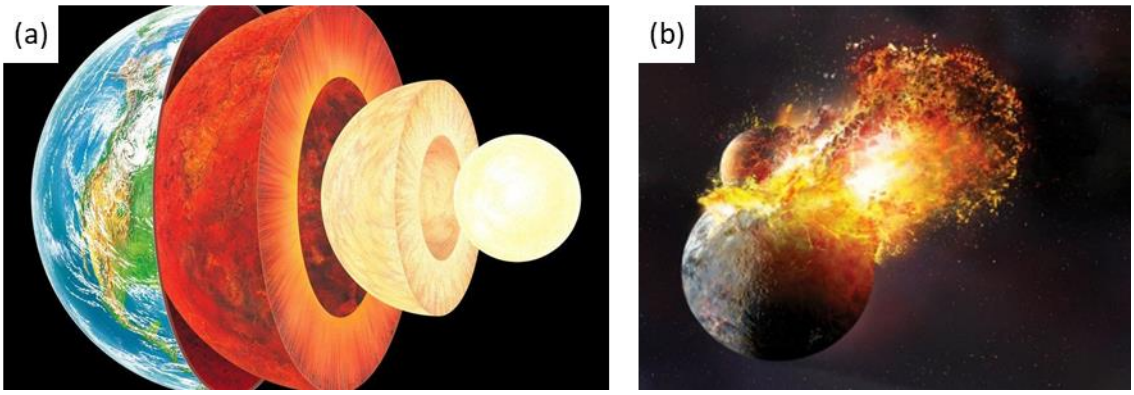

Figure 2-4. (a) The solid inner core and molten outer core are iron rich, with nickel and other trace elements [14]. (b) Model of possible moon-forming impact [15].

2.2 Shock

Shock compression is a useful tool to subject materials to extreme pressure (P) and temperature (T) environments. These ultra-high P-T conditions can be achieved using

explosive devices, Split-Pressure Hopkinson Bar, flyer plate impact, gas guns, and lasers (some of which will be discussed in Section 2.3). Shock waves have been studied throughout history, but one of the most important advancements was the development of a mathematical interpretation by Rankine and Hugoniot 150 years ago [16,17]. The formation of a shock wave in materials begins with the formation of a compressive wave after projectile impact, explosive detonation, or laser ablation. The compressive wave travels at the sound speed of the material causing particles near the wave to move at particle velocity, U_p. This also increases the internal energy near the wave front, consequently increasing sound speed as well [18]. If the wave velocity increases over time it can be assumed that this behavior can be modeled as a sequence of small velocity jumps. Each jump launches new compressive wave which is moving faster than the previous one because of the increase in sound speed. Over time, the later, faster compressive waves catch up to the earlier, slower ones causing the compressive waves to steeping into a shock wave (Fig. 2-5a).

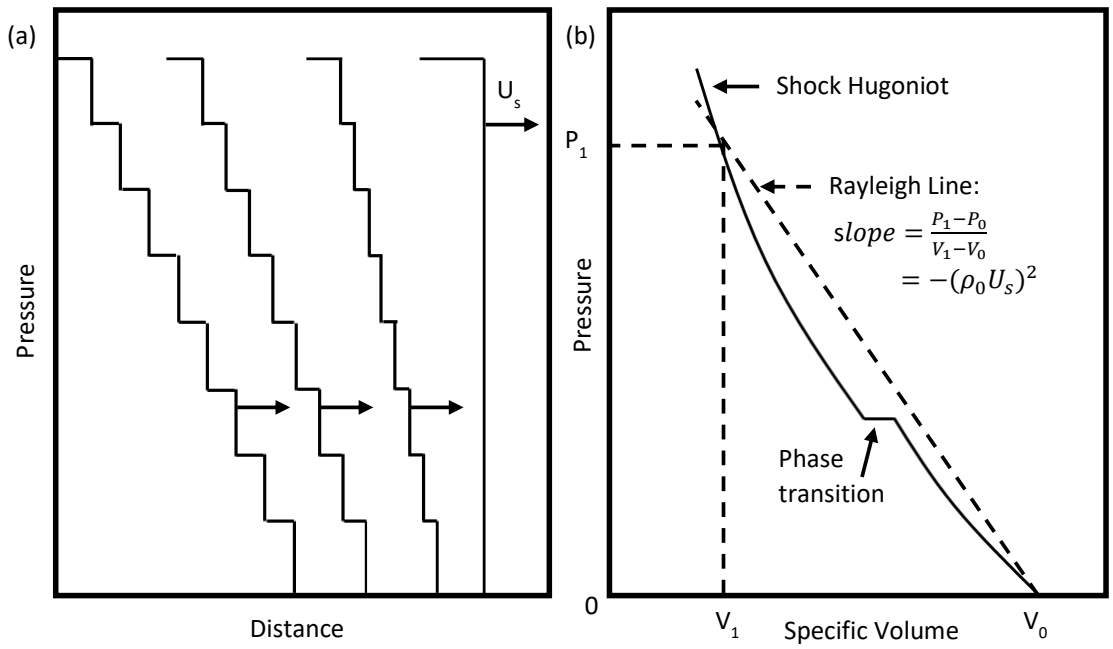

Figure 2-5. (a) Schematic of compressive waves steepening into a shock and (b) relationship between shock Hugoniot and Rayleigh line with a phase transition. Adapted from [19].

The Rankine Hugoniot equations for the shock conditions are based on the conservation of mass, momentum, and energy as follows [16,17]:

$$\rho_0 U_s = \rho(U_s - U_p) \tag{1}$$

$$P - P_0 = \rho_0 U_s U_p \tag{2}$$

$$E - E_0 = \frac{1}{2}(P + P_0)(V_0 - V) \tag{3}$$

where ρ is the density, U_s is the shock wave velocity, U_p is the particle velocity, P is pressure, V is volume, and E is energy. These three equations need to be combined with a fourth relationship to be able to fully solve the system [19]. The relationship between shock

velocity and particle velocity can be determined experimentally, and empirically tends to be described well by the Equation of State (EOS):

$$U_s = C_0 + S_1 U_p + S_2 U_p^2 + \cdots \tag{4}$$

where C_0 is the longitudinal sound speed and S_1 and S_2 are experimentally determined parameters. For metals, the expression can typically be truncated to the two-term linear form. If the initial conditions are known, Equations 1-4 can be solved for the series of points defining the Hugoniot (Fig. 2-5b). The Rankine-Hugoniot equations, particularly mass and momentum, hold well for regions infinitesimally close to the shock discontinuity, but are worth examining closer in moving further from the shock front [20]. This P-V curve is only a collection of all possible states, given a shock velocity where kinks in this curve can be due to elastic-to-plastic transitions, phase transformations, or other phenomena [19]. The bisector that connects initial and final states is known as the Rayleigh line and is considered to be the loading path for a given shock wave (Fig. 2-5b). A relationship between temperature and pressure at each point on the shock Hugoniot can be derived by means of the Grüneisen EOS and thermodynamic relationships [19]. The general solution is:

$$T = T_0 \exp\left[\left(\frac{\gamma_0}{V_0}\right)(V_0 - V)\right] + \frac{V_0 - V}{2C_v} P \tag{5}$$

$$+ \frac{\exp\left(-\frac{\gamma_0}{V_0} V\right)}{2C_v} \int_{V_0}^{V} P exp\left[\frac{\gamma_0}{V_0} V\right]\left[2 - \left(\frac{\gamma_0}{V_0}\right)(V_0 - V)\right] dV$$

where γ_0 is the Grüneisen parameter and C_v is the heat capacity at constant volume.

At the atomic scale, shock compression can be divided into multiple stages. As the first shock wave passes through the structure, the lattice rapidly compresses and experiences uniaxial strain that induces shear stresses in the structure. Then, like most materials, a yield point is reached and the lattice begins to deform plastically. During shock compression this point is called the Hugoniot Elastic Limit (HEL). As the material is now deforming plastically, twinning, shear bands, and phase transformations can occur. When the shock wave later reaches the back surface, release occurs in different modes depending on the difference in shock impedance. If the back surface is a free surface, where the shock wave releases into vacuum and shock impedance (the product of density and sound speed) is 0, spallation can occur. This will be described further in Section 2.4. If the shock wave moves into a material with lower shock impedance, the wave will slowly decay. If the second material has a higher shock impedance, the shock wave will reflect back into the first material, causing reshock. Reshock (or double-shock) experiments are a useful method to achieve a wide set of high pressures during shock compression.

Shock compression is a useful tool to reach incredibly high pressures, but materials will often melt before the desired final state is achieved. Thus, ramp compression needs to be used to reach similar high pressure at lower temperatures. Experiments using ramp compression need to be carefully designed through hydrodynamic simulations of unique pulse shapes or various target designs. The easiest way to ramp compress a material is to design a laser pulse shape that slowly increases the power. At the National Ignition Facility,

however, a ramp compression platform has been developed that uses an intense laser pulse and a reservoir-gap target configuration. A shock wave is formed after illumination of a layered reservoir and when this shock breaks out at the back side, it unloads across vacuum gap as a plasma flow [21]. This plasma stagnates on the far side of the gap, and it launches a ramp wave through the sample being studied. This ramped "plasma drive" allows the sample to be loaded quasi-isentropically, to pressures of many hundreds of GPa and sample temperature below ~1/3 of the melt temperature.

2.3 Dynamic Testing

2.3.1 Hopkinson Bar

The Hopkinson pressure bar was first developed in 1914 by Bertram Hopkinson in his work to measure pressure pulses produced by explosives [22]. This dynamic testing method is used to measure the stress-strain response of materials at strain rates of 10^2 s^{-1} – 10^4 s^{-1}. A specimen is sandwiched between two long bars, the incident and transmitter (Fig. 2-6a). The sample needs to be short enough that the stress can be considered to be uniformly distributed. When a projectile, the striker bar, impacts the incident bar it produces a stress wave. This elastic wave travels through the incident bar and reaches the specimen, which is plastically deformed as the wave travels through it and into the transmitter bar. The interaction of the wave with the specimen also produces complex reflections that propagate back into the incident bar. With strain gauges placed on the

incident and transmitter bars the signal of the pulse can be measured and be transformed into stress-strain plot.

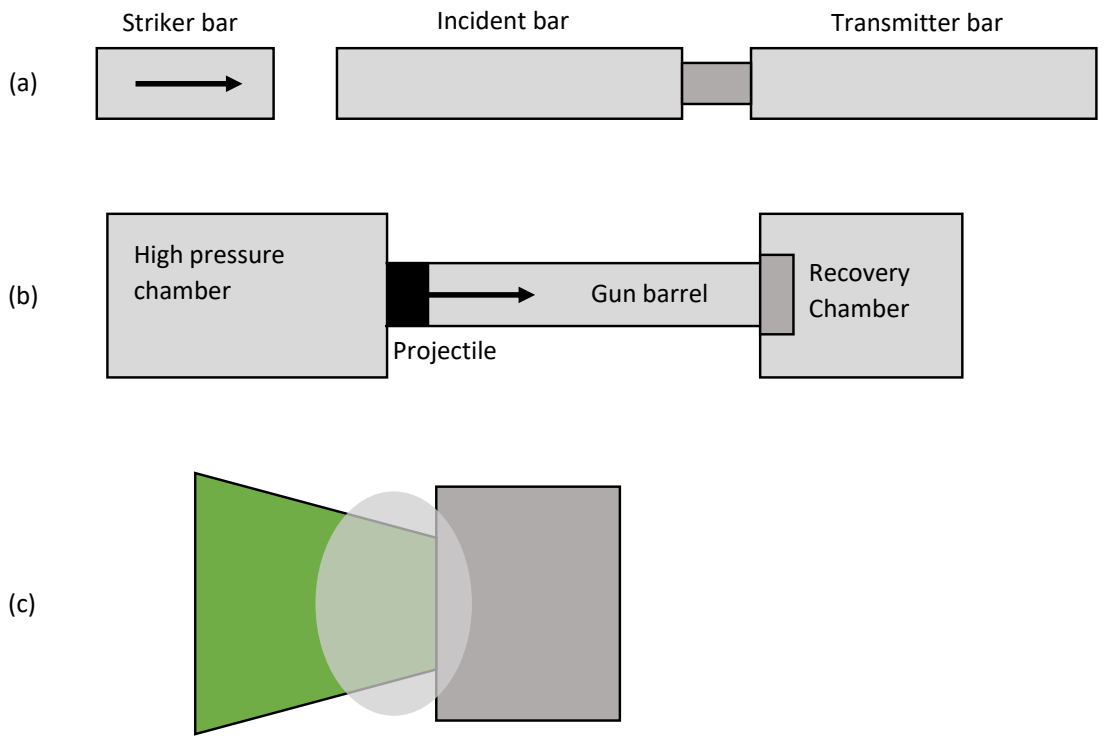

Figure 2-6. Schematic of (a) split Hopkinson pressure bar, (b) gas gun, and (c) laser induced shock compression.

2.3.2 Gas Guns

Gas gun systems have been used extensively to study materials at high pressures using planar shock pulses. Originally made as one-stage gas guns (Fig. 2-6b), their design was later improved by Crozier and Hume at the New Mexico School of Mines [19] to become two-stage gas guns. The dynamic behavior of materials can be studied at even higher strain rates: 10^4 s^{-1} – 10^6 s^{-1}. High-pressure gas is loaded in a chamber which, when

released, drives a projectile down a barrel. A two-stage gas gun works under the same principle, with the addition of a piston and further compressed air before the projectile. When the projectile hits the target, it produces a high-pressure shock wave that can be measured with a laser system.

2.3.3 Laser Shock

Laser shock-induced compression is another method of dynamic testing that can reach strain rates of 10^6 s^{-1} – 10^8 s^{-1}, higher than any other experimental technique. In this technique a laser beam is focused onto a sample such that when the energy is deposited onto the surface, it causes vaporization (Fig. 2-6c). The vapor pressure creates a pressure pulse to be transmitted into the sample. With sufficient input energy, extreme pressures (100's of GPa) and temperatures (1000's of K) can be easily achieved. There are many laser facilities in the world that are used to perform state-of-the-art science. The Jupiter Laser Facility (JLF) at Lawrence Livermore National Lab (LLNL) offers three lasers: Janus, Titan, and Comet. The Omega Laser Facility at the Laboratory for Laser Energetics in University of Rochester is a large-scale facility with two possible laser configurations. Lastly, the National Ignition Facility (NIF) at LLNL is the largest laser facility in the world, capable of reaching conditions similar to cores of stars and planets.

The Janus laser system (Fig. 2-7a) is a dual beam neodymium-glass laser in which each 1053 nm light laser beam can emit 1 kJ of energy in 1-20 ns pulse length [23]. VISAR and Streaked Optical Pyrometry (SOP) are available as diagnostics. The Titan laser system

(Fig. 2-7b) is also a dual beam laser in which one of the beams is shared with the Janus laser. The second beam is a short-pulse beam that provides up to 250 J energy in 1-10 ps. Lastly, Comet (Fig. 2-7c) has 4 beams that deliver up to 20 J of energy in extremely short pulses (0.5-6 ns). The large degree of flexibility and high shot rate makes JLF an extremely user-friendly system that produces great science.

Figure 2-7. Photos of the three laser systems at the Jupiter Laser Facility: (a) Janus, (b) Titan, and (c) Comet [23].

The Omega Laser facility is one of the more powerful laser facilities in the world. This high-energy UV laser system can deliver 30 kJ of energy using its 60 beams to a 1 mm sized target (Fig. 2-8a) [24]. Many years after the Omega laser was completed, a four-beam laser system, Omega EP, was created to perform short pulse laser shots (Fig. 2-8b). All four beams are frequency-tripled light (351 nm) and can provide up to 5 kJ of energy in long pulses (0.1-10 ns). Omega EP can also compress two of the four beams such that the 1053 nm light delivers up to 0.5 kJ in 0.7 ps, 1.25 kJ in 10 ps, or 2.3 kJ in 100 ps. The Omega Laser facility has a wide range of diagnostics for users, including VISAR, SOP, x-ray imaging, spectroscopy, and proton radiography. This user facility aims to conduct

research related to high-energy-density phenomena and perform experiments related to the National Inertial Confinement Program.

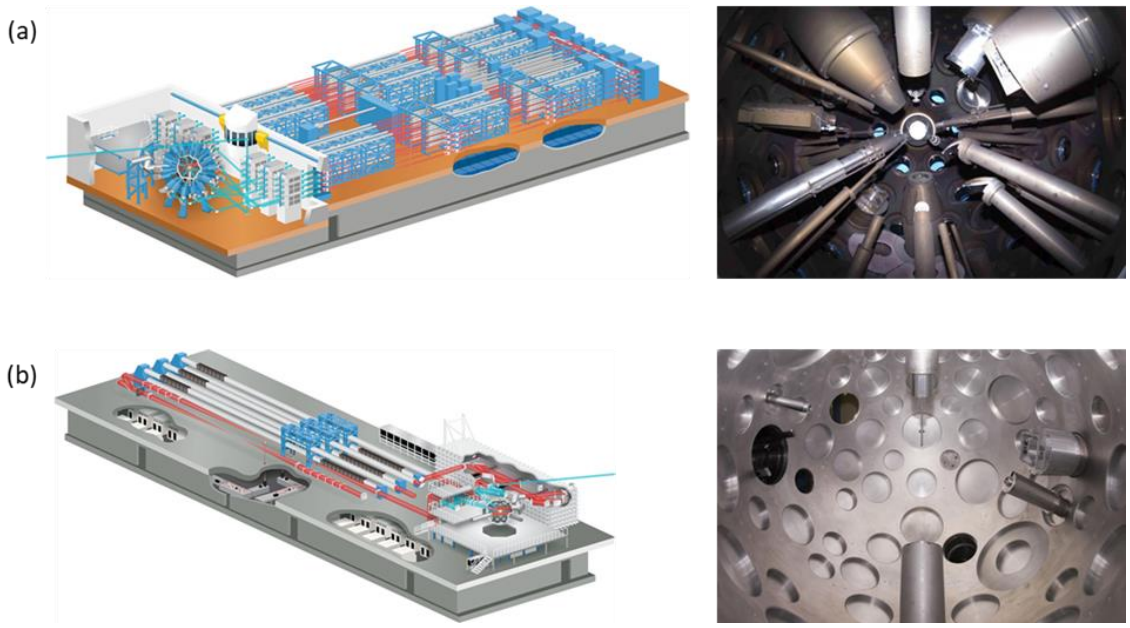

Figure 2-8. The Omega Laser Facility in Rochester is made up of (a) the Omega laser (60 beams) and (b) Omega EP (4 beams). (right) View of the target chamber center for each system [24].

The National Ignition Facility is the largest and most energetic laser in the world, built to achieve fusion ignition (Fig. 2-9) [25]. The NIF has 192 laser beams that can deliver up to 2 MJ of UV energy into the target for a few nanoseconds. This enormous system that contains over 30,000 optical components is housed in 10-story building the size of 3 football fields (Fig. 2-9). The incredibly powerful laser beams create conditions similar to those found in stellar and planetary cores as well inside exploding nuclear weapons. With research spanning from astrophysics to inertial confinement fusion, the NIF is leading the way in high-energy-density science. Just recently (August 2021) the NIF had a record-

setting inertial confinement fusion experiment. This scientific feat produced 1.35 million joules of energy – 70% of the energy put into the target. This breakthrough could not have happened without key improvements in the fields of experimental design, modeling, target fabrication, and laser beam quality.

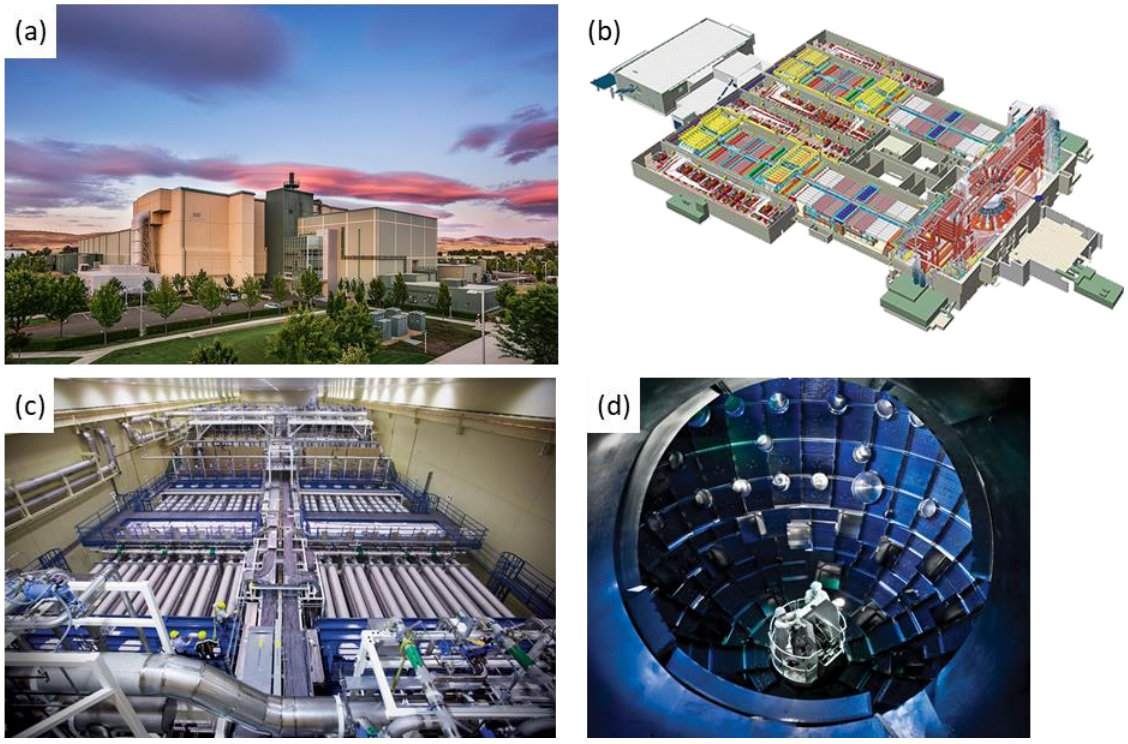

Figure 2-9. (a) Exterior of the National Ignition Facility as seen from the lab, (b) schematic of interior design, (c) photo of one of two identical laser bays that houses 2 clusters of 48 beamlines, and (d) interior of the target chamber [25].

X-ray light sources also provide the unique capability to perform in situ x-ray diffraction (XRD) during laser shock experiments. These can be performed at the Dynamic Compression Sector (DCS) at the Advance Photon Source (APS) in Argonne, Illinois or at the Matter in Extreme Conditions (MEC) instrument at the Linac Coherent Light Source

(LCLS) in Stanford, California. The APS is a synchrotron-radiation light source that provides ultra-bright, high-energy storage ring-generated x-ray beams [26]. The DCS is located in Sector 35 of the APS and focused on real-time x-ray diffraction, scattering, and imaging, of condensed matter phenomena under dynamic compression [27]. The laser shock station at DCS provides a 351 nm, 100 J laser with variable energy (30-90%). Their simultaneous line VISAR, point VISAR, and XRD diagnostic capabilities makes this facility ideal for probing phase transformations in materials at a large range of conditions. The MEC instrument provide both long (60 J in 10 ns) and short (1 J, 40 fs) pulse capabilities with a 527 nm light laser [28]. Their XRD capability from the hard x-rays of LCLS [29] along with the incredibly high shot rate make this facility extremely desirable for high energy density physics.

2.3.4 Diagnostics

There are a large number of diagnostics that can be used in conjunction with laser shock experiments but this section will focus on the three main diagnostics used in this research: VISAR, radiography, and x-ray diffraction. VISAR (Velocity Interferometry System For Any Reflector) is an optical tool designed to measure the velocity history of a reflecting surface [30]. An incident light beam is pointed onto a reflective surface and when the light is reflected, it contains the Doppler shift that results from the surface motion. The reflected part of the beam is recombined with the incident beam after it passes through an etalon which causes a delay with respect to the reflected beam (Fig. 2-10a). The amount of

delay is related to the etalon length. The resulting interference pattern is then observed by imaging it onto a streak camera, recording the phase as a function of time. The shock or particle velocity can then be determined as described by Celliers et al. [31].

Radiography is an imaging technique used in many fields, including medical and industrial uses. In high energy density physics, however, it is commonly used for instability growth measurements, implosion imaging, and as a fine structure probe (e.g. EXAFS). For materials science, the strength of materials under extreme conditions can be inferred through the measurement of Rayleigh-Taylor instability growth, as will be shown in Chapters 6 and 7. In these experiments, a subset of laser beams is used to illuminate a thin foil which causes the emission of x-rays [32] (Fig. 2-10b). The x-rays then interact with a shocked target through absorption or scattering principles and produce an x-ray image where the growth of pre-imposed ripples is measured and used to infer strength.

X-ray diffraction (XRD) is a non-destructive imaging technique used to probe material at the atomic level (Fig. 2-10c). In this technique the x-rays are reflected by planes of atoms according to Bragg's law [33]. XRD is most commonly used in static diamond anvil cell experiments since diffraction patterns can be taken at many increments in time for a long period of time. During laser shock experiments, generally only one diffraction pattern can be taken during an experiment due to the speed of shock waves. The development of time-resolved XRD for shock experiments is ongoing and will provide an incredibly unique capability to probe structural changes during dynamic compression.

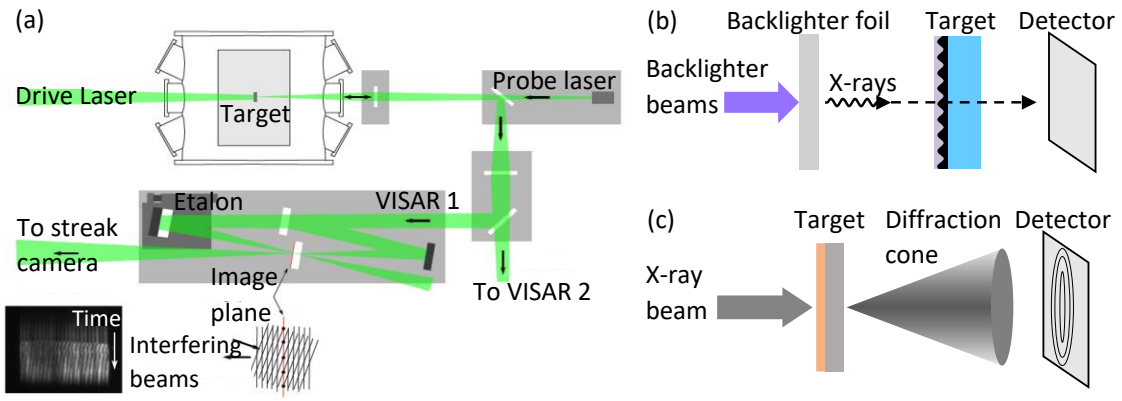

Figure 2-10. (a) Schematic of VISAR [34], (b) radiography and (c) diffraction concepts.

2.4 Spall

Spall is of interest for high velocity impact situations, for example in ballistics, geological events, or aerospace debris. In ballistics and aerospace applications, the impact of a projectile or debris to a surface or the ejection of material from a meteoritic impact crater can cause damaging spall [35–37]. So, in these processes of dynamic failure, it is crucial to understand material properties to effectively prepare for such events. Spall occurs from the interaction of stress waves during shock compression. When a pressure wave moves through a material, a free surface will cause wave reflection because of incompatible shock impedance (Fig. 2-11a). The incoming compressive wave and reflected wave will interact until a tensile wave is formed. This will lead to spall fracture when the stresses are of sufficient magnitude [19,38]. At positions x_1 and x_3, a compressive pulse is followed by a tensile pulse after some separation in time. At position x_2, however, the compressive pulse is immediately followed by the tensile pulse (Fig. 2-11b). The first region to

experience a tensile pulse (t_5 in Fig. 2-11a) is represented by the intersection of waves in Fig. 2-11b. The reality is that if the stresses are sufficient enough to cause spall, there will be additional release waves formed at the newly created internal surfaces, significantly complicating the x-t diagram.

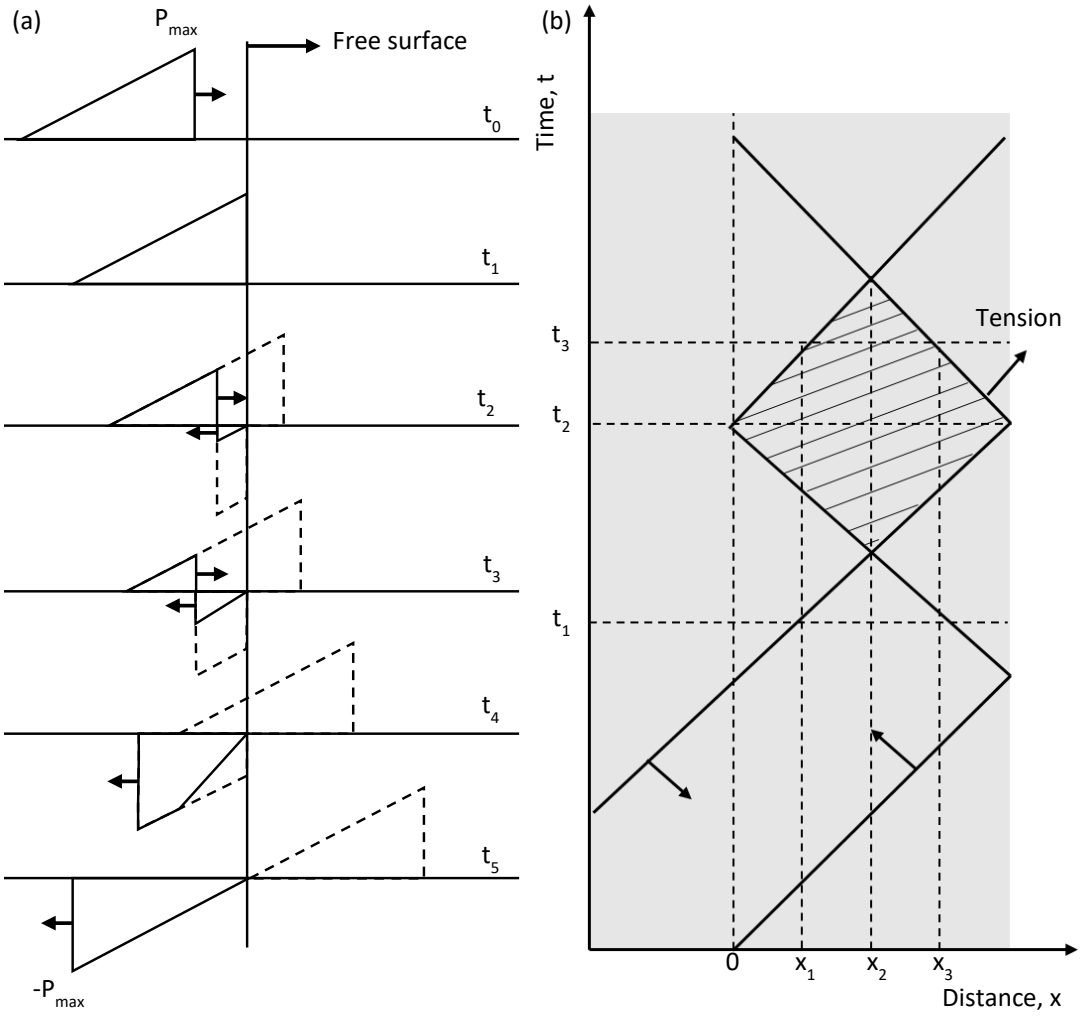

Figure 2-11. (a) Schematic of a triangular pulse shape traversing a sample until interaction with free surface causes reflection. (b) Distance-time plot showing propagation of waves in a target due to laser irradiation.

The velocity of the rear free surface (Fig. 2-12a) is used to determine spall properties like strain rate and spall strength. The ideal free surface velocity profile can be divided into five distinct parts (Fig. 2-12b). At point 1, the arrival of the first shock wave from laser irradiation is felt at the back of the sample and point 2 is the peak of that first wave. At point 3, the shock wave reaches the rear free surface and a rarefaction wave returns into the sample. This accelerates the rear surface of the sample to approximately double the velocity of the particles trailing the shock front. Once the waves interact and a tensile wave is formed, the velocity decreases, point 4. Finally, as spall occurs within the material, a second shock wave is formed which arrives at the rear surface and accelerates it once again, point 5. Shock and rarefactions waves travel between the spall plane and rear surface with decreasing amplitude, accelerating and decelerating the rear surface alternately, known as reverberations. The peak free surface velocity at point 3, u_{max}, and first minimum free surface velocity at point 5, u_{min} (also known as the spall pullback signal) in a simplified acoustic approach yields the following linear approximation relationship [38]

$$P_{spall} = (1/2)\rho_0 c(u_{max} - u_{min}) \tag{6}$$

where ρ_0 is the initial density and c is the sound velocity. The strain rates were calculated by applying the same acoustic approximation as follows

$$\dot{\epsilon} = \frac{(u_{max} - u_{min})}{\Delta t \times 2c} \tag{7}$$

where Δt is the time difference between u_{max} and u_{min}.

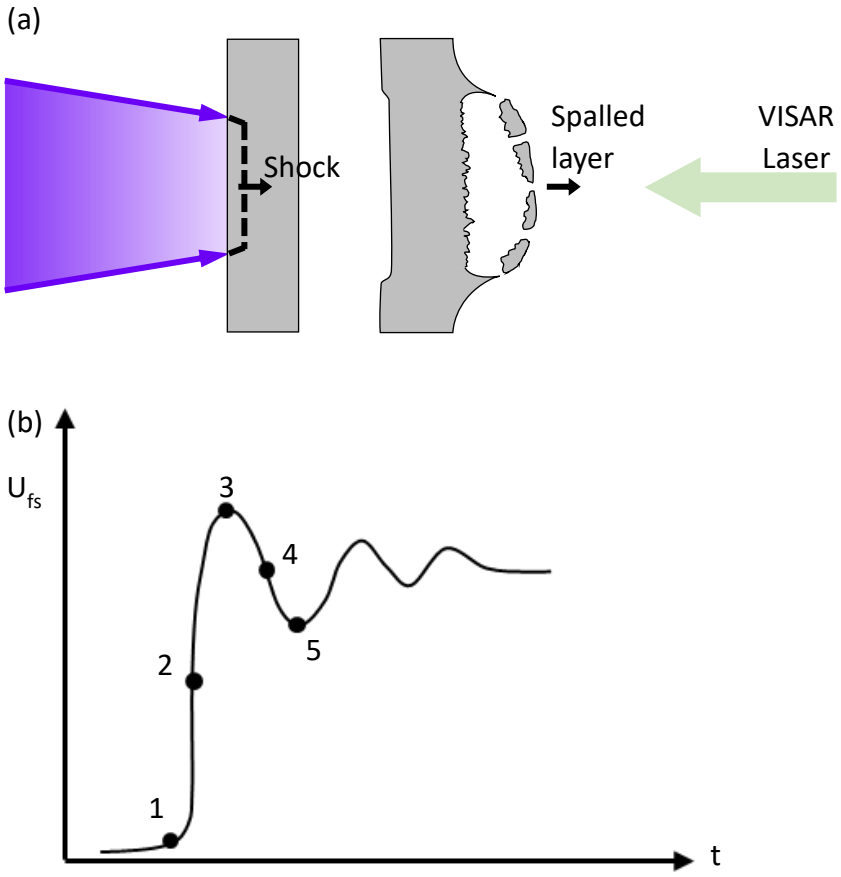

Figure 2-12. (a) Schematic of laser-induced spall fracture and (b) an ideal free surface velocity measurement at the rear surface of a metal upon spalling.

The formation of a spallation plane will occur if the tensile stresses are large enough such that internal cracks or voids form. In brittle solids, failure can be identified by smooth facets that are the result of the separation of atomic bonds along specific crystallographic planes (Fig. 2-13a). Fracture in ductile solids is characterized by a dimpled surface morphology that is the result of the nucleation, growth, and coalescence of voids (Fig. 2-13b).

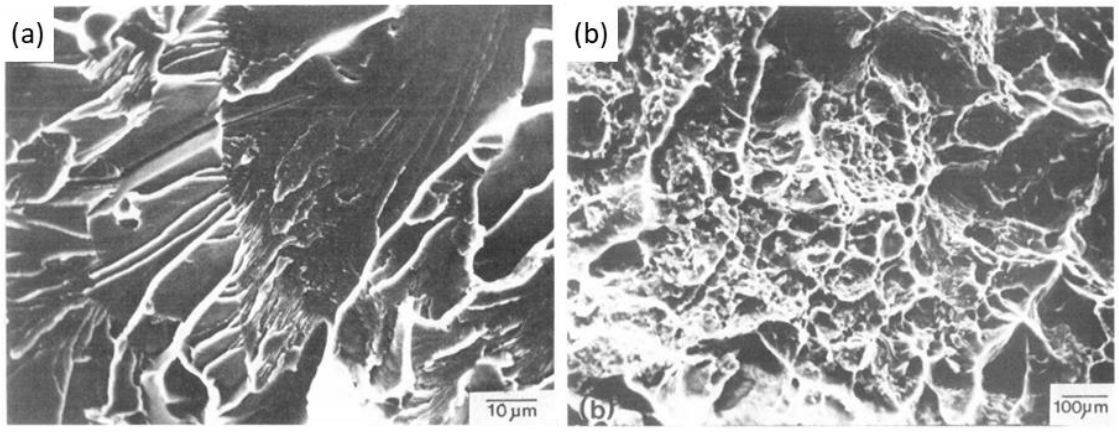

Figure 2-13. (a) Brittle failure in steel in Charpy impact test and (b) ductile failure in steel after tension test at 10^3 s^{-1} [39].

The formation of voids can occur from a variety of phenomena at different length scales (Fig. 2-14) [40–44]. At the atomic scale, intrinsic vacancy complexes can form nanoscale voids, although larger scale defects would dominate over such small-scale imperfections. Deformation-induced dislocation cell walls with a critical misorientation have large strain energy that can be relieved through void nucleation. At larger length scales twin and grain boundaries are common void initiation sites as their high interfacial energy and weak bonding allow for the preferential nucleation of voids. Second-phase particles or inclusions can cause cracks to propagate into the matrix material, which in turn can cause debonding of interfaces.

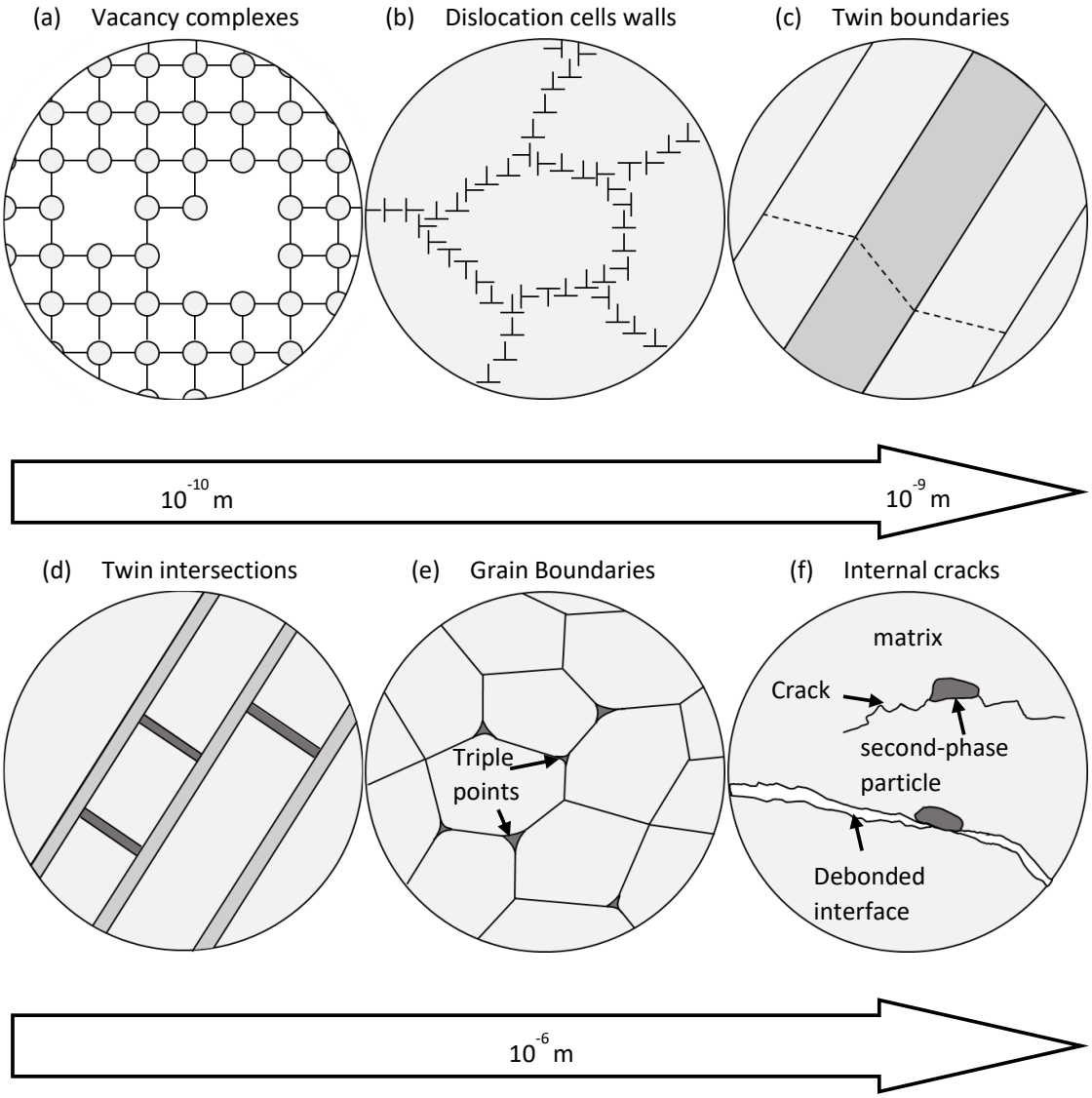

Figure 2-14. Hierarchy of void initiation sites. (a) Vacancy complexes such as di- and tri-vacancies, (b) dislocation cell walls, (c) twin boundaries, (d) twin interactions, (e) grain boundaries and triple points, (f) internal cracks and interface debonding at second-phase particles.

Void growth can be analytically modeled through the nucleation and propagation of geometrically necessary dislocations (GNDs) (Fig. 2-15). For every emitted dislocation loop, an incremental volume change, ΔV, is assumed such that a dislocation density can be

calculated. The high dislocation density results in increased shear stress in the vicinity of the void and consequently, increased temperature. Although this simplified analytical model may not capture other effects that may play a role in void nucleation and growth, the calculated temperature increase is similar to what is seen in MD simulations of iron spall. This will be discussed in further detail in Section 4.5.

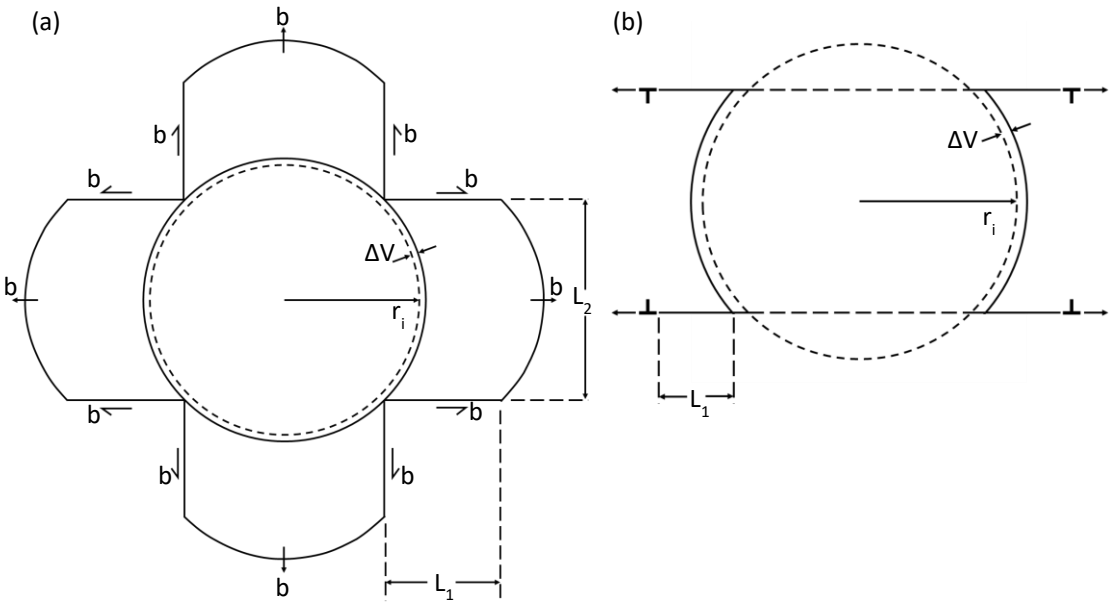

Figure 2-15. Schematic representation of void growth process via GND emission from (a) top and (b) side view. Initial void of radius r_i grows by ΔV after emission of several dislocations of Burgers vector, b.

It is well understood that iron undergoes an α to ϵ phase transformation at ~13 GPa during compression [45], but this phase change is also reversible; the ϵ to α change occurs during unloading at ~10 GPa [46–48]. This reversible phase transformation has also been linked to a change in spall morphology from rough to smooth spall [46,49]. Thin samples

that were transformed to ϵ-Fe were found to have smooth spall with dense twin distribution while thicker samples that remained mostly in the α phase showed brittle spall and a lack of twins. This was further investigated with MD simulations of nanocrystalline iron [50]. Simulation results using a phase-transforming potential show that after the ϵ-α phase transformation there is a much higher density of twins and a smoother spall surface while the phase-stable potential shows many cracks and rough spall. The formation of a substructure and twin boundaries resulting from the phase transformation provides more locations for void nucleation that eventually lead to ductile spall. In-situ diffraction experiments have reported a reduction in grain size, down to ~10 nm, during this shock-induced phase transformation [51]. Therefore, it is a possibility that the initial microstructure would have no effect on the spall strength. Other laser shock-induced spall experiments show that spall strength is higher in single crystal iron than in polycrystal iron [52], consistent with spall studies in various materials. In this study it was also found that single crystal iron has a ductile fracture surface while polycrystal iron spalls along grain boundaries. Ramp compression experiments in which spall occurred in polycrystalline iron found that spall strength increased at higher strain rates when compared to gas gun experiments [53]. Lastly, femtosecond laser shock pulses with thin films show increased spall strength compared to lower strain rate experiments, which agrees with the general trend of higher spall strength at higher strain rate (~10^8 s^{-1}) [54].

2.5 Diffraction

X-ray diffraction is a technique in which the length scale of an x-ray beam causes scattering at the atomic level. Laue diffraction relates to the scattering of waves due to diffraction by the crystal while Bragg diffraction gives the angles for coherent and incoherent scattering from a crystal lattice (Figure 2-16). The relationship between the interplanar distance, d_{hkl}, and the diffracted angle, θ, is Bragg's Law [55]:

$$n\lambda = 2d_{hkl}\sin(\theta) \tag{8}$$

where n is the diffraction order and λ is the x-ray wavelength. In perfect single crystal diffraction, the peaks will be sharp, but broadening at the full width half max will occur as the grain size, D, is reduced. With a monochromatic x-ray beam, this occurs in accordance to Scherrer's formula [56]:

$$B(2\theta) = \frac{K\lambda}{Dcos(\theta)} \tag{9}$$

where the broadening, B, as a function of 2θ, varies with a proportionality constant, K, the wavelength, and crystallite size, D. Without a monochromatic x-ray beam it is more complicated to determine the effects of grain size because peak broadening could occur from a reduction of the crystallite size or the broad range of energy of a "pink" beam. However, there are some methods that can be used to solve this issue. One is the modified Warren-Averbach analysis where a Fourier transform of the profile of a collection of diffraction peaks is used to extract the grain-size distribution and strain information used to determine material microstructure [57]. This has been implemented successfully with

laser-shocked iron by Hawreliak et al. [51]. A second, more recent, approach is implemented in a Rietveld refinement as published by Von Dreele et al. [58]. This technique is used in the diffraction campaign described in Chapter 5 to determine the order of grain refinement in laser shock and spalled iron.

Various information can be inferred from diffraction patterns. From the shift in the peak location, the pressure and temperature state can be found using published powder diffraction data files. Similarly, the lattice parameters of the unit cell can be adjusted and optimized for high pressure, laser shocked conditions. With certain experimental designs, the strain in the lattice can also be determined due to peak shifts. In a material that has a shock-induced phase transformation, like iron, the fraction of each phase can be measured by deconvolving the shocked diffraction pattern into its separate parts. Lastly, and most commonly, various phase paths can be determined, both solid-solid and solid-liquid transitions. Performing in-situ diffraction during lower strain rate experiments, like diamond anvil cells or gas guns, allows for studies on kinetics of phase transitions. Through laser shock experiments the phase behavior of materials under the highest pressures achievable can be established.

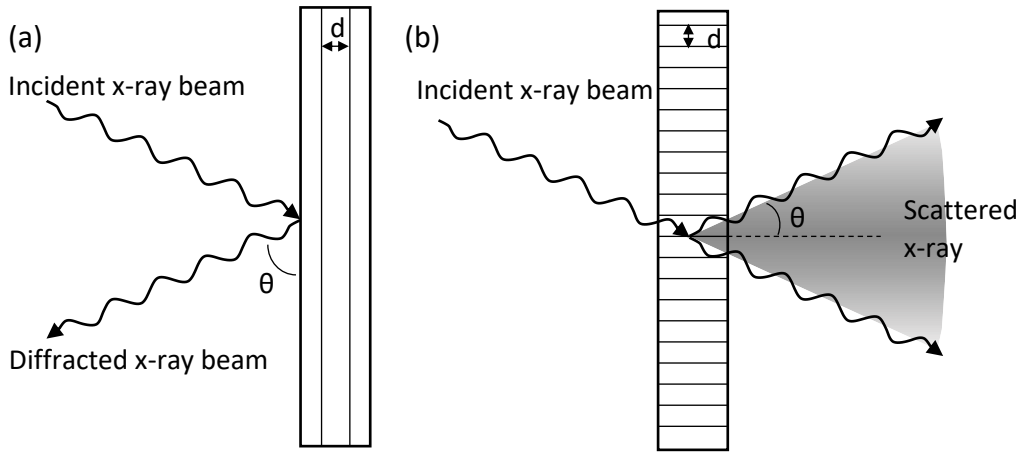

Figure 2-16. (a) Bragg and (b) Laue diffraction showing diffraction or scattering of incident x-ray beam, respectively.

2.6 Strength

In the most general terms, material deformation comes from the motion of dislocations. When a stress is applied, the atomic lattice begins to distort. At low levels, the lattice simply stretches or compresses and it can return to its original configuration. With increased stress, however, the lattice permanently shifts and a dislocation is formed (Fig. 2-17). With even more applied stress, that dislocation begins to move within the lattice, producing shear strain, and will eventually cause failure. The resistance to that motion is material strength. Dislocation motion can be slowed by a variety of methods. One method is the intrinsic resistance of the lattice structure to the distortion caused by moving dislocations. In metals, this does not have a large effect because metallic bonds have minimal directionality. In ceramics, however, the covalent and ionic bonds are much more resistant to deformation. To strengthen weak materials the structure must be altered

by introducing obstacles to dislocation motion; for example, through solid solution hardening, precipitation hardening, work hardening, or grain size hardening [59]. All of these methods are meant to stop dislocation motion to prevent premature failure. This work focuses on grain size hardening or grain boundary strengthening.

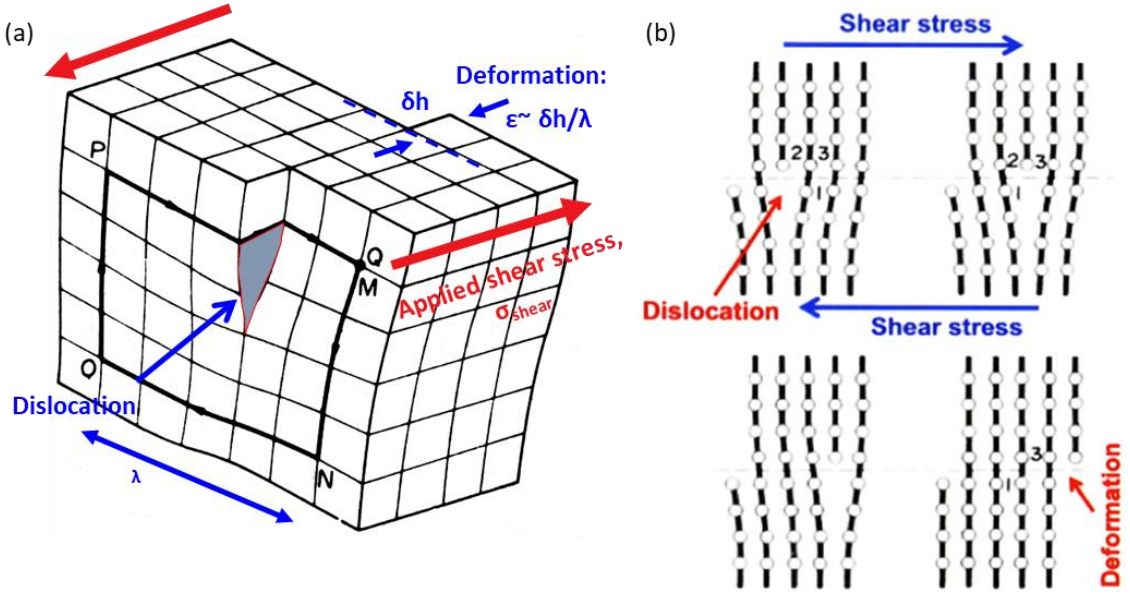

Figure 2-17. (a) Shear stress induced dislocation causes deformation. (b) Dislocation moving across atomic planes due to shear stress. Adapted from [60].

The strength of materials under an applied static stress is inversely proportional to grain size – the Hall-Petch effect [61]. This strengthening effect is the result of dislocations being arrested at grain boundaries, impeding any further propagation. Without the motion of dislocations, plasticity does not occur, and the yield strength increases as:

$$\sigma_y = \sigma_0 + \frac{k}{\sqrt{D}} \tag{10}$$

where σ_y is the yield stress, σ_0 is a materials constant for the starting stress for dislocation movement (or the resistance of the lattice to dislocation motion), k is the strengthening coefficient (a constant specific to each material), and D is the average grain size. For example, various Hall-Petch studies of iron show that the yield strength increases by a factor of 15 with the reduction of grain size (Fig. 2-18). During higher strain rate experiments, however, the behavior of dislocations and other strengthening mechanisms can be drastically different. There are many strength models that describe this higher strain rate behavior like Zerilli-Armstrong (ZA), Johnson-Cook (JC), Steinberg-Guinan (SG), and Preston-Tonks-Wallace (PTW).

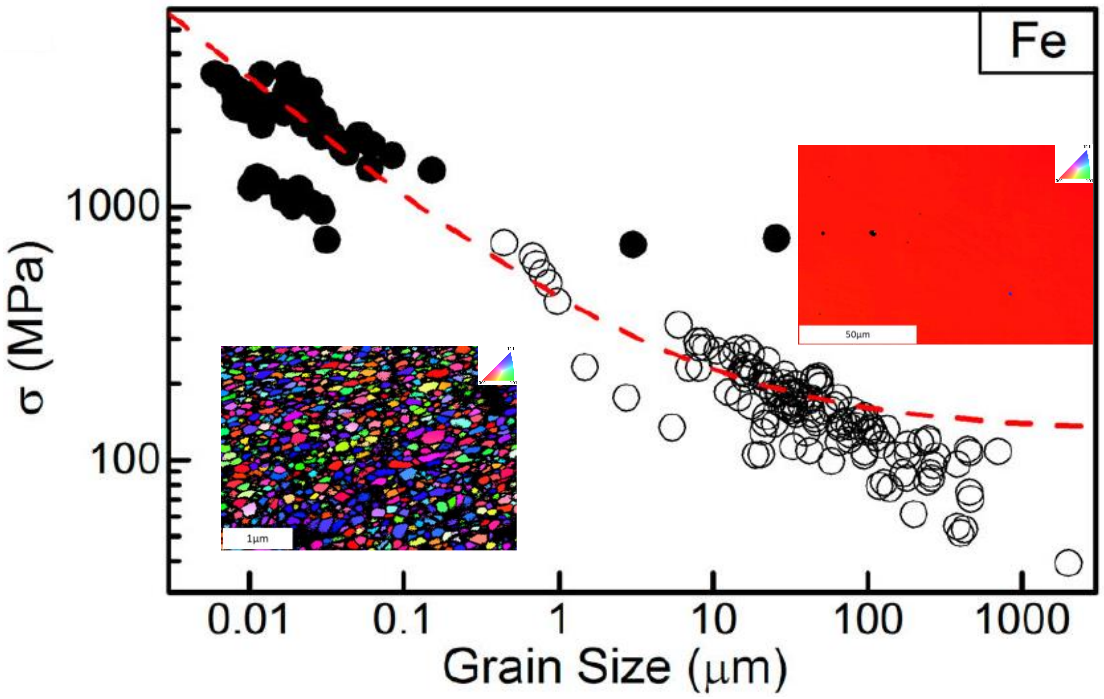

Figure 2-18. Hall-Petch effect in iron with insets of EBSD maps showing grain sizes. The closed points indicate Vickers and nanoindentation hardness measurements that were divided by a Tabor factor of 3 while the open points indicate yield strengths measured using compression or tension tests [62].

Voce strain hardening behavior was first realized by E. Voce in 1948 and describes an empirical relationship between stress and strain takes into account hardening behavior [63]:

$$\sigma = K - Bexp(-C\epsilon) \tag{11}$$

where σ and ϵ are the true stress and strain and K, B, C are material parameters. This is a commonly used model to explain hardening solely due to an applied strain. The ZA strength model is based on dislocation mechanics, developed by Frank Zerilli and Ronald Armstrong in 1987 [64]. The effects of strain hardening, strain rate hardening, thermal

softening, and grain size are included in this constitutive model. They developed separate relations for FCC, BCC, and HCP materials. However, their equation for BCC materials, shown below, does not account for twinning.

$$\sigma_y = \Delta\sigma_G' + c_1 exp(-c_3 T + c_4 T ln\dot{\epsilon}) + c_5 \epsilon^n + kd^{-1/2} \quad (12)$$

where $\Delta\sigma_G'$ is an additional stress component from the influence of a solute atoms and original dislocation density and n, c_1, c_3, c_4, c_5 are material constants. The JC model is purely empirical and also takes into account effects of effects of strain hardening, strain rate hardening, and thermal softening. In their 1983 paper, Gordon Johnson and William Cook determined material constants from various experiments (torsion tests over a wide range of strain rates, static tensile tests, dynamic Hopkinson bar tensile tests and Hopkinson bar teats at elevated temperatures) and found good computational results for a range of cylinder impact conditions [65]. Their constitutive equation is as follows:

$$\sigma_y = [A + B(\epsilon_P)^n]\left[1 + Cln\left(\dot{\epsilon_p}\right)\right][1 - (T^*)^m] \quad (13)$$

where A, B, n, C, m are material constants, T* is $(T-T_{room})/(T_{melt}-T_{room})$. The SG model was first developed in 1980 by Steinberg, Cochran, and Guinan for high-strain-rate modelling, but later (1989) extended to lower strain rates by Steinberg and Lund [66,67]. This semi-empirical model describes shear modulus (G) and yield strength (Y) as a function of strain, pressure, and temperature:

$$G(P,T) = G_0\left[1 + (G_P'/G_0)P\eta^{-\frac{1}{3}} - (G_T'/G_0)(T - 300K)\right] \quad (14)$$

$$Y = Y_{wh}\frac{G(P,T)}{G_0} \tag{15}$$

where G_0 is the shear modulus at reference conditions, $\eta = \rho/\rho_0$ is the compression ratio in density, and G_P' and G_T' are the pressure and temperature dependence coefficients for the shear modulus. The work-hardened yield strength, Y_{wh}, is defined by:

$$Y_{wh} = Y_0[1 + \beta(\epsilon_i + \epsilon_p)]^n \tag{16}$$

where Y_0 is yield strength at reference conditions, ϵ_p and ϵ_i are the deformed and initial equivalent plastic strain; β and n are work hardening parameters. If Y_{wh} exceeds the maximum yield strength, $Y_{wh,max}$, then Y_{wh} is reset to $Y_{wh,max}$.

Lastly, the PTW model, developed in 2003, describes the flow stress up to extreme conditions as a function of pressure, temperature, and strain rate. The dependence of the plastic strain rate on applied stress at low strain rates is of the Arrhenius form. Work hardening is modeled as a generalized Voce law. At strain rates exceeding 10^9 s^{-1}, work hardening is neglected, and the rate dependence of the flow stress is calculated using Wallace's theory of overdriven shocks in metals. The thermal-activation regime is continuously merged into the strong shock limit, yielding a model applicable over the 15 orders of magnitude in strain rate from 10^{-3} – 10^{12} s^{-1} [68]. The constitutive equation is as follows:

$$\hat{\tau} = \hat{\tau}_s + \frac{1}{p}(s_0 - \hat{\tau}_y) ln \left\{ 1 - \left[1 - exp\left(-p\frac{\hat{\tau}_s - \hat{\tau}_y}{s_0 - \hat{\tau}_y}\right)\right] exp\left[-\frac{p\theta\epsilon}{(s_0 - \hat{\tau}_y)\left[exp\left(p\frac{\hat{\tau}_s - \hat{\tau}_y}{s_0 - \hat{\tau}_y}\right) - 1\right]}\right]\right\} \quad (17)$$

where $\hat{\tau}_s$ and $\hat{\tau}_y$ are the work hardening saturation stress and yield stress which are functions of temperature, strain rate, and shear modulus; p and θ (from the Voce relation [63]) are material parameters, and s_0 is the value that $\hat{\tau}_s$ takes at zero temperature. Equation 17 is accurate for many metals in the thermal activation regime, when strain rate is below 10^9 s^{-1}. Above that strain rate, the high temperature and large strains associated with a strong shock causes work hardening to be saturated [68]. At this condition $\hat{\tau}_s = \hat{\tau}_y = s_0(\dot{\psi}/\gamma\dot{\xi})^{\beta}$ where $\dot{\psi}$ is the plastic strain rate, γ is a dimensionless material parameter, $\dot{\xi}$ is the atomic vibration frequency, and β is determined experimentally. Parameters used for each model are listed in Table 2-2 where s_x and y_x are used in the calculation of $\hat{\tau}_s$ and $\hat{\tau}_y$, respectively.

Table 2-2. Parameters for iron for the various strength models

Hall-Petch [62]	
σ_0 (MPa)	130
k (Mpa μm$^{1/2}$)	310

Voce [70]	
K	1463
B	650
C	87

Zerilli-Armstrong [64]	
$\Delta\sigma_G'$ (MPa)	0.0
c_1 (MPa)	1033
c_3 (K^{-1})	0.00698
c_4 (K^{-1})	0.000415
c_5 (MPa)	266.0
n	0.289
k (MPa m$^{1/2}$)	0.7

Johnson-Cook [65]	
A (MPa)	175
B (MPa)	380
C	0.060
n	0.32
m	0.55
T_m (K)	1811

Steinberg-Guinan [69]	
G_0 (GPa)	77
G_P' (1/GPa)	226
G_T' (1/K)	4.55×10^{-5}
Y_0 (GPa)	0.34
$Y_{wh,max}$ (GPa)	2.5
β	43
ϵ_i	0
n	0.35

Preston-Tonks-Wallace [71]		
	α-Fe	ε-Fe
θ	0.015	0.015
p	3.0	3.0
s_0	0.01	0.01
s_∞	2.5×10^{-3}	2.5×10^{-3}
y_0	6.625×10^{-3}	6.625×10^{-3}
y_∞	7.5×10^{-4}	7.5×10^{-4}
y_1	6.625×10^{-3}	0.03
y_2	0.265	0.25
κ	0.35	0.3
γ	1×10^{-5}	1×10^{-5}
β	0.265	0.25
α	0.23	0.23
T_{melt} (K)	1810	2050
G_0 (GPa)	87.2	87.2

As previously discussed, dislocations are the primary method of deformation in solid-state materials and the resistance to dislocation motion is the basis for material strength. When shear stresses are applied the dislocations need to overcome a barrier to deform the material, as shown in the inset of Fig. 2-19a. Dislocations can overcome this barrier through thermal activation or phonon drag. At low strain rates, thermal fluctuations in the lattice can move the dislocation over the barrier and allow it to continue moving until it gets pinned again. If the shear stresses are too large, dislocations are easily pushed over the barrier, so the resistance to motion comes from phonon drag. Phonon drag is a process in which the interaction of a dislocation with thermal vibrations (i.e. phonons) causes them to scatter and slow the dislocation motion. The PTW model is the only constitutive relation that takes into account both thermal effects and phonon drag. The original SG model was not appropriate for high-strain-rate deformation while the improved Steinberg-Lund model has a simple linear relationship in the phonon drag regime. The effect of this difference on strength can be seen in Fig. 2-19b. At the highest dislocation velocity, approaching the shear wave velocity, relativistic effects begin to play a role.

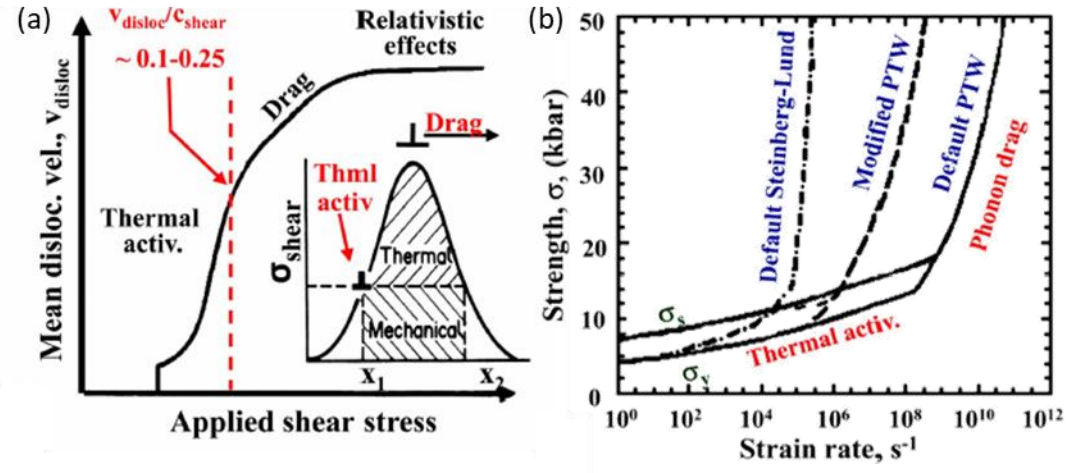

Figure 2-19. (a) Sketch of dislocation velocity vs applied shear stress. The inset shows schematically an edge dislocation pinned against a barrier in stress vs position. (b) PTW strength model vs strain rate, for low strain limit and the saturated, high strain limit for default (solid) and for the modified (dashed) input parameters. Also shown is the Steinberg–Lund model. [21]

Rayleigh-Taylor (RT) instability, named after Sirs Rayleigh and Taylor, is a method in which strength of a material can be measured when traditional measurement capabilities (strain gauges) are inadequate. This is an instability at the interface of two fluids of different densities that occurs when a lighter fluid accelerates into a heavier fluid [72,73] (Fig. 2-20a). Assuming the instability is unperturbed in the x and y directions and it only grows in the z direction, the material velocity can be written as [18]:

$$u(x,\ y,\ z,\ t) = u_z e^{i(k_x x + k_y y) + \gamma t} \tag{18}$$

where u is the velocity component, k is the wavenumber, γ is the growth rate, and t is time. Further assumptions are that the amplitude of the perturbation, η, is small (η << λ) such that the pressure and density variations are small ($P = P_0 + \delta P,\ \rho = \rho_0 + \delta\rho$), the perturbation grows in the linear regime, and the fluids are noncompressible ($\nabla \cdot \vec{u} = 0$).

Following these assumptions, the general three-dimensional equations of motion can be linearized such that:

$$\frac{\partial \delta\rho}{\partial t} + \vec{u} \cdot \nabla\rho = 0 \tag{19}$$

$$\rho \frac{\partial \vec{u}}{\partial t} = -\nabla\delta P - a\delta\rho\vec{z} \tag{20}$$

where a is the acceleration that pushes the lighter fluid into the heavier fluid. Equation 18 can then be differentiated and substituted into Equations 19 and 20 to produce the following four equations for each velocity component:

$$\rho\gamma u_x = -ik_x\delta P \tag{21}$$

$$\rho\gamma u_y = -ik_y\delta P \tag{22}$$

$$\rho\gamma u_z = -i\frac{\partial}{\partial z}\delta P - a\delta\rho \tag{23}$$

$$\delta\rho\gamma = -u_z\frac{\partial \rho}{\partial z} \tag{24}$$

Equations 21 and 22 can then be multiplied by $-ik_x$ and $-ik_y$, respectively, added, and simplified to produce the following:

$$\rho\gamma\frac{\partial u_z}{\partial z} = -k^2\delta P \tag{25}$$

where k is the wavenumber and is equal to $(k_x^2 + k_y^2)^{\frac{1}{2}}$. Equation 23 can be solved for $\delta\rho$ and substituted into Equation 24 to produce:

$$\rho\gamma u_z = -\frac{\partial}{\partial z}\delta P + u_z\frac{a}{\gamma}\frac{\partial \rho}{\partial z} \tag{26}$$

Lastly, solving Equation 25 for δP and substituting this solution into Equation 26 yields the equation for single mode planar RT instability growth:

$$\frac{\partial}{\partial z}\left[-\rho\gamma\frac{\partial u_z}{\partial z}\right] = k^2\left[-\rho\gamma u_z + u_z\frac{a}{\gamma}\frac{\partial\rho}{\partial z}\right] \tag{27}$$

The boundary condition for this equation is that velocity in the z-direction, u_z, and the rate of change of the velocity in the given z-direction, $\frac{\partial u_z}{\partial z}$, need to continuous across the interface. This can be written as:

$$u_0\frac{a}{\gamma}(\rho_2 - \rho_1) = \frac{\gamma}{k}(\rho_2 + \rho_1) \tag{28}$$

where u_0 is the initial velocity of the interface. Lastly, solving for the growth rate, γ, yields:

$$\gamma = \sqrt{Aka} \tag{29}$$

where A is the Atwood number, k is the wavenumber, and a is acceleration. When $\rho_2 \gg \rho_1$, A = 1, and the growth assumes its maximum value. If $\rho_2 = \rho_1$, A = 0, and no growth occurs. When $\rho_2 < \rho_1$, A < 0, the perturbation does not grow, but instead oscillates around the initial amplitude. There are multiple effects that can reduce the classical RT growth rate: surface tension, density gradient, ablation, and viscosity. The viscosity can be thought of as a measure of strength and thus the strength of a material can be inferred by comparing the difference between the initial and final perturbation amplitude [74]. If the material has no strength, the ripple growth will be uninhibited, but if the material has a finite strength, growth will be limited (Fig. 2-20b).

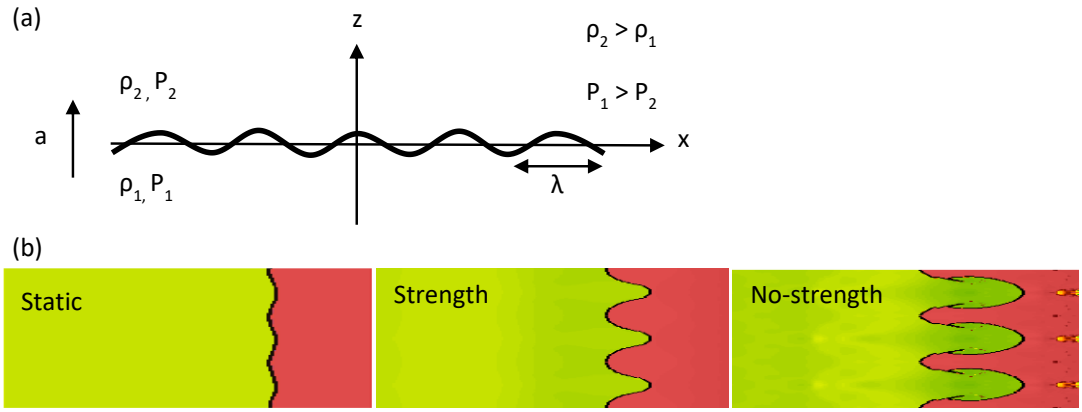

Figure 2-20. (a) Schematic of Rayleigh-Taylor induced ripple growth. A sinusoidal perturbation with wavelength λ and amplitude η on an interface between two uniform fluids of different densities accelerated upward. (b) Representation of ripple growth showing (left) initial, static ripple, (middle) ripple growth if material has strength, (right) ripple growth without strength.

2.7 Hydrodynamic simulations

In the design of laser experiments hydrodynamics codes are used to simulate the laser conditions, target assembly, and resulting pressure/temperature state. Hydrodynamic codes are formulated to solve the conservation laws (mass, momentum, and energy), equation of state (EOS), radiation transport, and other material phenomena (thermal conductivity, ionization, magnetism, etc.) [18]. The accuracy of such hydrodynamic codes is reliant on "real-world" experiments whose results are used to validate models. Numerical simulations provide guidance into the feasibility of an experiment; assist in developing the parameters of the experiment; and they provide a tool for interpreting the experimental results.

One such code, called Hydra, was developed by Lawrence Livermore National Lab to model capsule implosions at the NIF [75]. Another similar code, called Ares, is also commonly used multi-physics code developed by LLNL [76]. Both codes use a structured mesh and arbitrary Lagrange Eulerian formulation to accurately model radiation transport with a variety of targets. One of the benefits of these codes is that mesh motion can also be solely Lagrangian – where the coordinates of the mesh are tied to the fluid at t=0 and move with the fluid velocity, keeping zone mass constant throughout the simulation. This formulation allows for better modeling of distinct, layered targets as are used in direct-drive (DD) shots. The numerical code Hydra is used to accurately model laser interaction with an ablator material in one-dimension to create adequate compression profile for the iron samples. The pressure profile is depicted as a position-time (or x-t) plot to visualize the shock path within the samples and subsequent spall-induced reverberations for the JLF and DCS experiments. Ares is used in two dimensions to model the RT instability growth for the NIF and Omega EP experiments. In each hydrodynamic simulation, different constitutive models can be intrdoduced for the iron such as SG and PTW to determine the effect of strength on ripple growth. Such simulations are used to compare with experimental data, inferring iron strength at high pressure-temperature conditions.

Chapter 3: Quasistatic Compression

Uniaxial compression tests at low strain rates were performed to determine material strengths at ambient conditions. Small pillars (0.6 x 0.6 x 1.2 mm) were cut using Wire Electrical Discharge Machining (EDM) and tested under quasistatic compression and nanoindentation (Fig. 3-1). Under compressive loading, the material behavior is predictable and follows the Hall-Petch relationship (Eq. 10) that predicts a yield strength of 1100 MPa for a grain size of 100 nm. The nanocrystal behavior is seen to exhibit strain softening which occurs as a high dislocation density is reached. Single crystal behavior is characterized by traditional strain hardening. Nanoindentation also shows an increase in hardness in nanocrystalline iron – double the hardness for the same applied load.

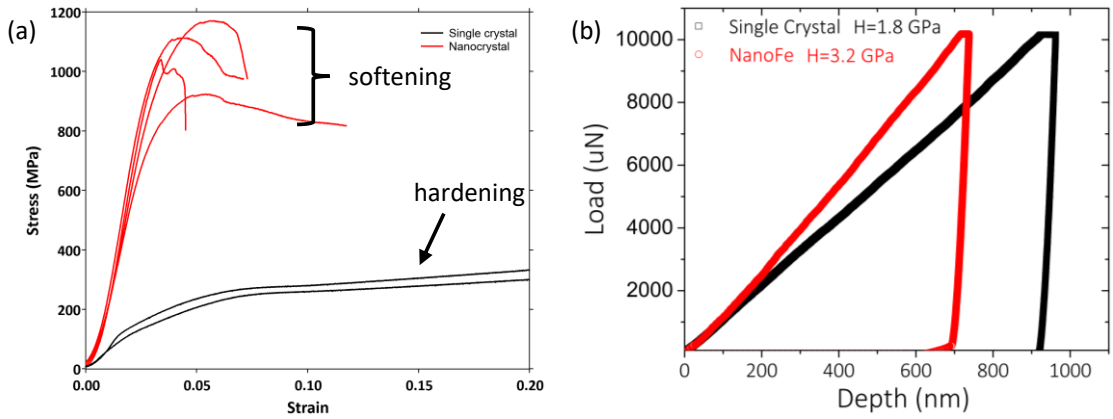

Figure 3-1. (a) Quasistatic compression of iron pillars using Instron Universal Testing Machine (3367 Dual Column Model) at a strain rate of 10^{-4} s^{-1} and (b) nanoindentation using Hysitron nanoindentor with a spherical tip with 150 nm radius.

Uniaxial compression tests in the quasistatic regime were also conducted at larger strain rate of 10^{-1} s^{-1}. At this rate, the material still follows the Hall-Petch relationship,

predicting yield strengths of ~400 MPa and ~1100 MPa for single and nanocrystalline iron, respectively (Fig. 3-2). Again, similar strain hardening and softening behavior is seen in single and nanocrystalline stress behavior, respectively.

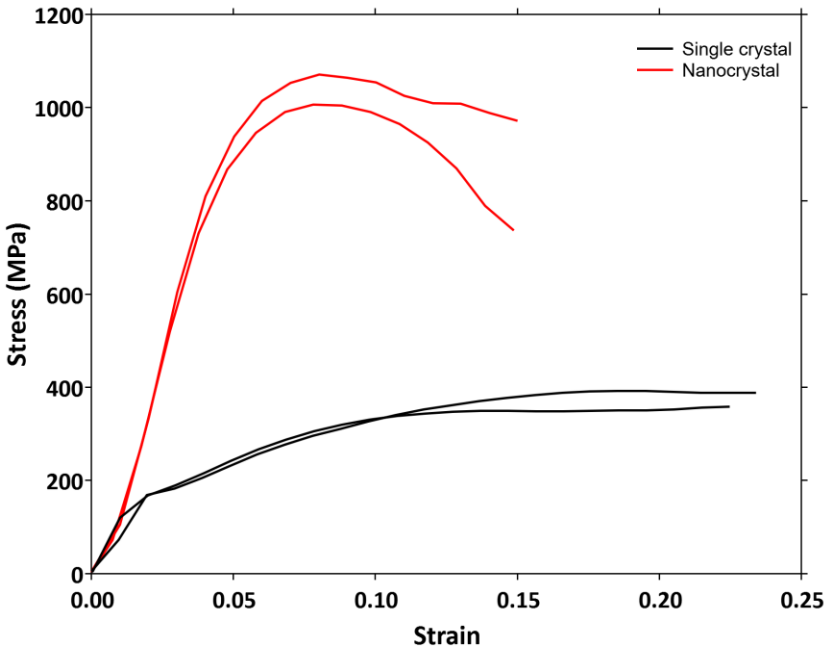

Figure 3-2. Quasistatic compression of iron pillars using Instron Universal Testing Machine (3367 Dual Column Model) at a strain rate of 10^{-1} s^{-1}.

Chapter 4: JLF Spall Experiments

4.1 Experimental and Computational Methods

Iron samples consisted of single crystal iron foils of 250 μm (Accumet Materials Co, 99.94+%) or 100 μm thickness (Surface Preparation Laboratory, ~99.98%), polycrystalline foils of 100 μm and 250 μm thickness (Goodfellow, ~99.5%), and nanocrystalline foils that were produced from the 1 mm thick single crystal samples (Accumet Materials Co, 99.94+%) using high-pressure torsion (HPT). The HPT process was conducted for 20 turns at 2 GPa to produce an average grain size of ~100 nm. All foils were then laser cut to 2.5 x 2.5 mm squares and mechanically polished to an optical finish using 30, 12, 9, and 5 μm silicon carbide and aluminum oxide paper, followed by 1 μm diamond suspension. Grain sizes were determined through Electron Backscatter Diffraction (EBSD) on a FEI Apreo Field Emission Scanning Electron Microscope (FESEM). Unshocked samples were mechanically polished to 0.04 μm finish using silicon carbide paper, diamond suspension, and colloidal silica suspension. EBSD confirmed that the single crystal had no grain boundaries and the [001] direction was oriented in the shock direction. Grain sizes were found to be 100-250 μm and 100 nm for poly- and nanocrystalline iron, respectively.

A 30 μm thick polystyrene ablator was adhered to one side of each sample foil using Hardman Double Bubble epoxy. All glue was tacked on the edges to minimize the gap between the sample surface and ablator. This assembly was then glued to a stainless-steel

washer with 10 mm outer diameter and 2 mm inner diameter. Recovery gel (Gelly^{TM} brand candle wax) was molten onto a debris shield, then upon solidifying was placed approximately 15 cm behind the target in the expected direction of motion (Fig. 4-1a). Samples were laser shocked in Target Area 1 in the Jupiter Laser Facility at Lawrence Livermore National Laboratory. The 100 J 2ω laser had a nominal square pulse shape with 10 ns duration and 1 mm spot size, resulting in peak power of approximately 1 TW/cm^2. VISAR (velocity interferometry system for any reflector) was used to record the velocity of the sample rear free surface (Fig. 4-1b) from which spall strength, peak pressure, and strain rates are calculated. Two independent interferometers were used to ensure the data is conclusive and appropriately calibrated in addition to allowing us to resolve 2π uncertainties in the phase (etalon thicknesses: d_1 = 49.968 mm and d_2 = 100.21 mm). 1-D radiation hydrodynamic simulations using Hydra [75] were run to predict peak pressure and spall strength (Fig. 4-1b). The incident square laser pulse produces a triangular shock wave in the material which reflects off the free surface because of impedance mismatch (Fig. 2-11).

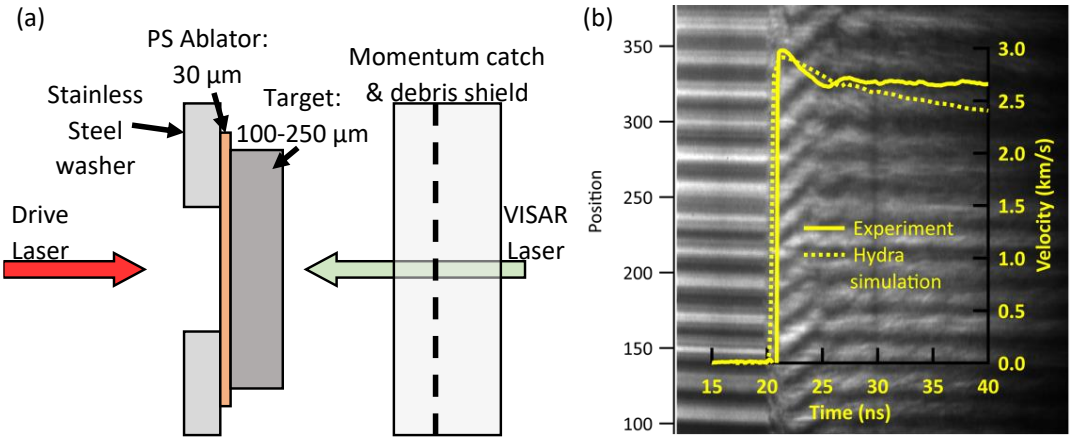

Figure 4-1. (a) Experimental set-up. The iron target is glued onto polystyrene ablator, which is then glued onto a stainless steel washer. Assembled target is placed in the target mount and the debris shield and momentum catch (polymer gel) is placed behind the target. VISAR laser is simultaneously used with the drive laser to capture interference fringes from the free surface. (b) 1-D radiation-hydrodynamic simulations predict free surface velocity similar to experimental measurement [75].

We performed non-equilibrium Molecular Dynamics (MD) simulations of shock compression, following standard practices. Experimental laser shock compression can be modeled by introducing a time-dependent piston velocity profile which dictates the prescribed shock volume and strain rate [77]. Controlled acceleration and deceleration profiles can mimic the stress profile introduced during shock compression [50,78,79]. The piston is linearly accelerated to 800 m/s over 5 ps, maintained at that velocity for 20 ps, then decelerated to stationary over 20 ps, resulting in strain rate of approximately 10^{10} s^{-1}. Although the latter is higher than the experimentally applied strain rates, it will be shown in Section 4.4 that it is adequate to capture the deformation mechanisms taking place in the experiments. Four different Fe samples were modeled, single crystal with [001] oriented

in the shock direction, and three nanocrystalline samples with average grain sizes of 14 nm, 12 nm, and 10 nm. The nanocrystalline samples were prepared using Atomsk [80] with sample dimensions of 50 x 50 x 150 nm^3, comprising approximately 32 million atoms. We employed periodic boundary conditions transverse to the shock direction (Z), allowing for unconstrained expansion of the free surface in the shock direction. The systems were compressed along the Z direction. We employed an extensively used Embedded Atom Model (EAM) potential that is fitted to adequately reproduce the α-ϵ phase transition of Fe [50,81–87]. Simulations were run using LAMMPS [88] and visualization was performed using OVITO [89] post-processing algorithms (adaptive common neighbor analysis [90], polyhedral template matching [91], construct surface mesh [92] and dislocation extraction algorithm (DXA)) [93]. The nanocrystalline samples were minimized and thermally annealed at $0.7T_m$ for 0.5 ns. All samples were thermalized at 300 K prior to loading.

In addition to non-equilibrium molecular dynamics, a nanometer-sized void in iron was modeled using the same potential as described above. The simulation domain was initially set up as a cubic sample containing 563 unit cells with one spherical void (r = 1.5 nm) at the center of the sample. Periodic boundary conditions were imposed in all directions and the sample was equilibrated to zero pressure at an initial temperature of 300 K. A uniaxial tensile strain rate of 10^9 s^{-1} was applied in the [001] direction for 120 ps, resulting in a total of 12% volume strain with lateral strains impeded. A 1 fs time step was chosen and the simulation was run with a constant NVE (number, volume, energy)

integration consistent with the micro-canonical ensemble such that no temperature control is imposed and we could measure temperature effects due to plasticity. The dislocation extraction algorithm technique (DXA) was used to identify line defects.

4.2 Spall Strength

The spall strength and strain rate were calculated from Equations 6 and 7. The approximate strain rate for the 250 μm thick samples was ~10^6 s^{-1} while a reduction in thickness to 100 μm increased the strain rate ten-fold, to ~10^7 s^{-1}. The peak pressure achieved during spall was calculated using the Hugoniot relationship between pressure and particle velocity, assuming particle velocity is approximately half of the free surface velocity. Peak pressures ranged from 60 GPa – 100 GPa, well above the theoretical 13 GPa α-ϵ phase transformation pressure. Representative VISAR traces of free surface velocity depicting strain rate and grain size dependence can be seen in Fig. 4-2 and the resulting strain rate and spall strengths are summarized in Fig. 4-2c.

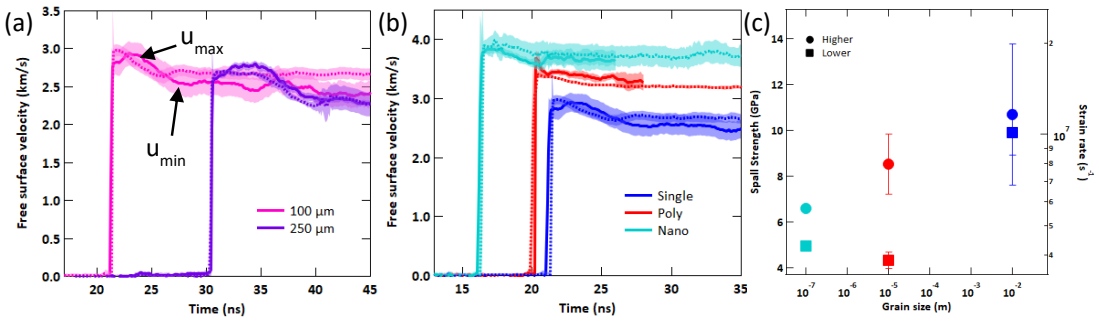

Figure 4-2. Representative VISAR traces (solid and dashed lines represent two channels of VISAR). (a) Strain-rate dependence in single crystal samples and (b) grain size dependence for samples of 100 μm thickness. Zero time represents start of drive laser and shaded region represents combined error from standard deviation and a systematic error. (c) Spall strength dependence on grain size and strain rate in iron. Nanocrystal samples (teal) show lowest spall strength while larger grained single crystal (blue) show highest spall strength. Higher strain rates result in high spall strength for all grain sizes. Error bars are the result of experimental variation in sample thickness.

Experimental results from this study provide the necessary evidence that the reverse phase transformation has occurred: a ductile spall surface is observed, and peak pressures reached well above the α to ϵ phase transition pressure. The spall strength is found to depend on initial microstructure, which might be surprising since in-situ diffraction results of iron shock driven into the ϵ phase reveal transformation-induced nanoscale grain sizes much smaller than the grains in any of the initial microstructures [51]. If void nucleation sites occurred on these transformation-induced grain boundaries, their presence could mask the effect of the initial microstructure. However, the spall strength does depend on the scale of the initial microstructure. Post-shock characterization of the structure near the spall plane, described in Section 4.3, supports the hypothesis that the reverse phase transition returns the material to a microstructure similar to the starting one. This was further

investigated with similar experiments at the DCS. The spall strength is expected to be highest in single crystal because of the scarcity of fracture nucleation sites. Grain boundaries are a common nucleation site for voids under dynamic tensile loading and dislocation pile-up locations under shear loading [94]. Since shock-induced spallation is a combination of tensile and shear forces, it can be expected that the presence of grain boundaries propitiates nucleation sites which weaken the material. This result is in agreement with literature and spall theory that dates back three decades [38,49,50,52,54,94–97] (Fig. 4-3). The large symbols represent the current study; the small symbols come from a variety of sources; the closed symbols represent experiments; the open symbols represent simulations. The monocrystalline and nanocrystalline samples show consistently higher and lower spall strength, respectively. Polycrystalline samples show much larger variation in spall strength, due to a variety of factors: (1) large variation in grain size (5 – 250 μm), (2) sample purity (99.5 – 99.999%), and (3) sample processing conditions. Grain size, which is frequently unreported in the literature, will clearly affect spall strength, as smaller grains will have more grain boundaries and therefore be weaker. The sample purity will also affect the spall strength as solute atoms tend to migrate towards grain boundaries to decrease strain energy. Lower purity iron will have more grain boundary solutes which, in turn, affect the grain boundary coalescence strength and stress for nucleation voids. Different processing methods used in sample preparation can also introduce different levels of strain in the structure. We fit the spall strength by using a

power law (Fig. 4-3), which converge at a high strain rate close to the Debye frequency, or the frequency of atomic vibrations. At this extreme strain rate the spall strength can be considered the ultimate tensile strength, 35 GPa [97], at which point the interatomic forces can no longer hold the structure together. The fit for polycrystalline iron does not currently converge because of the lack of experiments or simulations at strain rates higher than ~10^8 s^{-1} and inconsistencies in the grain structure. Similar failure behavior has been seen in spalled tantalum [98], vanadium [99], and iron at lower strain rate [49].

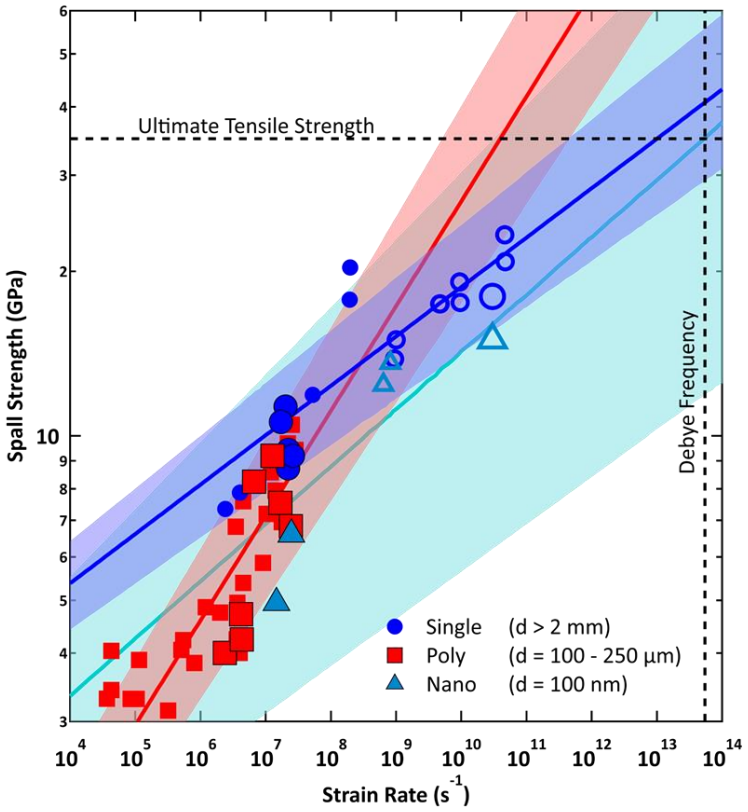

Figure 4-3. Spall strength versus strain rate on log-log scale with grain sizes from current experiments listed. Large symbols represent the current work, small symbols represent literature data, closed symbols represent experimental results, and open symbols represent simulation results. Power law fit to monocrystalline and nanocrystalline data converge near the ultimate tensile strength at ultra-high strain rate. Shaded regions represent 95% confidence interval. References as follows: [49,50,52,54,95,96,100–103]. Reference [100] and [101] report grain size of 19-40 µm and 5 µm, respectively. All other references do not report grain size.

4.3 Spall Morphology

The spalled surface of recovered samples was characterized by SEM while EBSD was used to characterize cross-sections to understand the failure mechanism. We find that the shocked single crystal iron shows nanoscale dimpling that is characteristic of ductile

failure (Fig. 4-4d) while poly- and nanocrystal iron samples show flaking that could be a result of failure via separation along grain boundaries (Fig. 4-4e, f). The high-pressure torsion process to fabricate the nanocrystal samples produces thin, elongated grains along which the spall occurs. Evidence of these elongated grains can be seen in (Fig. 4-4f). The dimple size in single and polycrystalline samples and the shear-like bands in nanocrystalline samples are consistent, on the order of 1 nm (Fig. 4-4g-i). In single crystal samples a remnant of the spall plane can be seen near the edge of the sample (Fig. 4-5a), in which twin boundaries can be found (Fig. 4-5b). The unmapped region around the twin boundaries can be attributed to voids/cracks or possibly a highly strained region that EBSD is unable to map. Randomly distributed voids are also seen through the cross section of the sample (Fig. 4-5c). For polycrystalline Fe, multiple spall layers can be seen in cross-sectional SEM images (Fig. 4-6a) with separation occurring along grain boundaries where this is a large density of voids (Fig. 4-6b). Density of geometrically necessary dislocations (GNDs) was mapped using Matlab toolbox MTEX according to Pantleon [104]. In both cases, GND density is approximately 10^{15} m^{-2} (Figs. 4-5d-e, 4-6d-e), which is consistent with heavily work-hardened materials [105] as well as shock compressed tantalum [106,107]. Furthermore, this technique underestimates the GND density as 3D maps are needed for a more accurate measurement. The circular regions with high dislocation densities (Fig. 4-5e) are due to sub-surface voids that emit shear dislocation loops. When these loops intersect the polished surface, they generate the circular regions of high GND

density. These are evidence for the shear loop emission mechanisms for void growth described in Section 2.4. The misorientation angle for the boundaries seen in Fig. 4-5b was measured to be ~60°, suggesting the formation of {001}/{112} twins. Additionally, these boundaries were found to be Σ3 boundaries (Fig. 4-7), which is known to occur from twinning [105].

Vestiges of a brittle fracture mechanism were observed at the edges of the spall plane where pressure and strain rate are lower than at the center of the sample. This can be explained by a brittle-to-ductile spall transition as described by Grady [97]. At a critical strain rate, the material can transition from fracture toughness controlled (brittle) to flow stress controlled (ductile). For iron, this critical strain rate is calculated to be on the order of 10^5 s^{-1}, a reasonable value for the edge of the spalled region where the shock has decayed. Smaller grained samples, however, do not display this behavior near the spall edge, because their spall behavior is dominated by grain boundaries rather than homogeneous void nucleation. These two morphologies are consistent with previous observations summarized by Meyers and Aimone [39]. Experimental results from this study provide the necessary evidence that the reverse phase transformation has occurred: a ductile spall surface and peak pressures well above the α to ϵ phase transition pressure.

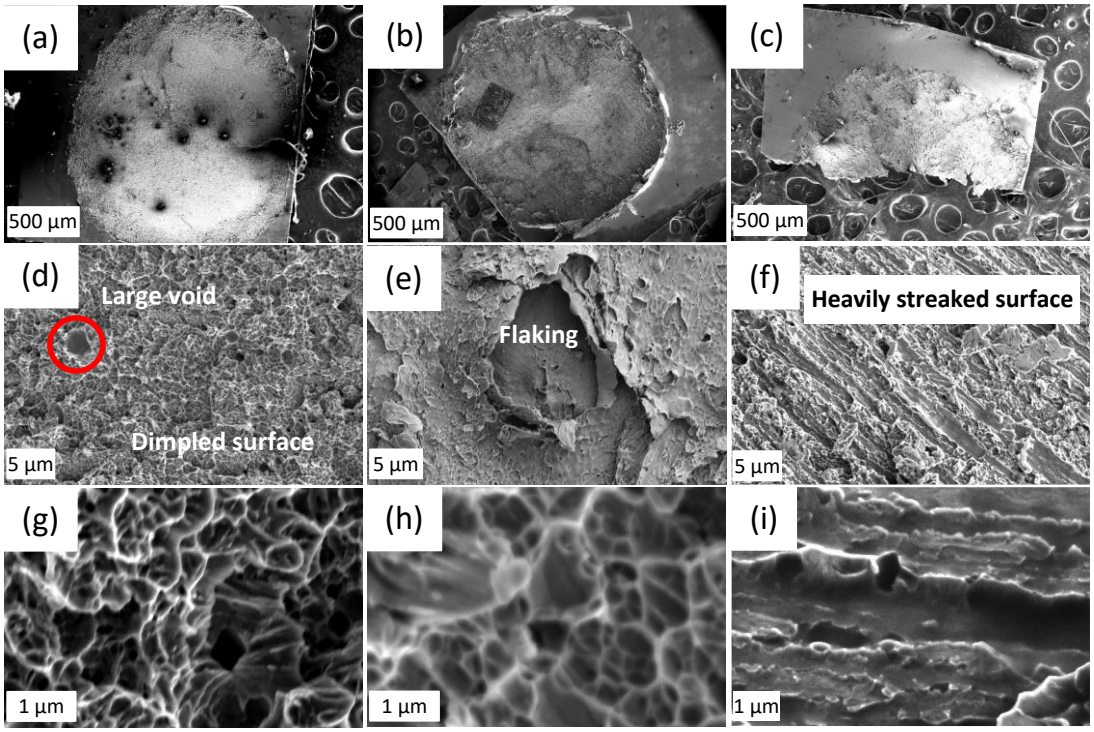

Figure 4-4. SEM images at three magnifications of single crystal (left), polycrystal (middle), and nanocrystal (right) at low (a-c), medium (d-f), and high (g-i) magnification. Dimpling in single and polycrystal iron is evidence of ductile fracture while shear-like bands in nanocrystal are evidence of spalling along grain boundaries. Dimple size in (g) and (h) and streak features in (i) are at the same length scale.

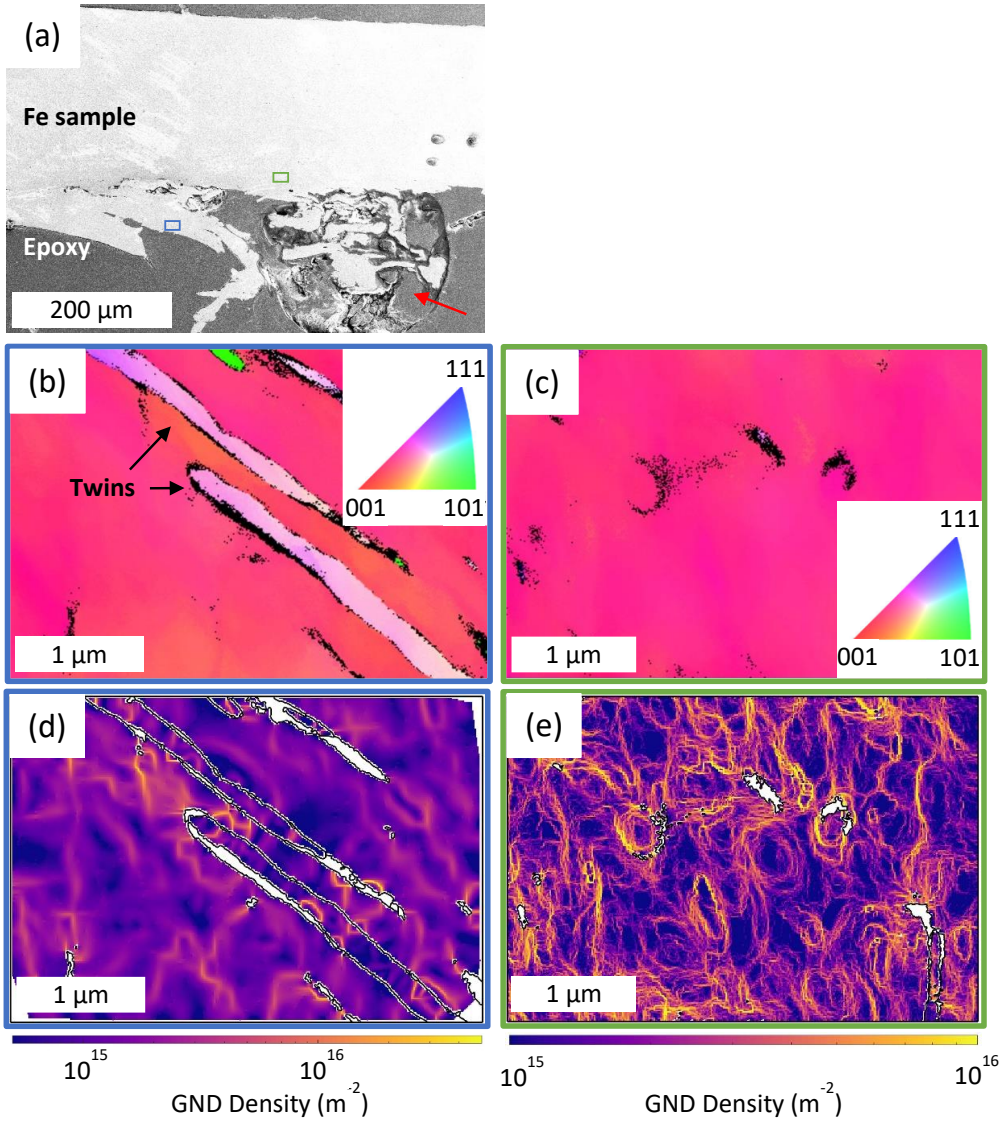

Figure 4-5. (a) Cross-section SEM image of shocked single crystal iron. Red arrow points to epoxy bubble. (b) EBSD mapping (IPF Z) near the spall plane shows large concentration of voids in vicinity of the twin boundary and (c) EBSD mapping further from the spall plane shows randomly spaced void groups. (d-e) Density of geometrically necessary dislocations is plotted for each EBSD map showing concentrations around 10^{15} m^{-2} in the bulk material and regions of higher concentration around twins or voids.

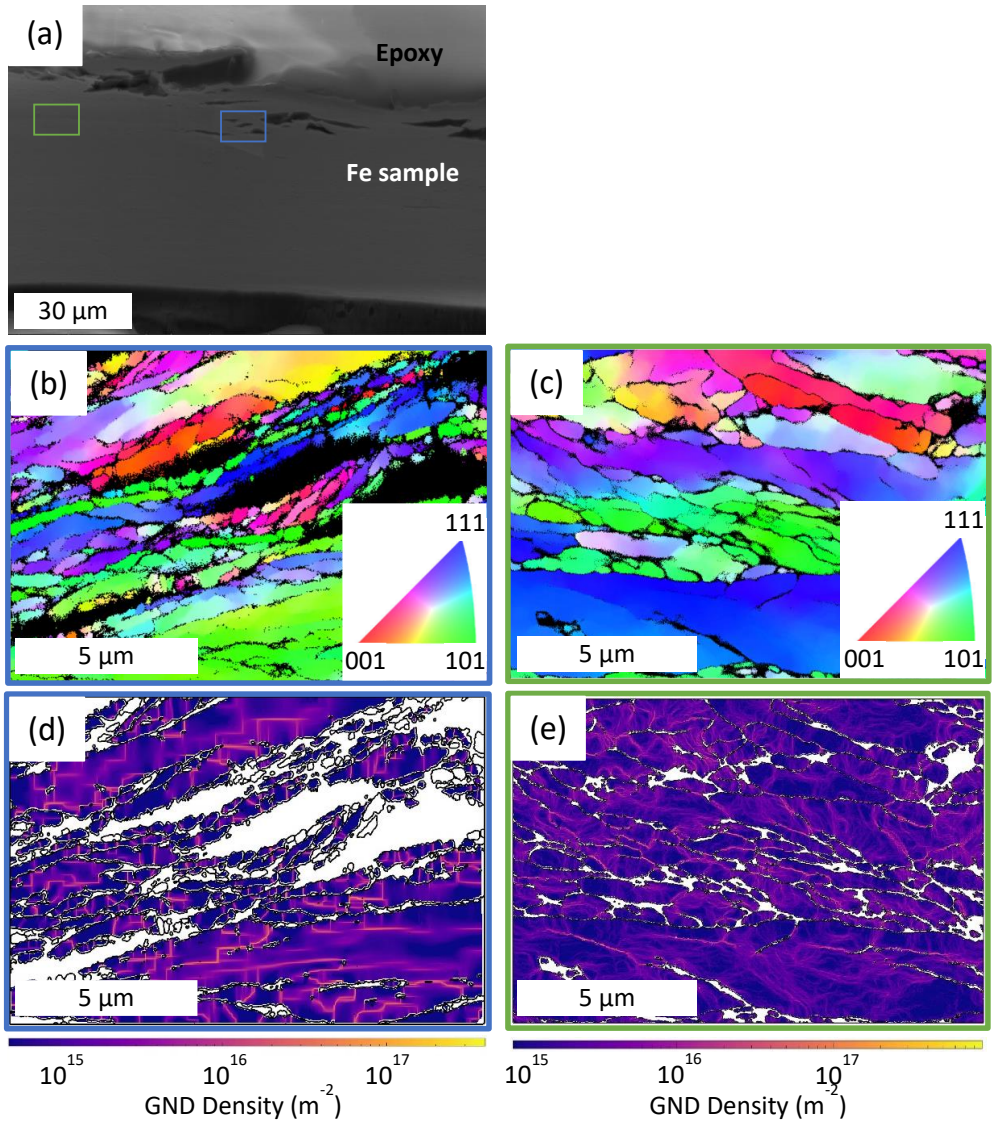

Figure 4-6 (a) Cross-section SEM image of shocked polycrystalline iron. (b) EBSD mapping (IPF Z) near the spall plane shows showing various cracks that are opening along grain boundaries and (c) EBSD mapping further from the spall plane. (d-e) Density of geometrically necessary dislocations is plotted for each EBSD map showing concentrations around 10^{15} m^{-2} in the bulk material and regions of higher concentration around sub-grain boundaries.

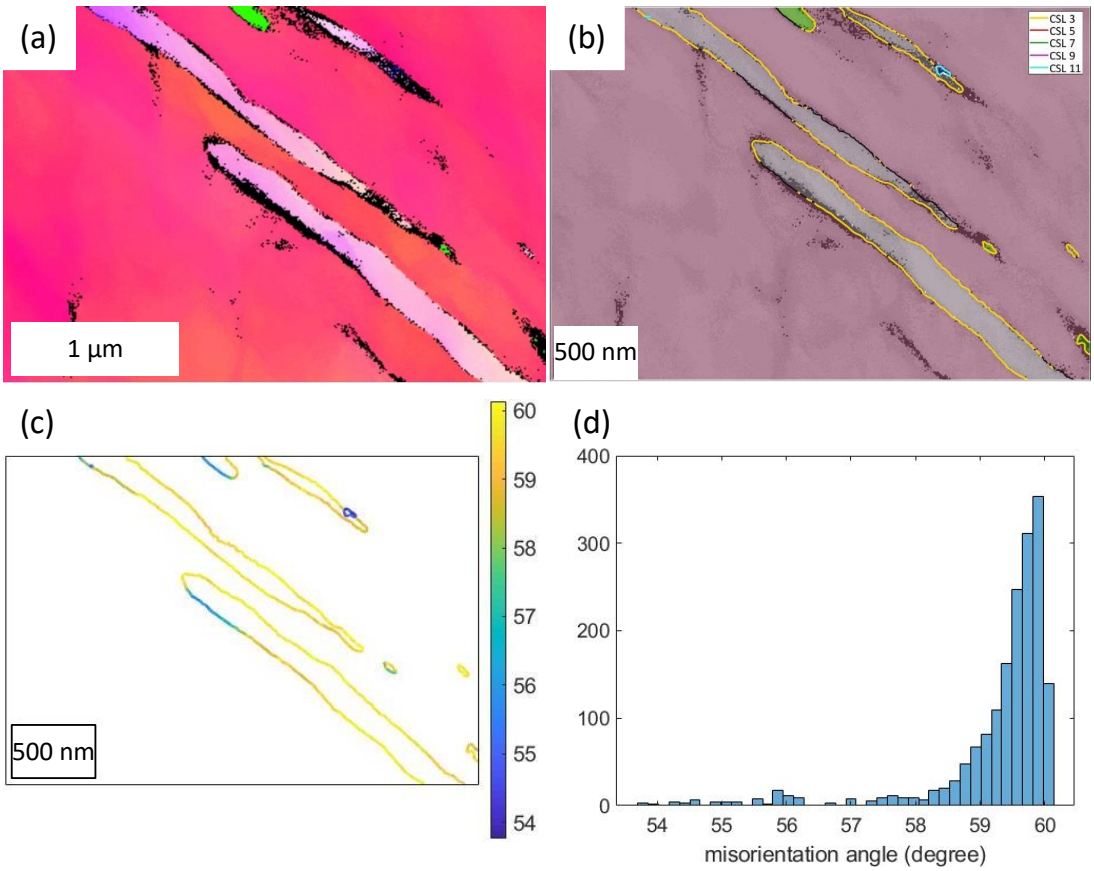

Figure 4-7. (a) EBSD mapping (IPF Z) of single crystal cross-section near the spall plane showing twin boundary and (b) corresponding Coincident site lattice boundary analysis providing evidence of a Σ3 boundary which corresponds to twinning. (c) Misorientation angle analysis and (d) corresponding histogram showing misorientation angle ~60°, which is also close to misorientation of a (112) twin plane and the (100) EBSD point of view.

Voids (~10 µm diameter) on the spalled surface were seen exclusively in single crystal samples (Fig. 4-8). We observe smoothed inner surfaces which are indicative of melting and re-solidification of the material. During shock compression the temperature is expected to rise [19], but not enough to melt the entire sample. Section 4.4 will discuss molecular dynamic calculations that determine the temperature of both the overall sample

and locally around a void. The formation of voids can occur from a variety of phenomena (Fig. 2-13). At the atomic scale, vacancy complexes can form nanoscale voids and at larger length scales twin and grain boundaries are also common void initiation sites, as we will see in Section 4.1.4. Second-phase particles or inclusions can cause cracks to emanate into the matrix material and as those cracks grow under tension cause debonding of interfaces. The large voids seen in SEM can be attributed to void formation at larger length scales while the overall fracture surface is caused by void nucleation and growth at smaller length scales.

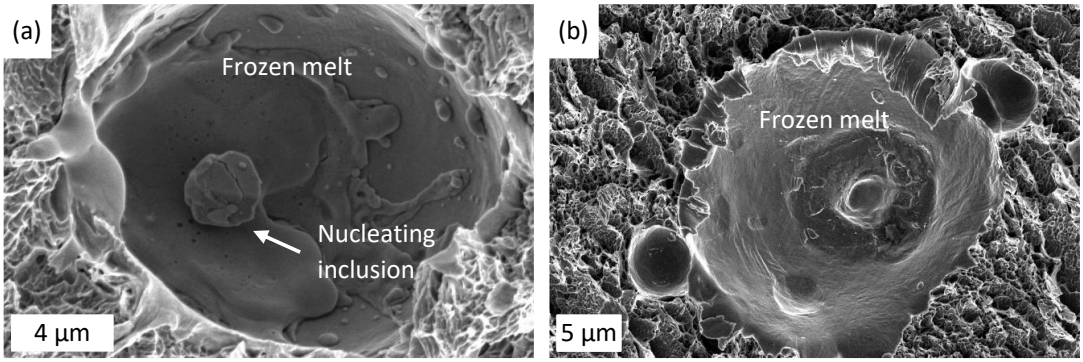

Figure 4-8. SEM images of voids found in single crystal iron. Voids are roughly 10 µm in diameter in both (a) high and (b) low strain rate samples. Smooth inner walls show evidence of melting inside the voids.

4.4 Molecular Dynamic Simulations

As the initial shock runs across the sample, an α to ϵ phase transition takes place. This is expected after the results by Gunkelmann et al. [84] and Amadou et al. [81] for similar shock conditions. For the single crystal, the MD simulations reveal the nucleation

of an ϵ phase that propagates along the sample in the shock direction, whereas for the nanocrystalline sample, the α to ϵ phase transition takes place within each grain, preserving the initial grain boundary structure. At later time, as the shock profile reflects from the rear surface of the sample, the reverse transition (ϵ to α) takes place. Interestingly, all samples return to their initial microstructure (α-Fe single crystal and nanocrystal with α-Fe domains), further supporting the experimental hypothesis that the reverse phase transition may return the microstructure to something like the starting material. Similar conclusions were obtained in previous MD studies of uniaxial compression and release of polycrystalline iron [84]. These processes take place before any spallation event.

Stress profiles in iron samples were calculated from non-equilibrium MD simulations along the shock direction for different times around the beginning of spallation (Fig. 4-9). Positive values of σ_{zz} indicate tension. Assuming that the spall strength is equal to the peak tensile stress along the shock direction, the single crystal strength is 18 GPa, while the nanocrystal strength is 14.5 GPa. There was no significant strength variation with grain size for the nanocrystalline systems modeled here. The peak stress for the single crystal occurs in a region between 75 and 100 nm at about 56 ps, with a marked drop in stress 2 ps later. This drop signals the inception of the spallation event, with the formation of one or more closely spaced voids in that region. The stress peak is broader for the nanocrystalline sample, resembling a plateau that spans around 50 – 100 nm. In this instance, as time evolves (≥ 54 ps) stress drops occur in several positions along the plateau, signaling a distribution of the spallation event as voids open at several locations in this

region. The delocalized spallation is due to the distributed nature of grain boundaries along the sample, two-dimensional defects that possess less strength and more void nucleation sites than in the single crystal.

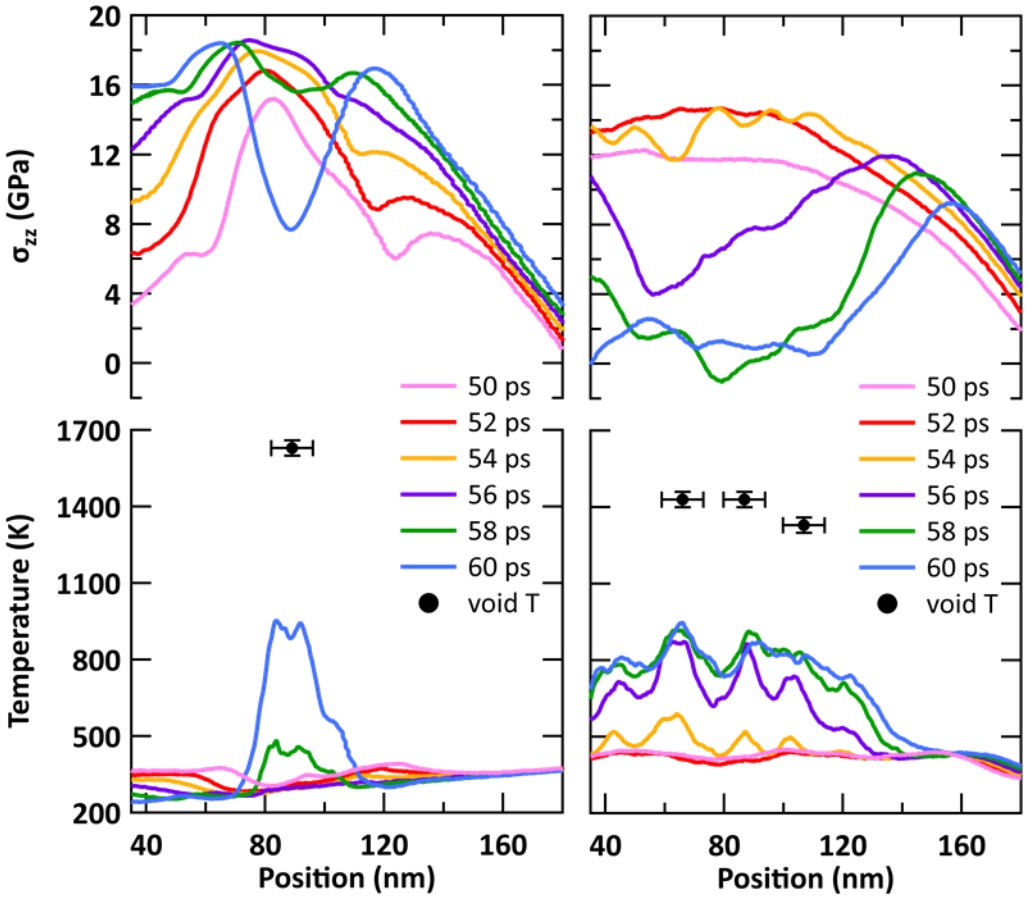

Figure 4-9. MD calculations of pressure in the z-direction (parallel to loading) and temperature in the single crystal (left) and nanocrystal (right) with 10 nm average grain size. Void T symbols correspond to the peak temperature in voids at 60 ns. Initial shock direction goes from left to right.

In the single crystal samples, as voids nucleate due to twin-twin interactions and grow, they start coalescing, forming larger flaws, weakening the sample's section, and ultimately leading to the formation of a spallation plane (Fig. 4-10a). For the

nanocrystalline simulations, however, the high fraction of grain boundaries offers energetically favorable nucleation sites for the formation of voids (Fig. 4-10b). The orientation of a grain boundary with respect to the wave propagation direction is more important than specific grain boundary orientation. This preferential failure along grain boundaries that are perpendicular to the loading direction is in agreement with previous studies on BCC metals [108]. Consequently, twinning is less pronounced, but can still be found in relatively large grains. In addition to computational evidence of intra-granular plasticity under spall conditions, similar observations can be found in the atomistic simulation literature: Gunkelmann and co-workers report intra-granular plasticity in α-Fe for their nanocrystalline studies both under homogeneous compression [36] and under non-equilibrium shock compression [29]. Experimental evidence of intra-granular plasticity is also found in both BCC and FCC metals [57–59]. Grain boundary plasticity is another factor that can play an important role, particularly for grain sizes as small as the ones used in this work and under the high stresses induced by the shock loading process. To add complexity, grain boundary plasticity can also be rate dependent, as shown by grain boundary disconnection motion studies [60]. Grain boundary sliding and intragranular plasticity were identified in our simulations

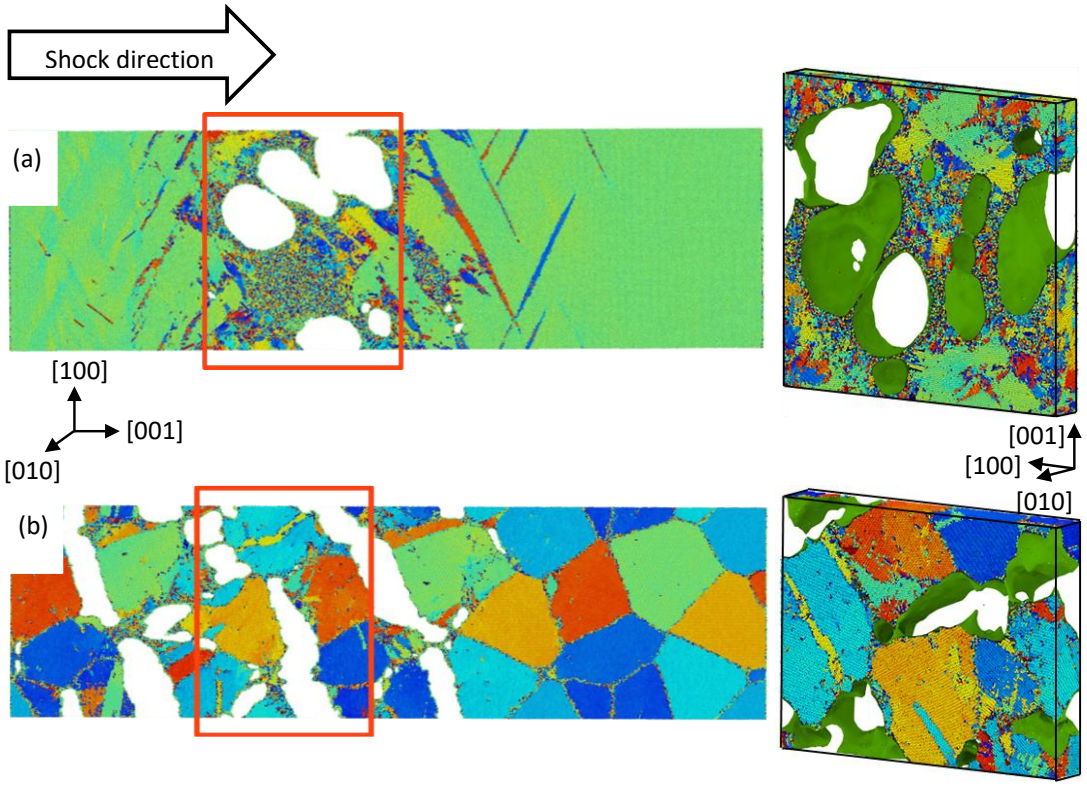

Figure 4-10. MD simulation of shocked (a) single crystal and (b) nanocrystal iron (10 nm grain size) at 68 ps with enlarged view of the spalling region. Atom coloring is based on the relative crystalline orientation and white corresponds to void region. Enlarged views (right) are rotated to highlight void where green surfaces correspond to spall surface. Initial shock direction goes from left to right.

The time-resolved evolution of void nucleation and growth during spall in the [001]-oriented single crystal sample can be seen in Fig. 4-11. The polyhedral template matching algorithm was used to classify the local structural environment of the atoms. Twins (orange domains) nucleated during spall form elongated structures that, upon intersecting, favor the nucleation and growth of spheroidal voids (Fig. 4-11). At a later stage, the voids have grown and are closer to each other, leading to coalescence. Void

formation by twin-twin interaction was also reported by Gunkelmann et al [50] in Fe spall simulations and by Hahn et al. [78] in Ta spall simulations.

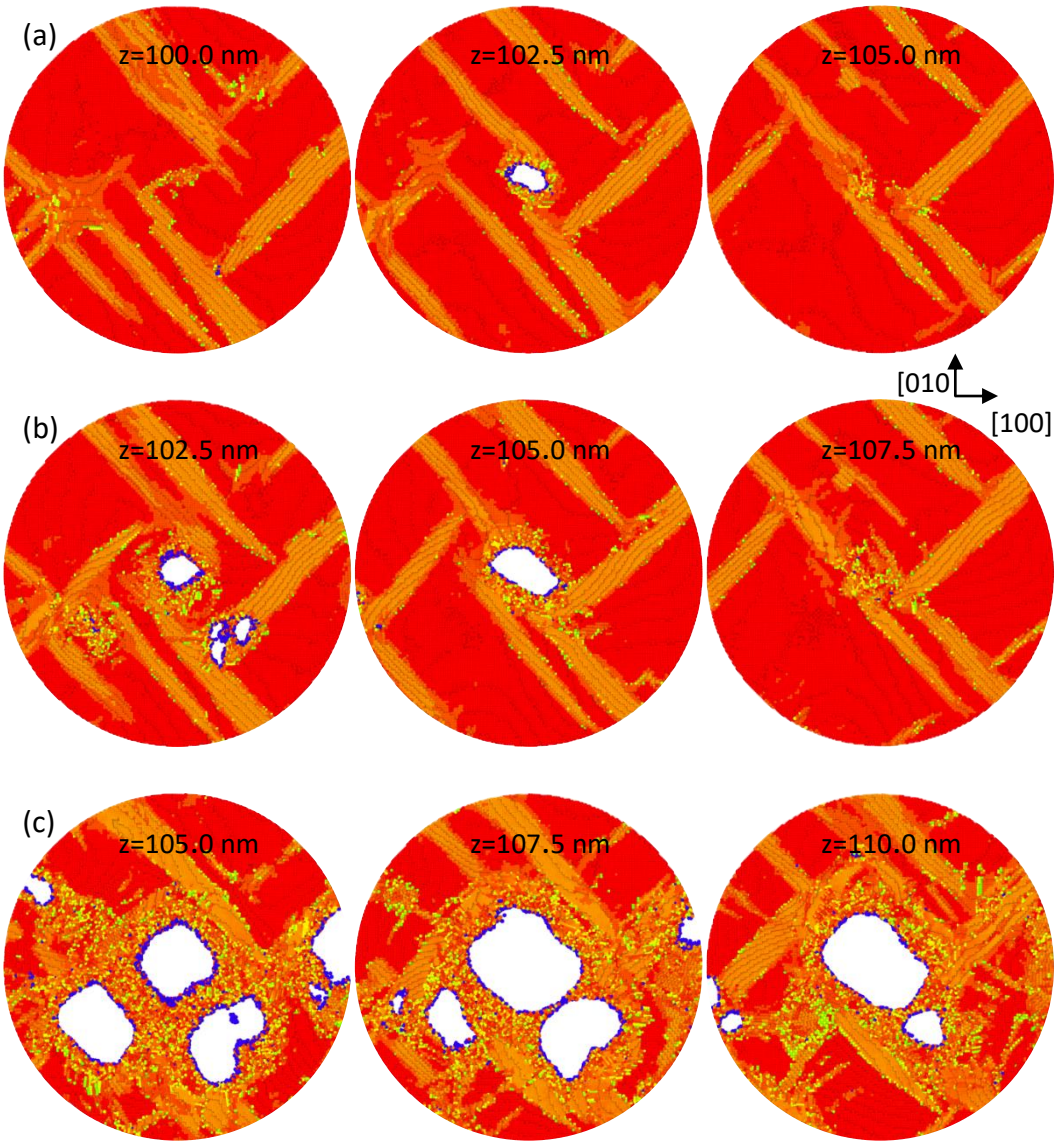

Figure 4-11. Slices of the single crystal sample along the shock direction at (a) 56 ps, (b) 58 ps, and (c) 62 ps. Atom coloring corresponds to local orientation of the atoms. Red corresponds to [100]-oriented BCC structure and orange are {110} oriented domains, which correspond to twins. The strong changes in color in the surrounding of the voids point to massive disorder, typically associated with melting.

4.5 Analytical model for dislocation generation around void surface

The MD predictions of high dislocation densities and temperatures around voids and the experimental observation of the apparent melting behavior stimulated the development of an analytical model for void-generating dislocations that increase the temperature. A nanometer-sized void is considered to act as a nucleation site for geometrically necessary dislocations (GNDs) that, upon propagation away from the void, lead to successive nucleation and propagation events (Fig. 2-15). This yields a quantifiable dislocation density. The motion of dislocations, in turn, heats the surroundings of the void due to plastic activity, producing a significant increase in local temperature. GNDs can be used to estimate the total dislocation length around a growing void by assuming that a certain number of dislocation shear loops are initially nucleated on the void surface and that they transport matter away from it [109–111]. This mechanism was proposed and analytically demonstrated by Lubarda et al. [112]; later MD simulations quantified the emission of dislocation shear loops and their eventual transformation into prismatic loops by a "lasso" mechanism for BCC crystals [113,114]. In the analysis presented below only the shear loop emission is evaluated because it is assumed prismatic loops do not form under uniaxial compression [115], until later when plastic flow reduces the background shear stress and the voids grow under greater stress triaxiality [116]. For the BCC structure, eight loops that propagate along BCC slip planes ($\{110\}/\langle 1\bar{1}1\rangle$) are initially assumed, and

other sets of loops are also created as the void growth proceeds. Figure 2-15 depicts the growth of a void by the emission of various dislocations.

For every emission i of loops, the total length is,

$$\Delta L_t^i = 8\left(2\, L_1^i + L_2^i\right) \tag{30}$$

where L_1 and L_2 are the lengths of the screw and edge components, respectively. It is assumed that each loop expands to a distance of 10 times the initial void radius. This is a reasonable assumption consistent with continuum plasticity treatments of void growth under hydrostatic tensile stresses. Once that loop reaches such distance, the applied shear stresses are sufficiently relaxed and the applied strain is accommodated by the emission of a new loop set. The total dislocation length around the void is:

$$L_{total}^i = L_{total}^{i-1} + \Delta L_t^i \tag{31}$$

The formation of the dislocation loops can be assumed to expand the void by an incremental volume dV [115] such that for every emission i, the incremental and new void volumes are:

$$\Delta V^i \cong 2\sqrt{2}\pi r_{(i-1)}{}^2 b \tag{32}$$

$$V^i = V^{i-1} + \Delta V^i \tag{33}$$

Assuming spherical voids, the radius at the i'th emission event is:

$$r_i = \sqrt[3]{\left(\frac{3}{4\,\pi}\right) V^i} \tag{34}$$

The strain is computed assuming the increase in volume due to void growth is accommodated by an increase in the vertical dimension, a_3, in the unit cell:

$$V_{sample}^{i} = V_{sample}^{i-1} + \Delta V^{i} = a_1 a_2 a_3^{i} \tag{35}$$

where a_1 and a_2 remain constant during uniaxial tension and a3 increases as:

$$a_3^{i} = \frac{V_{sample}^{i}}{a_1 a_2} \tag{36}$$

The corresponding strain increment $d\epsilon$ and total strain are:

$$\Delta \epsilon^{i} = \frac{a_3^{i} - a_3^{i-1}}{a_3^{i-1}} \tag{37}$$

$$\epsilon^{i} = \Delta \epsilon^{i} + \epsilon^{i-1} \tag{38}$$

The results for each generated emission event can be found in Table 4-1 for an example case. They show that after ten dislocation emissions, the void radius is doubled, for an initial void radius of 1.5 nm. The work-hardened volume is considered as the volume limited by the spherical volumes corresponding to the work hardened radius $R = 10r_i$ and void radius r_i:

$$V_{wh}^{i} = \frac{4}{3}\pi(R^3 - {r_i}^3) \tag{39}$$

Dislocation density, ρ_{GND}^{i}, can then be calculated as the ratio between total dislocation length (Eq. 31) and work hardened volume (Eq. 39):

$$\rho_{GND}^{i} = \frac{L_{total}^{i}}{V_{wh}^{i}} \tag{40}$$

It is important to note that to accommodate for the increasing strain, the analytical model uses successive loop generation events, and that beyond 10% strain the dislocation configuration becomes too complex for the simple assumptions. The dislocation velocity

(in m/s) as a function of shear stress, $\bar{v}(\tau)$, can be computed assuming a power law fit to the experimental results of Urabe and Weertman [117]:

$$\bar{v}(\tau) = 0.882\tau^{0.986} \tag{41}$$

The shear stresses were computed from our MD simulations of shock compression as [118]:

$$\tau = \frac{1}{2}\left[\sigma_{zz} - \frac{1}{2}\left(\sigma_{xx} + \sigma_{yy}\right)\right] \tag{42}$$

where σ_{xx}, σ_{yy}, and σ_{zz} are the hydrostatic stresses in the x, y, and z geometrical directions. The shear stresses obtained during the void nucleation and growth process and within that region are, on average, 600 MPa (0.6 GPa), giving an average dislocation velocity of approximately 500 m/s. Similar dislocation velocities were observed in our MD simulations of a single void under high strain rate uniaxial tension and are also consistent with previous studies on BCC Ta under high strain rate uniaxial compression [114]. The plastic shear strain rate can be related to the mobile dislocation density ρ_m using Orowan's equation [119]:

$$\dot{\epsilon}_p = b\ \rho_m \bar{v}(\tau) \tag{43}$$

where b is the Burgers vector, approximately 0.27 nm for α iron. The mobile dislocation density ρ_m is equal to a fraction of ρ_{GND} ($\rho_m = f\ \cdot \rho_{GND}$) where f is a mobile dislocation density fraction that is estimated assuming that the mobile dislocation density gradually decreases due to shear loops nucleating, propagating, and populating the work-hardened volume. This fraction takes the unity value as the first generation of loops leave the surface,

and linearly decreases to 0.1 as the last emission of dislocations takes place due to two main factors: (1) dislocation loops consist of dislocation edge components that slip with high mobility, while screw components have limited mobility and (2) the rapid formation of junctions leads to a decrease in mobile dislocations with respect to the total number of dislocations [115].

Assuming adiabaticity, the temperature increase associated with plastic deformation is expressed as:

$$\frac{dT}{dt} = \frac{\beta}{\gamma \cdot C} \cdot \tau \cdot \dot{\epsilon}_P \tag{44}$$

where γ is the material density, C is the specific heat capacity, τ is the time-dependent shear stress, and β is the Quinney-Taylor parameter that represents the fraction of rate of plastic work dissipated as heat [120], taken as equal to 1 for the sake of simplicity.

In reality, the evolution of dislocation density with plastic deformation is the result of the combined effects of dislocation generation and annihilation, with characteristic rates $\dot{\rho}_{gen}$ and $\dot{\rho}_{ann}$, respectively [121]:

$$\dot{\rho} = \dot{\rho}_{gen} - \dot{\rho}_{ann} \tag{45}$$

At the initial stages of plasticity, the material can be considered as pristine, and dislocations can expand and populate the surrounding volume freely. As the successive emission of loops takes place, the newly nucleated dislocations now propagate within a volume that contains dislocations. As more and more loops are emitted from the void surface, the plastic volume in the vicinity of the void has an increasing dislocation density and the dislocation forest requires a reduction of the mean free path. In consequence, annihilation events

become more probable, to the limit that the annihilation rate becomes equal to the generation rate once the dislocation density reaches a critical value, yielding saturation at around 10^{17} m^{-2}, consistent with conditions of shock compression in BCC metals [106,122]. As a first approximation, the dislocation annihilation rate is considered to be proportional to the dislocation density and inversely proportional to the mean free path before they encounter dislocations of opposite sign [123]. Indeed, the Kocks-Mecking theory has different power dependencies for the two terms, $\dot{\rho}_{gen}$ and $\dot{\rho}_{ann}$ [124] and a detailed treatment of the exact functional form for these high strain-rate conditions is beyond the scope of this work.

It is reasonable that when dislocation activity starts, the total and mobile dislocation densities are similar, but the rapid formation of junctions leads to a decrease in mobile dislocations with respect to the total number of dislocations. As the mobile dislocation density reaches a saturation value (~10^{17} m^{-2}), the $\dot{\rho}_{gen}$ and $\dot{\rho}_{ann}$ can be considered to be equal, such that $\dot{\rho}$ becomes zero. Thus, the total dislocation density, considering both generation and annihilation events, remains constant at the saturation point. The density of mobile dislocation decreases beyond a strain of 0.09.

The comparison of analytical and MD predictions is revealing. The MD-predicted dislocation density rises rapidly with plastic strain up to $5x10^{16}$ m^{-2} and then increases at a much lower rate. Although there are differences between the two predictions, the results are fairly consistent. Additionally, the dislocation density estimated from recovered

samples (10^{15} m^{-2}) is within one order of magnitude – a reasonable difference given the assumptions of the model and the underestimation of the EBSD GND technique.

Table 4-1. Estimation of temperature increase by GND emission

Emission no.	ΔV (nm^3)	V_i (nm^3)	r_i (nm)	V_{wh} (nm^3)	L_{total} (nm)	ρ_{mobile} (10^{16} m^{-2})	ρ_{gnd} (10^{16} m^{-2})	T (K)
0	0	14.13	1.5	0	0	0	0	300
1	4.94	19.07	1.66	4169.72	173.33	4.16	4.16	314.02
2	6.03	25.10	1.82	4163.69	348.06	7.52	8.34	338.82
3	7.24	32.34	1.98	4156.45	524.19	10.1	12.6	371.68
4	8.57	40.91	2.14	4147.88	701.76	11.8	16.9	409.38
5	10.03	50.94	2.30	4137.85	880.75	12.8	21.3	449.22
6	11.61	62.54	2.46	4126.24	1061.18	12.9	25.7	488.51
7	13.31	75.85	2.63	4112.93	1243.06	12.1	30.2	524.67
8	15.13	90.99	2.79	4097.80	1426.40	10.4	34.8	555.22
9	17.09	108.07	2.95	4080.71	1611.19	7.90	39.5	577.81
10	19.16	127.24	3.12	4061.55	1797.45	4.43	44.3	590.18

Parameters for Eqs. 30 through 45 are taken as follows: R = 10 nm, γ = 7300 kg/m^3, C = 460 J/(kg K), τ = 0.6 GPa after MD simulations, $\bar{v}$ =500 m/s [117].

The emission and propagation of dislocations for ten successive generation events increases the temperature to 590 K, an increase of over 250 K above the initial value. This

corresponds to an increase in void radius from 1.5 to 3 nm. GND-predictions can also be compared with the temperature profiles of the spall simulations (Fig. 4-9). The temperature rise at void initiation at 58 ps and 54-56 ps in single and nanocrystal iron, respectively, is similarly ~250 K. The void nucleation in the spall simulations exhibits important differences not included in the model; e.g. under spall conditions, voids nucleate at twin-twin intersections in a heavily stressed environment, whereas the model presented in this section contains a pre-existing void under equilibrium conditions. In addition, several other factors may also play a role under shock loading conditions, such as phase transformation, microstructural evolution, thermal softening, heat conduction or even electron-phonon coupling [125,126]. In particular, heat conduction can play an important role in void growth as pointed out by Wu et al. [126], since depending on the efficiency of the heat conduction, voids would grow adiabatically or non-thermally. One possibility or the other depends mainly on the initial void size, void growth rate, and material properties such as thermal conductivity, mass density, specific heat and yield strain. According to Wu et al. the criteria to determine when the adiabatic void growth or the non-thermal void growth idealizations should be considered is:

$$\begin{cases} \dfrac{a\,\dot{a}}{\Omega} < 0.01, & for\ non-thermal\ growth \\ \dfrac{a\,\dot{a}}{\Omega} > 100, & for\ adiabatic\ growth \end{cases} \tag{46}$$

where a is the initial void radius, $\dot{a}$ is the void growth rate, and $\Omega = 2.6k/\rho c_p \varepsilon_Y^{2/3}$, where k is the thermal conductivity, ρ is the mass density, c_p the specific heat capacity and ε_y the

yield strain. Considering the initial void radius, the void growth rate, $c_p = 460\ \frac{J}{kgK}$, and other parameters for iron after Wu et al [126] ($k = 80\ \frac{W}{mK}$, $\rho = 7870\ \frac{kg}{m^3}$, $\varepsilon_Y = 0.00026$), we obtain $\frac{a\,\dot{a}}{\Omega} \approx 2.3 \cdot 10^{-5} < 0.01$. This is indicative of a non-thermal growth regime, that is the influence of heat conduction appears to be non-negligible. This opens the possibility for improvements of the current model by introducing modifications to Eq. 44, that would result from incorporating a heat conduction term into the energy balance equation. At later stages of void growth during spall, however, voids grow much more rapidly, justifying a treatment using an adiabatic approximation [126]. Although the simplified analytical model presented here may not capture other effects that may play a role in void nucleation and growth, the 250 K temperature increase is similar to what is seen in MD. The incorporation of more complex dislocation phenomena and this promising result may pave the ground for future developments of such models. Additionally, experimental results predict density of geometrically necessary dislocations to be 10^{15}. This is a feasible quantity considering the assumptions taken in the analytical model and the underestimation of GND density from the EBSD maps.

Chapter 4, in part, is a reprint of material as it appears in: Righi, G., Ruestes, C. J., Stan, C. V., Ali, S. J., Rudd, R. E., Kawasaki, M., Park, H.-S., Meyers, M. A. Towards the ultimate strength of iron: spalling through laser shock. Acta Materialia 215 (2021). The dissertation author was the primary investigator and author of this paper.

Chapter 5: DCS Spall and Diffraction Experiments

5.1 Experimental and Computational Methods

Laser shock experiments were conducted at the Dynamic Compression Sector (DCS) of the Advanced Photon Source (APS) in Argonne National Laboratory. Time-resolved x-ray diffraction (XRD) was performed using an 80 μm by 50 μm 24 keV pink beam and recorded using a Rayonix SX165 detector. A 100 J, 351 nm laser with a 1 mm spot size and 10 ns pulse length was used to generate a shock wave. The facility diagnostics report that a 70 J energy pulse was delivered, lower than the nominal 100 J specification. A 30 μm polystyrene ablator was glued onto 50 μm iron foils of varying grain size (Fig. 5-1a). Single crystal iron ([001] orientation) from Surface Preparation Laboratory and polycrystalline samples (100-250 μm grain size) from Goodfellow were used. Velocity interferometer system for any reflector (VISAR) was used to record free surface velocity, which provided the peak pressure, strain rate, and spall strength. Point VISAR (VPF = 1.554, 0.945) and line VISAR (VPF = 2.068) were used in conjunction to verify velocity measurements (Fig. 5-1b). No sample recovery was possible, but the same foils were used in Chapter 4 so it can be assumed that post-shock characterization would have shown the same, or similar, results. Hydrodynamic simulations using Hydra were used to visualize the pressure profile in the iron sample and predict the x-ray timing (Fig. 5-1c).

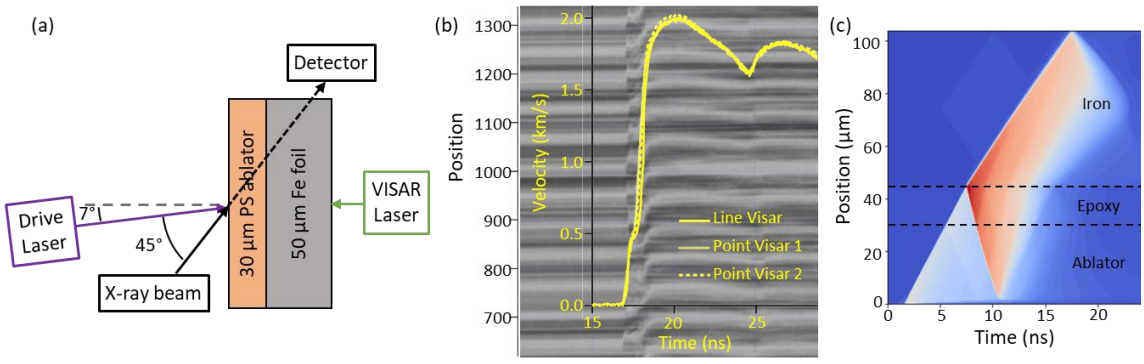

Figure 5-1. (a) Experimental set-up (not to scale) and (b) representative visar data (solid line represents line visar and dashed lines represent two channels of point VISAR). Zero time represents start of drive laser. X-ray probe timing (~100 ps) not shown. (c) x-t plot of pressure from Hydra simulations.

Molecular dynamic simulations of uniaxial compression were carried out using LAAMPS [88]. Body centered cubic (BCC) Fe polycrystals were modeled with an embedded atom method (EAM) potential developed by Gunkelmann and co-workers [87]. This potential was widely used due to adequately reproduce the α-ϵ transition [81,86,127]. Polycrystal samples were designed using Atomsk [80] with dimensions of $100a_0^2$, leading to 2 million atoms in 30 grains, with a mean grain diameter ~7 nm. Samples were compressed up to 15% along [001], at strain rates of 2×10^7 s^{-1}, 10^8 s^{-1} and 10^9 s^{-1}. Samples were held at this maximum strain for 20 ps. Finally, samples were unloaded by applying uniaxial tension along the same axis at the same strain rate, to achieve zero uniaxial strain and stress by the end of the simulations. All samples were created with periodic boundary condition (PBC). Energy minimization and box relaxation were performed for all samples before compression, for an initial temperature T_0=300 K, and zero pressure. Visualization

and analysis were performed using OVITO [89]. Crystal structure was identified with Polyhedral Template Matching (PTM) [91], using root-mean-square deviation (RMSD) equal to 0.1. PTM is generally more robust than other structure identification methods at high temperatures and pressures.

5.2 Spall Strength

The strength of each sample upon spall was calculated in a similar method to Section 4.2 using Equations 6 and 7. Preliminary results show that spall strength at strain rate of ~$8x10^6$ s^{-1} is consistent with our previous experiments, around 9.6 GPa and 7.5 GPa for single and polycrystalline iron, respectively. The peak pressure was calculated using the Hugoniot relationship between pressure and particle velocity, similar to Section 4.2. The pressure reached was ~55 GPa, above the phase transition pressure, and similar to previous experiments (Chapter 4). The spall strengths for single and polycrystalline samples follow a similar trend to other laser shock-induced spall experiments [54,101,127] – polycrystals have a lower spall strength than their single crystal counterparts (Fig. 5-2). It is expected that single crystal iron is stronger than polycrystalline iron during spall failure because of the lack of failure initiation sites. The many grain boundaries in polycrystalline materials act as preferential void nucleation and dislocation pile-up locations under tensile and shear loading [94]. It has been shown that in single crystal iron, the formation of twins and their associated boundaries during pressure release facilitates the formation of twin

boundaries, which become void nucleation sites as failure commences [127]. This failure behavior is typical of BCC metals like tantalum [98] and vanadium [99].

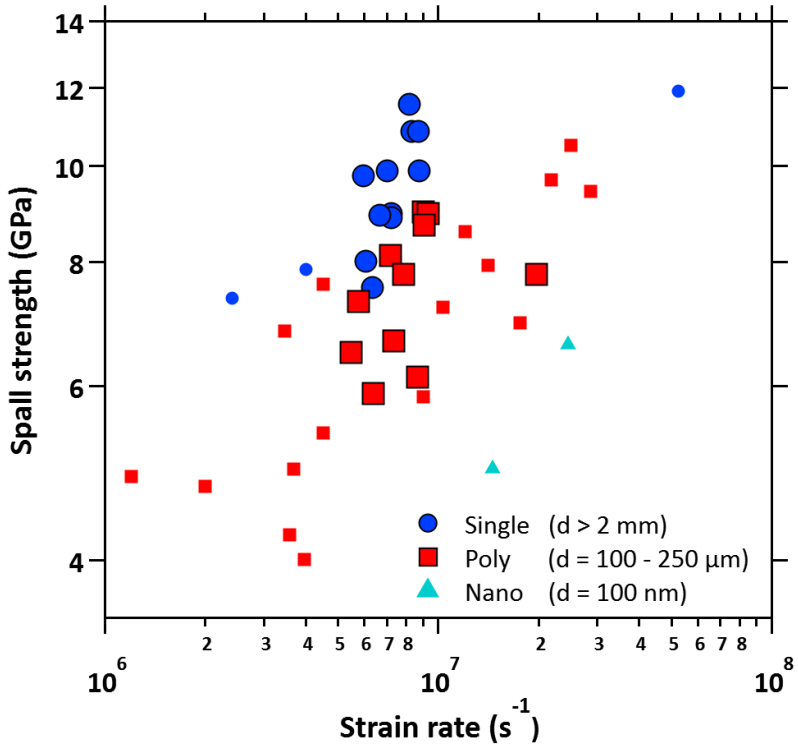

Figure 5-2. Spall strength versus strain rate on log-log scale with grain sizes from current experiments listed. Large symbols represent the current work from the DCS and small symbols represent literature data. References as follows: [49,52,100–103,127]

5.3 Crystal Structure

X-ray diffraction measurements were taken using a 100 ps x-ray burst at various delay times with respect to the laser start time. By adjusting this delay time, we were able to probe different moments during compression and release to reveal phase transition mechanics. XRD images were also taken before each data shot to reveal sample ambient structure. The sample data was azimuthally integrated using Dioptas [128] to determine

crystal structure. Using the corresponding lattice parameters for each phase we were able to estimate the pressure and temperature achieved during each shot. The kinetics of the phase transition is well studied [48,129–131] and is not the focus of this work. Instead, the effect of grain size on the phase transition timescale was investigated. In single crystal samples, the first measurement after shock breakout was at 1.23 ns, where the {110} BCC peak is just visible with very low intensity (Fig. 5-3a). Unfortunately, we do not have data points closer to shock breakout to resolve the time at which the HCP – BCC transition begins. After ~4.98 ns post-breakout, the transformation has evolved and shows largely BCC peaks. Exact determination of the phase evolution is complicated due to texture development of shocked single crystal iron, so will be the topic of future work. At late delay times, near the end of spall, the BCC phase is seen to have a transformation memory effect, where the microstructure shows strong single crystal character. This finding is in agreement with both diamond anvil cell [132,133] and laser shock work [52,127].

In polycrystalline samples (Fig. 5-3b), the return to a BCC structure also begins almost immediately after shock breakout, with the first signs of BCC peaks visible at 0.85 ns. Over the course of the shock release and subsequent spall, the phase transition completes ~8 ns. The exact duration of the ϵ-α transition is inconclusive due to large gaps in time, but the latest time point shows 97% has retransformed to BCC so 8 ns can be assumed to be reasonable. This time to restore a BCC structure is longer than previous

work with polycrystalline iron (2.1 ns in Hwang et al. [134] for $\dot{\epsilon} \approx 10^9$ s^{-1}), but this difference is expected due to the lower strain rate of experiments described here ($8x10^6$ s^{-1}).

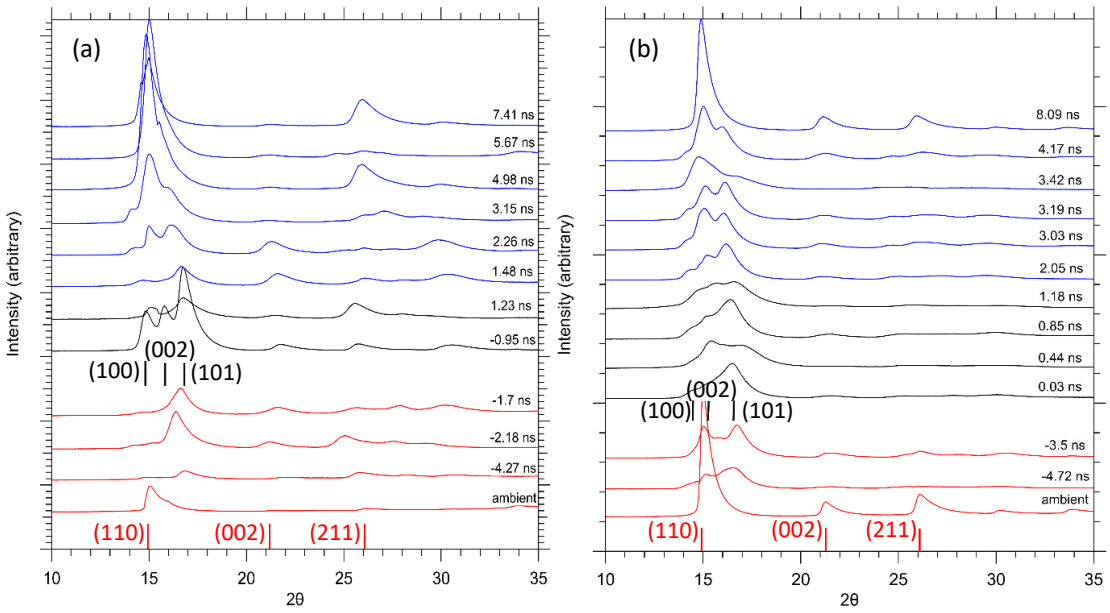

Figure 5-3. Preliminary diffraction results of (a) single and (b) polycrystalline iron. Clear transformation to HCP occurs during compression (red) while during release (black), structure reverts to BCC. After release, structure retains BCC character.

The weight fraction of BCC phase is determined using Rietveld refinement [135] with GSAS-II software [136], including the pink beam profile function described in Von Dreele et al. [58]. The resulting evolution from BCC to HCP is clearly seen during compression, or negative times, and the reverse transition occurs during release, or positive times (Fig. 5-4). The kinetics of this reverse phase transformation can be further described using a simple phenomenological rate equation: the Johnson-Mehl-Avrami-Kolmogorov (JMAK) model [137–139]. This type of formulation was originally designed to describe

material solidification processes but has been applied to solid-state phase changes as well [140,141]. This model describes the transformed volume fraction in an exponential form:

$$Y(t) = 1 - \exp\left[-Kt^n\right] \quad (47)$$

where Y(t) is the fraction of the material transformed as a function of time, t; K is a rate constant, and n is the JMAK kinetic exponent. This exponent can provide information about the nature of the phase nucleation process where the value can vary between 1 and 4, corresponding to heterogeneous or homogeneous nucleation. The best-fit parameters for the JMAK model to our data are K = 0.14 (± 0.05) and n = 1.38 (± 0.24). The exponential factor around 1 agrees with the theory that the presence of many grain boundaries in polycrystalline material causes phase nucleation sites to be non-random and restricted to 1-2 dimensions [142]. The rate constant can be used to determine the activation energy for the ε to α phase transition assuming the following Arrhenius form:

$$K = Aexp\left[-\frac{E_a}{k_B T}\right] \quad (48)$$

where A is a constant, E_a is the activation energy, k_B is Boltzmann's constant, and T is temperature in K. The pre-exponential factor, A, can be estimated as k_BT/h where h is Planck's constant. For a rate constant of 0.14 and temperature of ~1000 K (according to hydrodynamic simulations), the activation energy is ~4.4 x 10^{-19} J. This can be considered as the difference in Gibb's free energy of the α and ε phases.

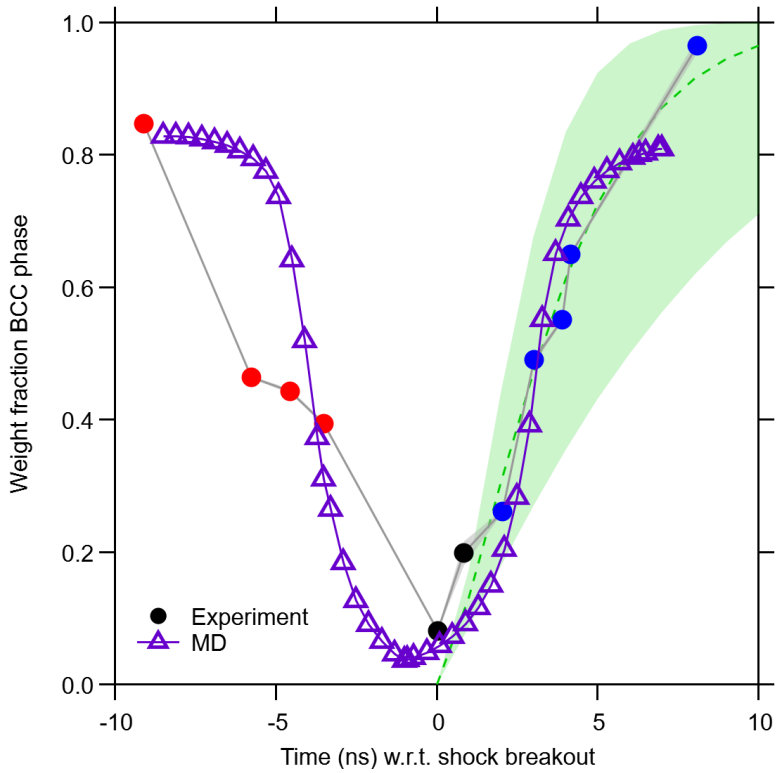

Figure 5-4. Weight fraction of BCC phase as function of x-ray timing. Experiments are shown in filled circles and simulations are shown in open triangles. Shading represents one standard deviation and dashed line represents fit according to Eq. 47.

The large unanswered question from the previous spall experiments (Chapter 4): is does the reverse phase transition return the microstructure to its original state? In-situ diffraction experiments have reported a reduction in grain size, down to ~10 nm, during the shock-induced phase transformation [51]. Therefore, it is a possibility that the initial microstructure would have no effect on the spall strength. Other laser shock-induced spall experiments show that single crystal iron has a higher spall strength and a ductile fracture surface while polycrystalline iron is softer and spalls along grain boundaries [52], consistent with the previous spall study [127] as well as spall studies in other metals. This

leads to the idea of a microstructural memory effect that results from the release in compressive strain. The diffraction experiments described here also find a similar memory effect, both on the microstructural scale and the atomic scale. During compression, the single crystal BCC structure clearly transforms to HCP (Fig. 5-5a) and remains as HCP Fe shortly after shock breakout as well (Fig. 5-5b). After the complete transformation back to α-Fe, the single crystal diffraction patterns show a 100% BCC structure with single crystalline character (i.e., diffraction spots rather than rings) (Fig. 5-5). These patterns show, qualitatively, that the single crystal iron maintains its single crystallinity throughout the phase transformation cycle, with minimal, or even no, grain size reduction. This finding contradicts the well-known findings of Hawreliak and Kalantar of drastic grain size reduction during shock compression of iron [51,143]. This can be due to the following: the phases retransform in the opposite order in which they transform. The orientations return to the original ones. Such is the case for the shape memory effect. Further effort on this will be conducted in future work. The polycrystalline data, however, can be analyzed for grain size evolution. The shock-induced changes in microstructure can be extracted from GSAS-II [136], including the pink beam profile function describe in Von Dreele et al. [58] Typical Scherrer broadening (Eq. 9) [56] predicts that the HCP grains become reduced to 10's of nanometer in size. At later times the domain size is seen to being recovering as well.

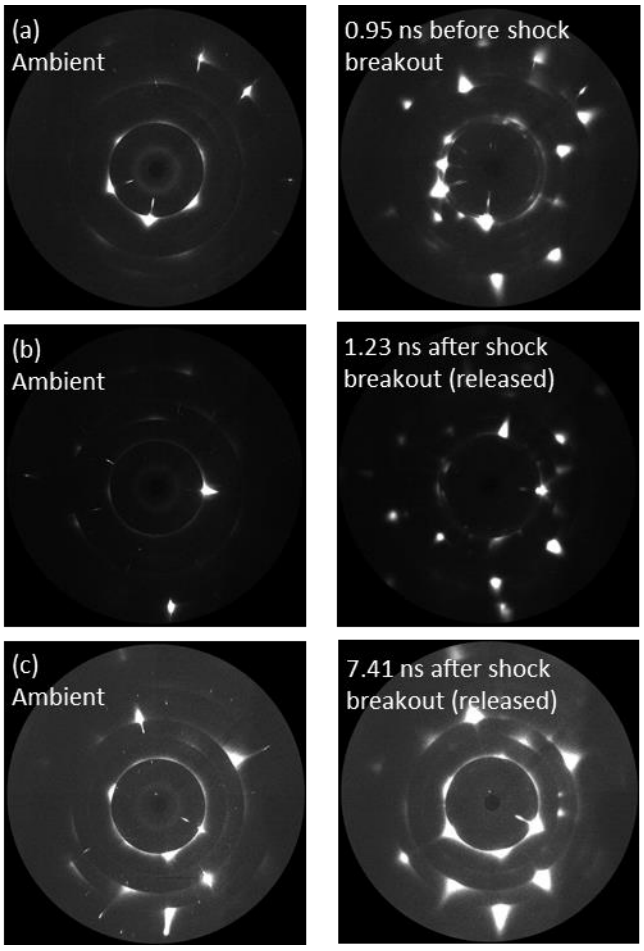

Figure 5-5. Qualitative comparison of single crystal showing clear single crystal peaks (with possibly minimal grain size reduction). (left) ambient and (right) as-shot diffraction image for (a) before shock breakout, (b) soon after shock breakout, and (c) late time after shock breakout.

5.4 Molecular Dynamic Simulations

The Molecular Dynamic simulations shows that as the sample is compressed, the α to ϵ phase transition takes place within each grain, preserving the initial grain boundary structure. During release, the reverse transition (ϵ to α) takes place and all samples return to their initial microstructure, further supporting the experimental hypothesis that the

reverse phase transition may return the microstructure to something like the starting material. Similar conclusions were obtained in previous MD studies of uniaxial compression and release of polycrystalline iron [84,127]. These processes take place before any spallation event. The result observed in the experimental shock are compared with MD simulation of compression and release. The peak stress obtained in MD varies between 43.12 – 46.75 GPa; all samples present similar stress-strain behavior. The phase transformation starts at ~7.5% compression and no residual strain is seen at 0 GPa. Due to imperfect grain boundary atoms, a small number of BCC and HCP atoms are identified at ~15% (compression) and 0% (release) strain. At peak compression the structure is almost entirely HCP, with many intragranular twins (Fig. 5-6). As the sample begins unloading, the BCC phase is seen to being nucleating at grain boundaries. This simulated phase nucleation process agrees with the finding described in the previous section (JMAK exponent ~1). The large amount of twins also agrees with MD results described in Section 4.4.

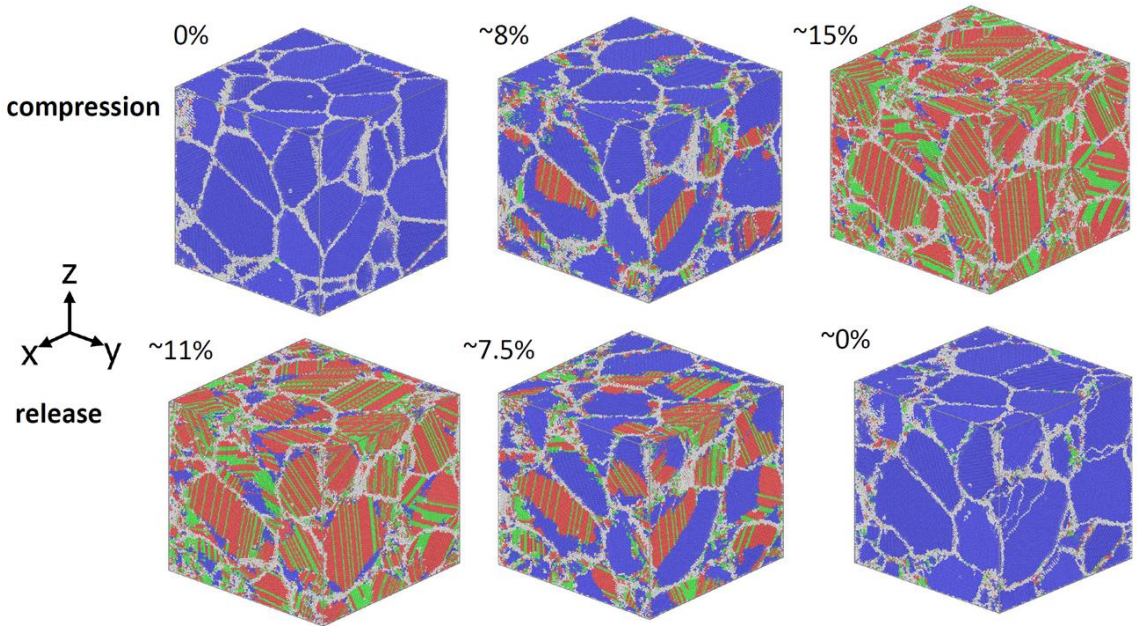

Figure 5-6. Molecular dynamics simulation showing (top) compressed and (bottom) released structures for nanocrystalline iron. Colors represent crystal structure. Red: HCP, green: FCC, blue: BCC, yellow or gray: other

The time to restore the BCC structure is calculated at various strain rates and compared against the experimental results as well as a previous study [84]. To measure the HCP-BCC transformation time in the simulations, the difference between the structure at 15% and 0% strain was considered. At the largest strain, there are ~3% BCC atoms whereas after the structure has been released, ~81% atoms are recovered. The experimental result of ~8 ns is in good agreement to the fit shown in Fig. 5-7 that predicts a time of 11 ns for $\dot{\epsilon} \approx 8\text{x}10^{6}\ \text{s}^{-1}$. This is excellent agreement considering the simulations are using much smaller grains, much higher strain rates, and much lower temperatures.

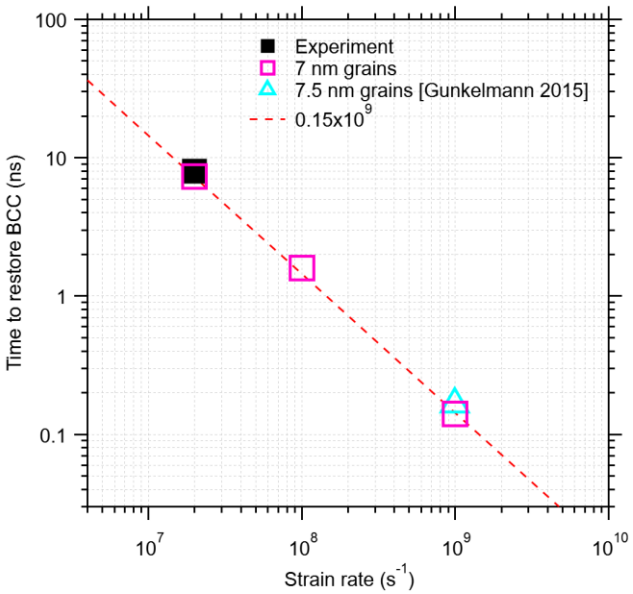

Figure 5-7. Time to restore the BCC structure for single crystal (experiment: black transparent circle and MD 2 & 4 million atom single crystal simulations: blue circle & orange diamond) and nanocrystalline (experiment: black transparent square, MD simulation: pink squares, and literature: purple diamond). Fits to the simulated data (red lines) represent different strain rates.

The spall strengths calculated here agree with previous work on laser shock-induced spall in iron with single crystal being stronger than polycrystals. The α-ε phase transition is observed during compression and is accompanied by a grain size reduction down to 10's of nanometers. In the single crystal case, further analysis is required to determine microstructural evolution. The reverse phase transition, ε-α, occurs during release prior to complete spall. This phase change occurs within ~8 ns at strain rate of ~$8x10^6$ s^{-1}. This is longer than previous experimental work on the subject (at higher strain rates), but is in close agreement with Molecular Dynamic simulation of the experiment.

Chapter 5, in part, is a reprint of material that has been submitted: Righi, G., Briggs, R., Deluigi, O., Stan, C., Singh, S., Clarke, S., Bringa, E., Smith, R., Park, H.-S., Meyers, M. A. Spalling and x-ray diffraction in iron: a study of the ε-α reverse phase transition. Physical Review B (2022). In prep. The dissertation author was the primary investigator and author of this paper.

Chapter 6: NIF Strength Work

6.1 Computational Design

Plastic deformation of metals is a complex process that, as stated by Cottrell, was one of the first to be studied and one of the last to be solved [144]. The stress that the material can sustain is a function of internal and external parameters. The internal ones are the multiple levels of the structure, from the nano- to the macro-scale. The external ones are the thermodynamic parameters of pressure, temperature, as well as the strain rate. Modeling this response is done, at the engineering level, by simple phenomenological equations such as the Johnson-Cook model [65]. More fundamental, physically based approaches incorporate a daunting complex of effects including thermally activation dislocation motion, viscous drag, relativistic effects, and additional contributions from grain size or other imperfections. The Preston-Tonks-Wallace (PTW) model [68] represents an apex constitutive equation that covers the range of strain rates from 10^{-3} to 10^{12} s^{-1} and is well suited for shock compression. By performing these experiments at extreme conditions, this type of commonly used constitutive equation can be validated in this regime.

Iron poses unique challenges to the design of effective ramp compression experiments that are sensitive to its strength. The structural alpha-epsilon phase transformation occurs at ~5% of the Earth's inner core pressure and is unavoidable. It complicates the design in several ways: (i) standard iron strength models developed for the alpha phase cannot be

expected to extrapolate well into the epsilon phase for the purposes of design; (ii) this uncertainty is further complicated by likely microstructural changes affecting strength and heating associated with the significant volume collapse, both resulting from the phase transformation; and (iii) the inability of indirect-drive designs to produce a broad range of temperatures at a prescribed pressure. The Rayleigh-Taylor (RT) instability induces material deformation, enabling a method to determine the material's strength when traditional measurement capabilities, like strain gauges, are inadequate under high-pressure (> 100 GPa) and high strain rate (> 10^7 s^{-1}) conditions. This instability occurs at the interface of two fluids of different densities by virtue of the lighter fluid accelerating into the heavier fluid [72,73]. RT strength experiments at state-of-the-art laser facilities such as the Laboratory for Laser Energetics (LLE) and the National Ignition Facility (NIF) have been developed over many years [21,145,146]. The growth of RT unstable perturbations for an ideal fluid depends on the Atwood number ($A = (\rho_2 - \rho_1)/(\rho_2 + \rho_1)$, where ρ_1, ρ_2 are densities of the interface materials), acceleration, and perturbation wavelength. This growth can be inhibited in real fluids through a variety of mechanisms: self-radiation [147], thermal diffusion [148–150], convection [151], ablation [152–154], "snow-plow" [155], and viscosity [156]. Similar to viscosity, the strength of a material can be inferred by comparing the difference between the initial and final perturbation amplitudes [157]. If the material has no strength, the ripple growth will be uninhibited and grow at the classical rate, however if the material has a finite strength, growth will be suppressed. In the linear

RT regime, the amount of RT suppression can be used to infer a measure of strength and the96ipplee growth can be measured by face-on x-ray radiography.

Experiments are being conducted at LLE (using the Omega EP laser [24]) and the NIF [25] to study iron strength under a variety of conditions of pressure and temperatures using direct-drive (DD) laser shots. For direct-drive experiments, ramp compression is achieved by laser pulse shaping. A new RT campaign at Omega EP is designed to investigate the temperature dependence of iron strength at high pressure (100 GPa). Hohlraum-driven RT experiments at 130 GPa and relatively low temperature found the strength of iron to be ~40 GPa [157], but moderate strain rate shear plate impact experiments and static diamond anvil cell experiments yield much lower strength [158,159]. The NIF can achieve higher pressures (P~350 GPa) and temperatures (T~5000 K), comparable to Earth and exoplanet interiors. Few experimental studies exist for iron strength at these conditions. Surprisingly, EXAFS results for the plastic-work-induced temperature rise during ramp compression imply an enormously high strength of 60 GPa [160]. Other promising techniques like in-situ x-ray diffraction are not yet able to reach suitably high pressures [161]. The iron RT experiments currently being conducted at the NIF aim to resolve discrepancies in the literature and determine the strength of iron at Earth core P-T conditions. The hohlraum-driven, or indirect-drive, platform is well developed at the NIF [101,162–165] and has been used for a few iron RT experiments. Although hohlraum-driven experiments are successful at reaching Earth core pressures, the

temperature is significantly lower than desired – about a third of the core temperature. This is because the current hohlraum design was optimized for higher-Z materials, like tantalum or lead, and so does not perform as well for iron. Intensive design work could be used to develop this indirect-drive platform for iron, but finer control can be achieved using direct-drive laser pulse shaping so the authors focus on that design work instead. Furthermore, usage of a hohlraum is subject to gold plasma filling in the space where the laser beams ablate the inner walls, resulting in compromised radiography data for low-Z RT experiments such as iron. These issues have pushed the development of the direct-drive platform in which conditions can be precisely controlled through target design and laser pulse shaping. These DD iron RT experiments are the first of their kind to take advantage of the uniquely adjustable long (60 ns) pulse shape to reach hundreds of GPa and high-temperature conditions. These experimental RT laser campaigns rely on hydrodynamic simulations to design both target and pulse shape for the desired conditions and predict strength. A description of the computational methods is presented in Section 6.2. Results for the target design, pulse shape, and the subsequent strength effects are presented in Section 6.3.

6.2 Simulation Methods

The direct-drive design reported here uses shaping of a laser pulse to drive a multilayer target including ablator, pusher, sample, and tamper materials. The uniquely long (60 ns) laser pulse is only available at the NIF since it is the only facility with the capability of stitching together 16 beams. Furthermore, the NIF has incredibly fine control,

both spatial and temporal, over the laser drives it can produce. The models used for each layer of material are listed in Table 6-1 where early simulations find that the thin applications of glue, typically <3 mm, used to adhere layers together are of negligible thickness and strength. The materials in the layers around iron have relatively low strength, so no strength models are used for Be, BrCH, epoxy, or LiF. If a thick material with significant strength is used next to the iron ripples, then the experiment will not produce accurate results for iron strength. Unlike the case of pressure-shear loading experiments [166], these materials and the glue layers that bond them do not need to be strong enough to transmit the large shear stress that forms in the iron. Each material layer has a 0.5 μm mesh size except for the Be ablator, which has a finer ablative mesh to ensure that laser energy absorption is modeled correctly. A mesh convergence study was run in Ares to ensure that a 0.5 μm mesh is well converged – there is < 5% difference in growth factor for a smaller mesh so it was concluded that this mesh size is enough to get reasonable growth factor predictions for a long enough run time (i.e., before mesh tangling ends the simulation). Boundary conditions are also applied to reduce computational cost. The sides of the target are set such that they act as reflecting boundaries. The front of the target is set such that it remains fixed for the entirety of the simulation and the back of the target is allowed to move freely.

Table 6-1. Materials used in the simulations.

Material	Thickness (μm)	Density (g/cm^3)	EOS	Strength model
Be	70	1.858	LEOS 40	N/A
12.5% BrCH	75	2.0	LEOS 5128	N/A
Epoxy	20	1.185	LEOS 5030	N/A
Iron	50	7.877	LEOS 260	SG x 0, 1, 2, 5
		7.85	SESAME 2140	α-PTW
		7.874	LEOS 263	ε-PTW
LiF	500	2.64	LEOS 2240	N/A

Strength is a characteristic property of materials and dictates behavior in many applications. At low levels of applied stress, the material lattice simply distorts elastically in a reversible fashion and can return to its original configuration. With increased stress, however, the lattice permanently shifts, and deformation occurs at all levels from the nano- to the macro-scale. The resistance to that deformation is the basis of strength. At large strain rates, the mechanics of deformation becomes complicated. Dislocations, the primary carriers of permanent deformation, are governed by thermal activation at slow strain rates, and viscous drag and relativistic effects at higher strain rates. Their collective behavior is

described by analytical models or through computations. The SG model (Eqs. 14-16) and PTW model (Eq. 17) are used to model these RT experiments.

The EOS of a material is required in computations to connect the conservation laws. Iron has multiple EOS models available, three of which are investigated here: LEOS 260 [167,168], SESAME 2140 [169], and LEOS 263 [170]. The SESAME and LEOS 263 models are multiphase forms that account for the high temperature and pressure solid-state phase changes in iron, while LEOS 260 does not distinguish between the various solid phases. The epsilon phase of iron extends from ~13 GPa to pressures well above 400 GPa [101,171]; it has been proposed that at 350 GPa there is a high-temperature body-centered cubic (BCC) phase of iron and it is that phase of iron in the Earth's inner core [172]. However, many other publications, both at low [132,133,171,173–175] and high strain rates [101,143,176–179], find that the HCP phase is stable at core pressures and up until melt [180], and the equations of state used here do not include a high-pressure BCC phase. The equations of state of the proposed BCC phase and the hexagonal epsilon phase are very similar and the small differences have no effect on this design. Figure 6-1 shows the shock Hugoniot and melt curve for each model. There is little difference in the Hugoniots at low P-T conditions, but the models begin to deviate around 150 GPa. The melt temperature as a function of pressure is much lower for LEOS 263, meaning that it predicts melting at a lower temperature for a given pressure state.

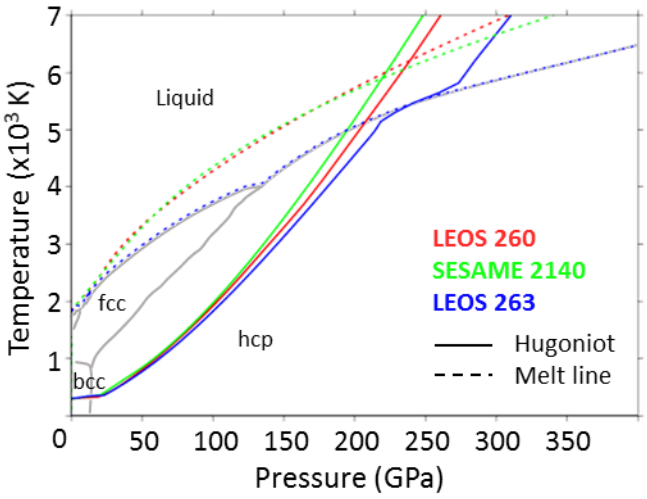

Figure 6-1. Shock Hugoniot and melt curves for the three iron EOS models used. The solid-solid phase boundaries (grey) correspond to the newly developed LEOS 263 model (courtesy of Wu [170]). The LEOS 263 phase boundaries and melt curve agree with data from various static [181–183] and dynamic [180,184,185] work.

6.3 Simulation Results

6.3.1 Target Design

The design of the target is based on previous experiments [146,186] using beryllium (Be) as the ablator material, followed by 2-12% brominated plastic (BrCH) which acts as the shield layer against x-rays generated by laser ablation that can heat the iron sample. The shield layer is followed by a low-density rippled epoxy which allows RT unstable ripples to grow by providing a relatively high Atwood number at the interface. Metal foams instead of an epoxy layer have also been postulated to be suitable, retaining a low-density post-shock compared to fully dense transition metals, but our simulations show the foam's high shock temperature and thermal conductivity cause premature melting in the iron. The

epoxy interfaces with the rippled iron foil, which is backed by lithium fluoride (LiF) that acts as a pressure tamper.

Since the role of the ablator is to produce a plasma that rapidly expands, causing a pressure wave to travel into the target, these simulations show that a thicker Be results in higher peak pressure and lower peak temperature in the iron (Fig. 6-2). The increased pressure is the result of pressure waves interacting and growing as they travel through thicker material. The lower temperature occurs because there is physically more material, which causes heat to dissipate more before reaching the next layer.

The x-ray/heat shield material is crucial in preventing unwanted heating in the iron due to x-rays. This ensures that any temperature increase is solely due to plastic work hardening and therefore, related to material strength and comfortably below melting. The pressure is relatively insensitive to the BrCH thickness and Br doping level (Fig. 6-2). The temperature, however, is sensitive to thicker BrCH or higher %Br. These two factors greatly reduce the temperature at the front of the iron as well as improve temperature stability. The higher-atomic number (Z) bromine increases opacity and restricts the transfer of energy (heat) throughout the material. An additional factor needs to be considered when a thicker heat shield is used: ripple radiography backlighter x-ray transmission for image plate data collection. A thicker heat shield or higher %Br has the effect of decreasing the transmission of the backlighter x-rays – impeding the radiography signal level.

The use of thicker rippled epoxy (10 – 40 μm) improves the overall pressure behavior, resulting in fewer reverberations. If a pressure wave interacts with a boundary where the sound impedance changes, wave reflections and interactions are generated. For a thinner epoxy layer, the front and back boundaries are close to each other, and the various pressure waves are reflected and interact much more, causing large reverberations. A thicker version simply allows some of the reflected waves to dissipate, lessening and delaying the pressure jumps. A thicker epoxy layer also causes lower temperature in the iron due to heat dissipation effects (Fig. 6-2).

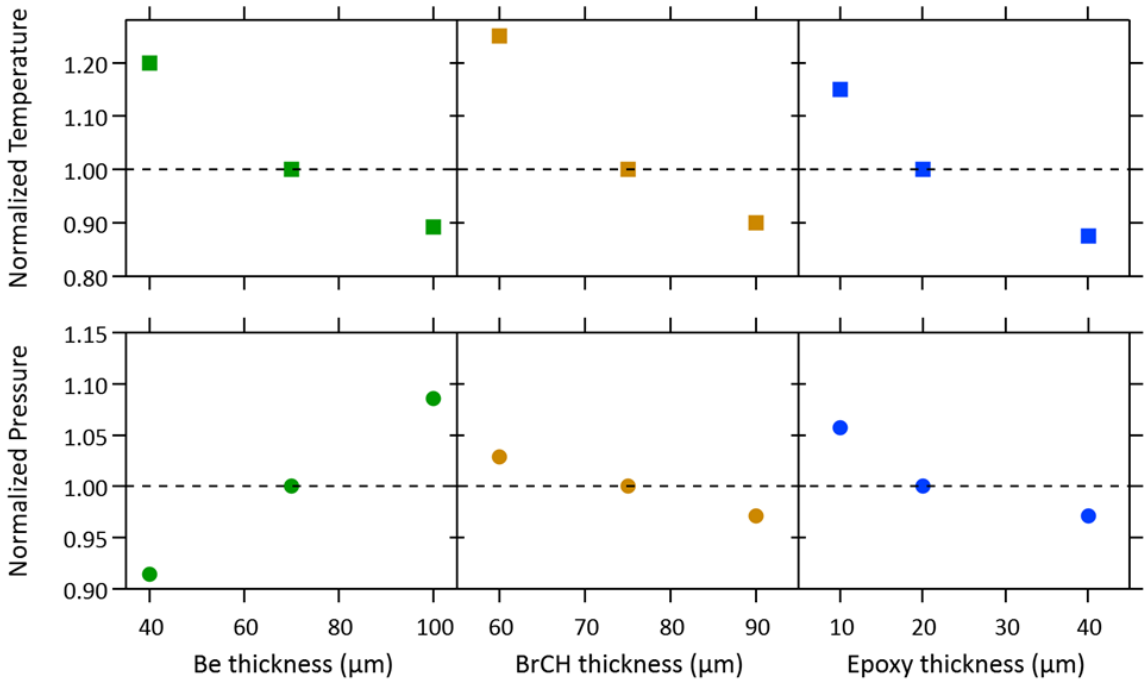

Figure 6-2. Normalized pressure and temperature as a function of material thickness where normalized value of 1 corresponds to P = 350 GPa and T = 4000 K. Variations in material thickness shown here are representative of all the options that were simulated for this work.

6.3.2 Pulse Shape Design

The laser pulse shape ramps up in power to help ensure the iron does not melt before reaching the desired P-T conditions. Three aspects of the pulse shape were investigated – initial shock-inducing jump, picket addition, and "hold" time. Inducing a shock at the beginning of the pulse is an easy way to initialize the sample into a specific P-T state along the Hugoniot to reach more extreme conditions. Since a shock generates on-Hugoniot compression, the temperature can be easily predicted, i.e., an initial shock of 100 GPa should increase temperature to ~2000 K. A picketed pulse is set by dropping the laser power after an initial shock pulse. The picket pulse is timed in such a way to destructively interfere with reverberations from sample interfaces. Including a picket reduces the severity of the pressure drop at early time as well as causing a slight reduction of temperature at the iron front. It is important that the picket does not cause the iron to revert to the α phase (< 13 GPa), avoiding unnecessary phase transitions. This is accomplished by keeping the laser power after the post-picket power drop to above 0.03 TW. Lastly, the late time "hold", which is a monotonic increase in power, is used to create a stable region in time at the desired pressure. A longer "hold" results in more time at peak pressure, but also causes significantly more heating (and premature melting). By using a 60 ns pulse shape, rather than 30 ns, the peak pressure can be held for longer time and the ramped portion can be more gradual, allowing for more time during which $T/T_m < 1$. This is the

only feasible way to make a solid-state iron strength measurement at the extremely high pressure and high temperature of interest.

The optimized target and pulse shape design are shown in Fig. 6-3. The target consists of a 70 μm Be ablator, 75 μm 12.5% BrCH heat shield, 20 μm epoxy, 50 μm iron, and 500 μm LiF. The pulse is made up of a 6 ns 0.2 TW picket, drop to ~0.1 TW, ramp, and "hold" to a peak power of 2 TW. In the experiments, this pulse is delivered to the target by 16 NIF beams (Fig. 6-3a). At a prescribed delay time a separate set of 12 NIF beams illuminates a thin foil which causes x-rays to be emitted and backlight the ripple target for face-on radiography. The desired 350 GPa pressure state is maintained for ~10 ns (Fig. 6-4a), while the ideal 5000 K temperature condition is not quite achieved. A peak temperature of 4000 K is reached for a few nanoseconds (Fig. 6-4b). The iron also remains in the solid state ($T/T_m < 1$) for the entirety of the simulation (Fig. 6-4c). Experimentally the measurement will be made at peak pressure, between 50 and 60 ns.

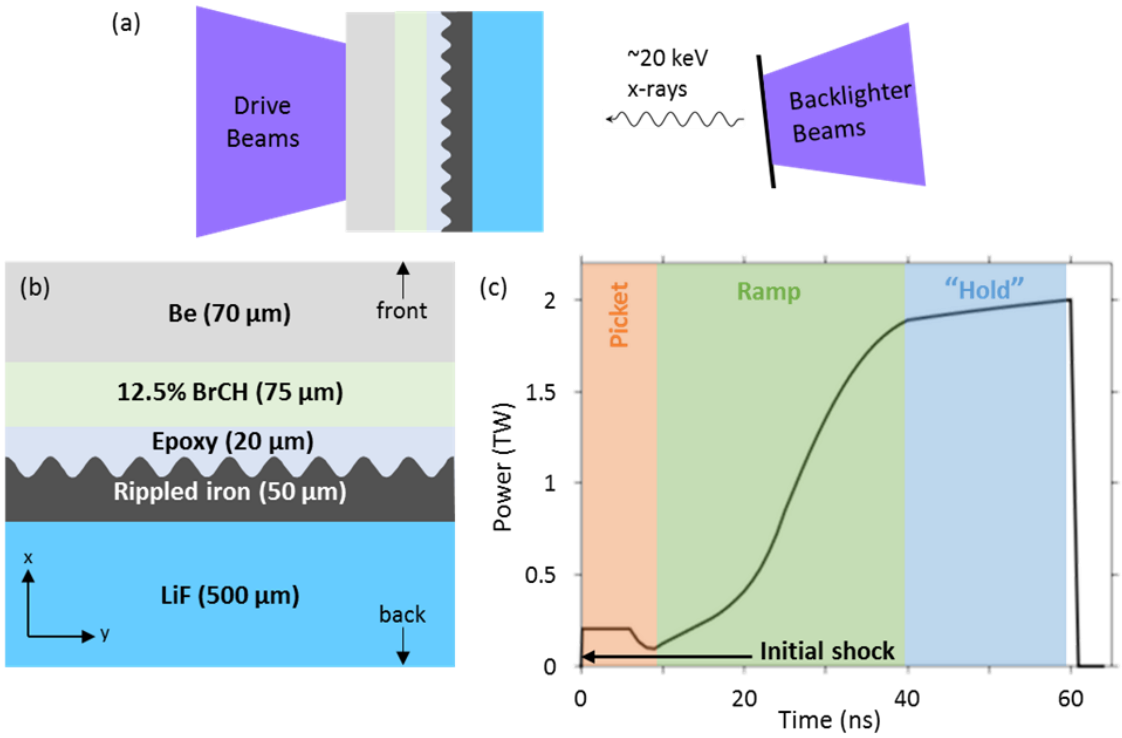

Figure 6-3. (a) Experimental configuration, where the sample is compressed by a set of NIF laser beams. The ripple growth is measured with face-on radiography from laser illumination of a backlighter foil to produce x-rays. Backlighter energy is dependent on foil material. Optimized (b) target and (c) pulse shape designs. The epoxy is applied directly to the iron ripples. The other layers are joined by thin (<3 µm) layers of epoxy (not shown) that have no effect on the growth factor in the RT design simulations.

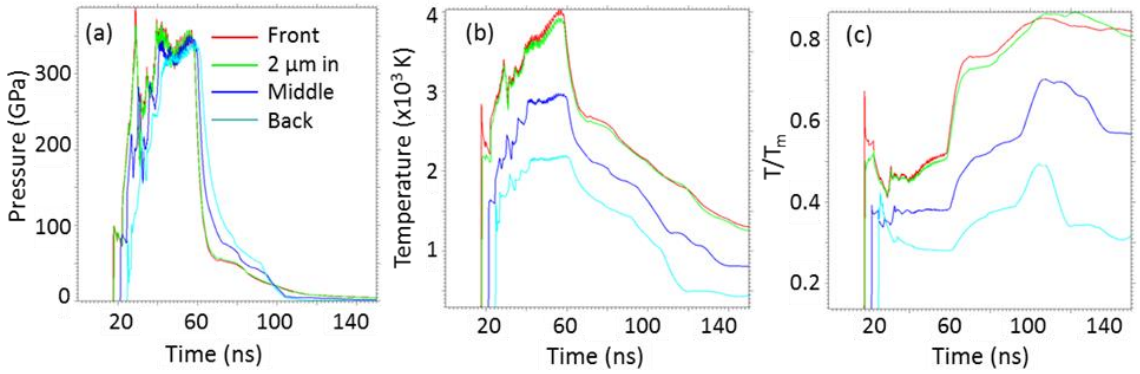

Figure 6-4. Hydra simulations of (a) pressure, (b) temperature, and (c) T/Tm in the iron at different locations. Red, green, blue, and teal curves correspond to various locations in the iron layer: front (rippled face), 2 μm in, middle, and back, respectively.

6.3.3 Strength and EOS Effects

The effect of strength on the RT instability was investigated with 2D Ares simulations (Fig. 6-5). By introducing a sinusoidal ripple pattern onto the front surface of the iron, the effect of strength can be inferred by measuring the growth factor (GF). The growth factor is essentially the ratio of the final and initial ripple areal density, that is, the multiplication of amplitudes by density. In practice, blurring of the ripple image in the experiment due to geometry and other factors must be accounted for by dividing GF by the modulation transfer function [187]. The simulations predict values for the von Mises flow stress while experimental RT measurements are a measure of the flow stress (half the von Mises stress [68]). For a 1 μm amplitude and 75 μm wavelength ripple pattern, the peak growth factor for iron with different levels of strength varies from 3-10 (Fig. 6-6). Growth factors in this range will provide a robust signal to noise in the collected radiography data. Here

SGx0,1,2,5 multipliers refer to multiplying the Y_0 parameter and maximum yield strength from work hardening ($Y_{wh,max}$) by the specified scale factor essentially scaling the flow stress. The 0 multiplier represents no-strength case. In a no-strength case, the iron behaves like a liquid and the perturbations exhibit classical, or uninhibited, RT growth. In this case the growth rate is proportional to the square root of the Atwood number ($\gamma = \sqrt{Aka}$, where k is wavenumber or 1/wavelength and a is acceleration, so that $GF=e^{\gamma t}$ in classical growth). The original SG and α-PTW strength models predict similar growth behavior – peaking at GF~10. The ε-PTW model [188] with GF~4 is constructed to give the strength of the high-pressure phase and is expected theoretically to best predict experimental results. 2x and 5x multipliers of the original SG model also predict less growth, indicating even higher iron strength. The range of growth factors predicted here corresponds to strengths ranging from 3 – 30 GPa at strain rate of $\sim 5 \times 10^6$ s^{-1}, with the ideal ε-PTW model predicting strength of 5 GPa (much lower than the value found by Huntington et al. (> 40 GPa) [157]). Note that those RT experiments were carried out at lower pressure (150 GPa) and likely lower temperature (not reported).

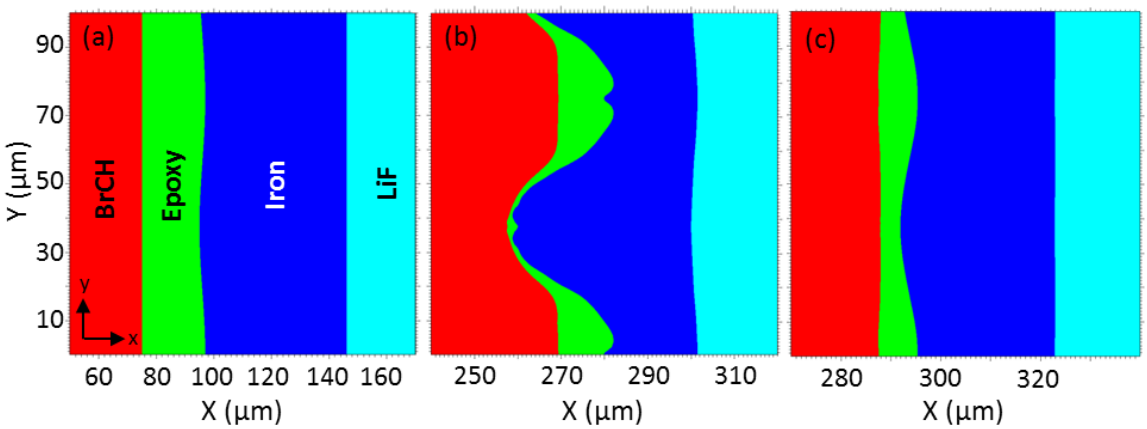

Figure 6-5. Ripple growth time sequence starting at (a) t = 0 with initial ripple pattern of 1 μm amplitude and 75 μm wavelength. Late time ripple growth (t ~ 55 ns) for (b) no strength and (c) high strength (SG x 5) cases assuming LEOS 260 model. Material layers are BrCH (red), epoxy (green), Fe (blue), and LiF (aqua). BrCH and LiF layers are cropped for better view of ripple growth.

The equation of state, or more specifically the melt curve associated with it, can also have a pronounced effect in predictions of the growth factor because depending on the model, T/T_m can be greater than 1 at different times. The melt curve of LEOS 263 lies at higher pressures than that of the other EOS tables used (Fig. 6-1), meaning the iron melts at lower temperature and potentially, earlier time. If the iron sample were to melt at an earlier time, the growth factor would follow the classical zero strength case and be much higher. Designing the target in such a way to make sure the sample does not melt until late in time helps to ensure we are taking an accurate solid-state strength measurement at the desired P-T conditions. The predicted ripple growth based on the EOS table used does not vary greatly (Fig. 6-6) and the predicted yield strength and strain rate at a given time are similar between EOS models.

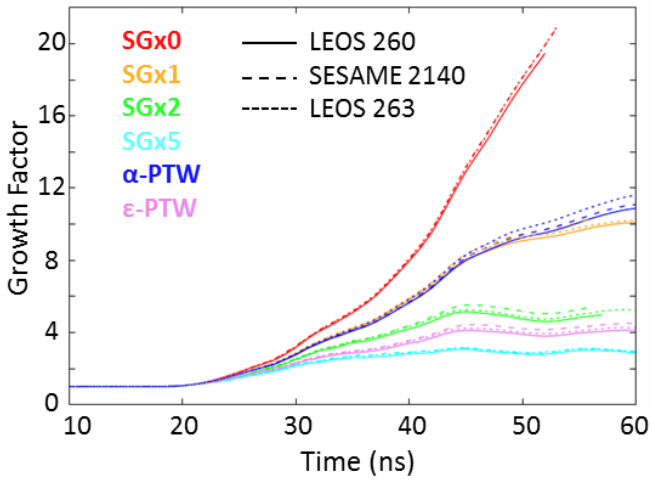

Figure 6-6. Growth factor calculations using 2D Ares for 1 μm amplitude/75 μm wavelength ripples in iron with different strength models (indicated by color) and EOS tables (indicated by line style).

We have described the computational design work for high-pressure iron Rayleigh-Taylor strength experiments at the NIF. The lack of clear experimental results on iron strength at high pressure and temperature conditions comparable to the Earth's inner core motivates these direct-drive shots which need extensive design as they have never been attempted before. Design work for the high-power direct-drive laser experiments is a complicated process of carefully balancing target components and pulse shape with the physical limitations of target fabrication and power limitations of the laser facility. The target components and pulse shape were optimized to produce the desired high pressure and temperature conditions. These extreme conditions require a design that induces a solid-solid phase transformation in the iron and take it to temperatures that approach melt. The effect of various strength models and EOS tables on ripple growth was investigated to predict experimental results and accommodate the large theoretical uncertainty in the iron

strength. Growth factors of 3-10 are predicted based on the optimal target and pulse shape with minimal variation based on the EOS used.

The desired pressure state in the iron is achieved using a picketed pulse followed by a smooth ramp and a "hold" up to 2 TW peak power. This design is the first example of how a longer (60 ns) pulse provides improved design options. Pressure is relatively insensitive to changes in target layer thicknesses, while temperature is highly variable. The P-T state of 350 GPa and 4000 K in the iron is achieved using a beryllium ablator (70 μm), brominated plastic heat shield (75 μm), epoxy pusher (20 μm), and lithium fluoride tamper (500 μm). Thinner layers before the iron can help to reach even higher temperatures but with a trade-off of the stability of the temperature state. Higher peak power in the pulse shape can also increase temperature, but with a danger of premature melting as well as power limitations of the NIF laser beams. Similar principles are applied to design Omega EP RT strength experiments where different peak temperatures can be achieved by changing the strength of the initial shock-inducing power jump in the pulse shape. This uniquely optimized design will be able to provide strength measurements of iron at extreme conditions adding to high-pressure materials science and providing iron data in a regime where the paucity of data to inform geophysical models is acute.

6.4 Experimental Methods

Ramp compression experiments were performed at the NIF using the 3.5 Mbar indirect drive platform (Fig. 6-7a) and a multi-component iron target. This allows for a

strength measurement to be taken at Earth core conditions of 350 GPa and high temperature. The strain rate for these experiments is on the order of 10^8 s^{-1}. The typical reservoir-gap configuration for this platform consists of a 155 μm CH heat shield, 245 μm aluminum x-ray absorber, multi-layered foam assembly to shape the pressure pulse, 1360 μm gap, and a 42 μm PVDF heat shield followed by the rippled iron sample and a HDC tamper (Fig. 6-7b). The rippled sample was made by General Atomics through the coining process in which the metal is heated and compressed with a precision machined die of a specified ripple pattern. The second target had an additional quartz window for free surface velocity measurements.

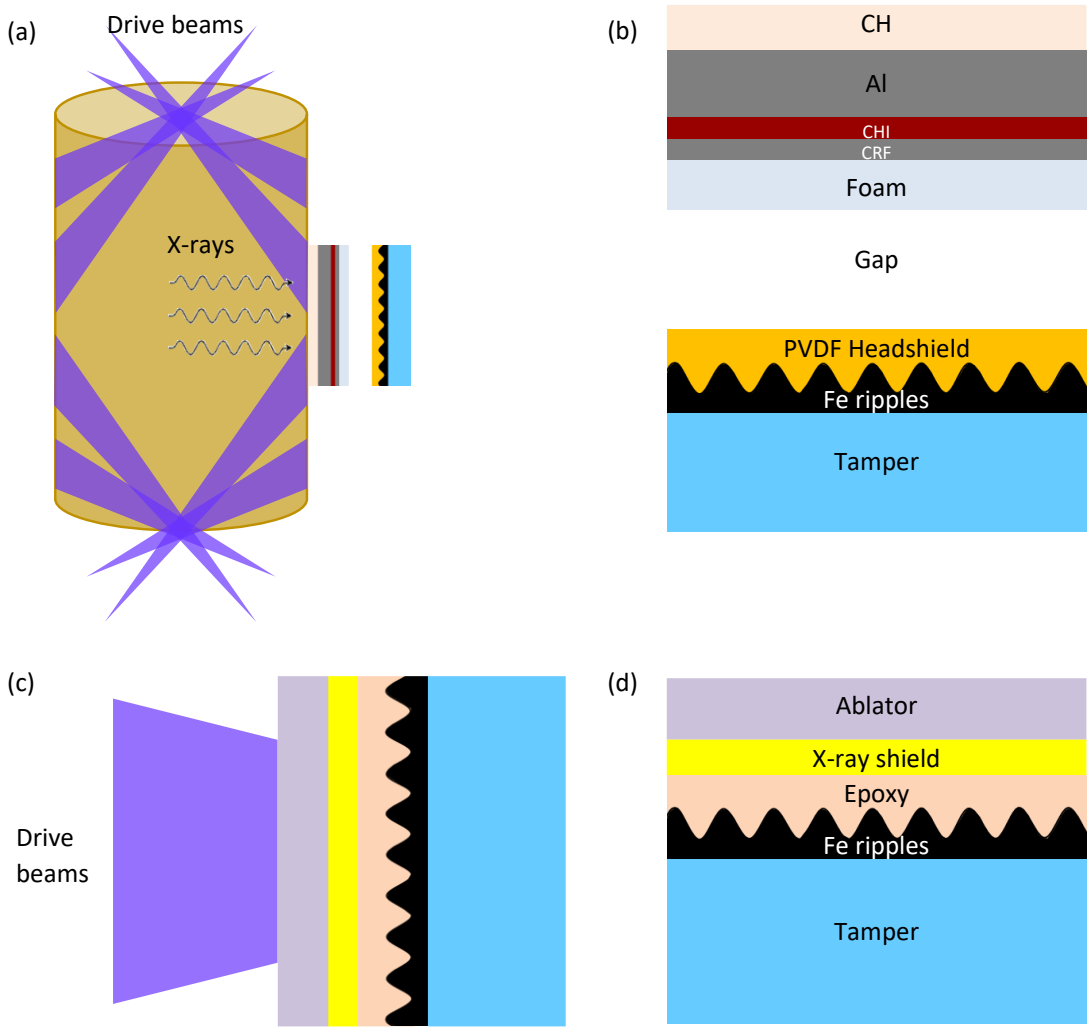

Figure 6-7. (a) Indirect drive platform using hohlraum-based design and (b) corresponding target design for ramp compression. (c) Direct drive platform and (d) corresponding layered target design.

For these experiments, 160 laser beams delivered a 2.7 ns square pulse to a gold hohlraum with a total power of approximately 1.85 TW. The illumination of the beams onto the inner hohlraum wall generates x-rays which then ablate the surface CH layer and, upon breakout, a shock wave is launched through the target package. The wave stagnates

on the heat shield and iron sample, creating the 3.5 Mbar ramped pressure pulse that allows RT unstable ripples to grow. The perturbation growth is labeled as the growth factor ($GF=\rho\Delta R_{final}/(\rho\Delta R_{initial}*MTF)$ where $\rho\Delta R$ is the measured areal density and MTF is the modulation transfer function, which quantifies backlighter diagnostic spatial resolution [187]. The iron portion of the target has additional calibration features that assist in data analysis (Fig. 6-8). The material response was measured through x-ray radiography and VISAR. The backlighter for face-on radiography was illuminated by 12 laser beams with a total peak power of approximately 2 TW. Two VISAR systems were used to provide assurance in the velocity data, with etalon lengths of 19.98 (VPF = 3.14) and 49.99 mm (VPF = 1.25). Radiation-hydrodynamic simulations with Ares [76] were performed to predict the effect of the applied pressure pulse to the iron ripples. The strength is inferred from such hydrodynamic simulations, assuming the calculated growth factor agrees with the measured values. The ripple growth factor is calculated based on certain strength models (SG, PTW, etc.) which also predict the yield strength of the material. The measured ripple growth data is then compared to simulations to determine which strength model is most accurate.

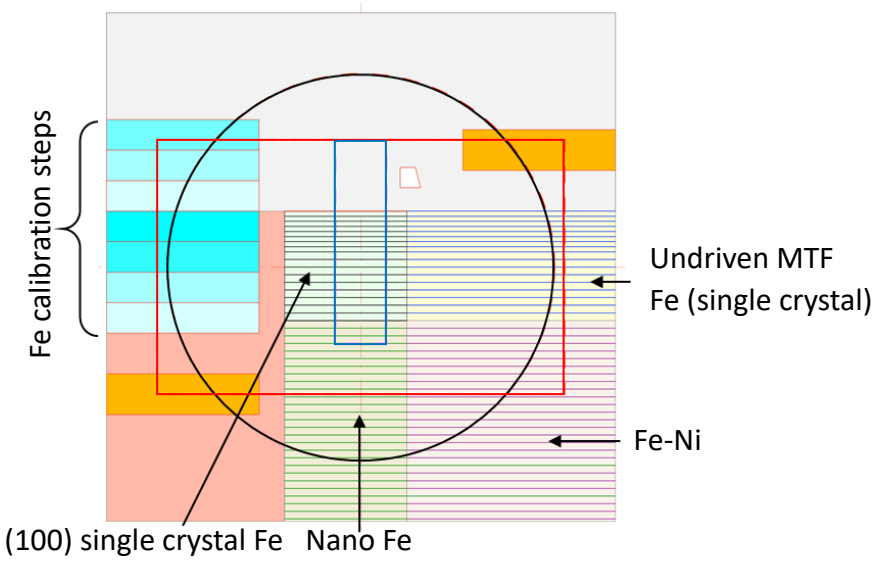

Figure 6-8. Iron target layout for hohlraum experiments with various ripple regions. Black circle, red rectangle, and blue rectangle represent driven area, radiography field of view, and VISAR field of view, respectively.

Single crystal iron discs (10 mm diameter, 1 mm thickness) were purchased from Accumet Materials Co and had a purity of 99.94+%. A few of these discs were further process with High-Pressure Torsion (HPT) to produce nanocrystalline grain structure. The HPT was conducted at Oregon State University with 20 turns at 2 GPa and produced an average grain size of ~100 nm. Iron-nickel was purchased from American Elements (24wt% Ni) and Goodfellow (35wt% Ni). Microstructure characterization was performed using Rigaku MiniFlex X-ray Diffraction (XRD) instrument, FEI Quanta 600 Scanning Electron Microscope (SEM) with EBSD (Electron Backscatter Diffraction), and Transmission Electron Microscopy (TEM).

6.5 Experimental Results

In the first NIF campaign, two shots were performed – July 2019 and February 2020. The first shot used only face-on x-ray radiography to measure ripple growth 60 ns after laser drive (Fig. 6-9a) which corresponded to the theoretical peak growth according to Fig. 6-9b. Lineouts of each region of the target provide the final ripple amplitude and when compared to the initial metrology measurements, the growth factor is calculated. Preliminary results show that the single crystal iron, nanocrystal iron, and iron-nickel alloy (24wt% Ni) had growth factors of 2.6, 2.2, and 2.2, respectively. The hydrodynamic simulations predict a strength of 15 GPa for a growth factor of 3.0 (Fig. 6-9c), so lower measured growth factors result in even higher strength. Additionally, since the growth factors were all so similar, it can be assumed that the strength is also similar for each microstructure.

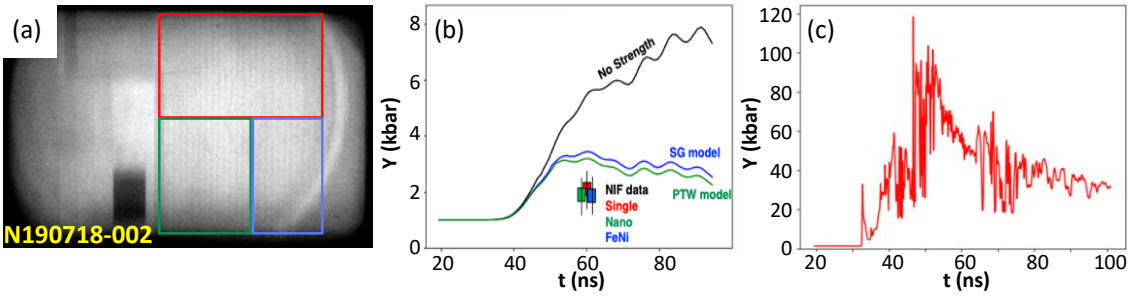

Figure 6-9. (a) Iron RT radiograph from shot N190718-002 where red, green, and blue regions correspond to single crystal Fe, nanocrystal Fe, and Fe-24Ni, (b) Predicted Fe growth factor vs. NIF data, and (c) inferred iron strength at 350 GPa with standard PTW model. Measured GF is lower than this model by ~2x.

The second shot used both VISAR and face-on x-ray radiography, 70 ns after the laser drive (Fig. 6-10a). Again, lineouts of each region provided the ripple growth information, this time with the addition of undriven ripple region to aid in analysis. The radiography data for this shot was partially obstructed by gold plasma filling in the hohlraum, so the growth factor is still being determined. VISAR data for this shot can be seen in Fig. 6-10b and confirms peak pressure reached during the experiment is ~350 GPa.

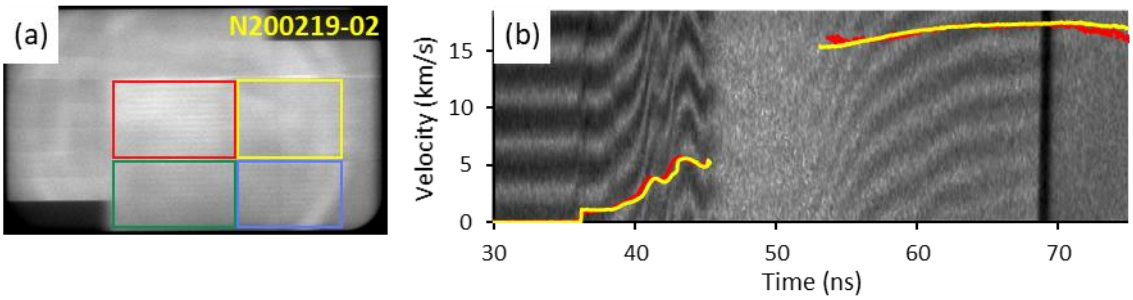

Figure 6-10. (a) Iron RT radiography from shot N200219-02 and (b) measured VISAR showing peak velocity of ~17.5 km/s which corresponds to ~350 GPa pressure.

The second NIF campaign has a 4-shot allocation, the first of which occurred in March 2021. In this experiment, single crystal iron, nanocrystal iron, and Fe-35Ni were used in a similar configuration as the previous experiments. Face-on radiography (Fig. 6-11) and VISAR were used to determine ripple growth 70 ns after laser start and pressure in the sample, similar to shot N200219. A higher energy backlighter was used in order to get higher quality data, but because of the use of a hohlraum, hold plasma again obscured the data. Further, more intensive, work is needed to de-noise the data and extract viable results.

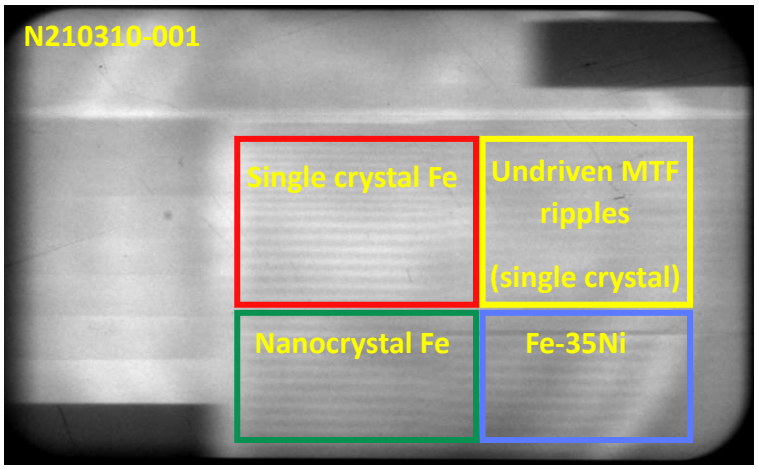

Figure 6-11. N210310 radiography. Gold plasma filling is also present, complicating the growth factor analysis.

The remaining 3 shots will be used to investigate strength dependence on orientation and composition in single crystal iron and iron-nickel alloys (10 – 35wt% Ni). These NIF shots will use the direct-drive design (Fig. 6-7c, d) described in Section 6.3 in the hope of getting unobscured data and the desired pressure and temperature. The first of said three shots occurred in May 2022. In this experiment, single crystal iron in (100) and (111) orientations and Fe-35Ni were used in a similar configuration as the previous experiments. Face-on radiography (Fig. 6-12a) and VISAR were used to determine ripple growth 55 ns after laser start and pressure in the sample. The direct-drive configuration caused the driven area to be elliptical rather than circular, so the FeNi driven region was too small to analyze. The remaining iron regions were analyzed using various growth factor calculation methods: the modulation transfer function (MTF) to adjust GF calculation by the backlighter diagnostic spatial resolution and step calibration to create a calibration curve

of amplitude in PSL (photostimulated luminescence – the intensity units of the raw radiography data) vs amplitude in microns. These two methods produced growth factor data as seen in Fig. 6-12b. It is important to note that these results are very preliminary – much more thorough analysis of the data as well as many more post-shot simulations need to be conducted. At first look, however, it seems like the data align with the three stronger constitutive models: ε-PTW, SGx2, and SGx5. Further work on this project will be ongoing. The remaining two shots of this series will be conducted in June 2022 and March 2023.

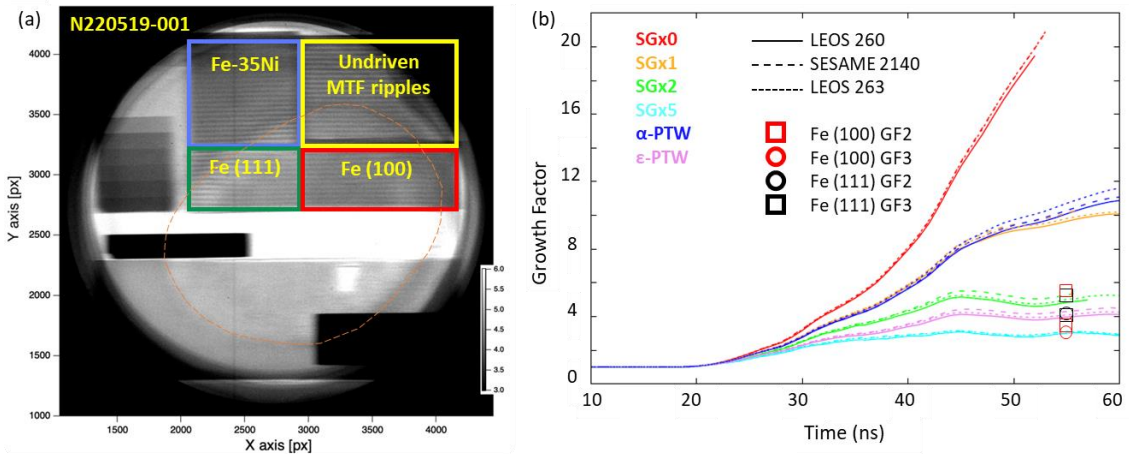

Figure 6-12. (a) N220519 radiography. Driven region is seen as elliptical feature outlined in orange dashed line. (b) Predicted Fe growth factor vs. NIF data. FeNi driven region was too small to extract growth factor. GF2 and GF3 represent growth factor calculation method based on MTF and step calibration, respectively. Data analysis courtesy of Yong-Jae Kim.

Overall, due to the lack of concrete GF data, it is still unclear how the microstructure of iron effects its high-pressure strength. The data so far is inconclusive, but a few theories are possible.

1. Samples with an initially smaller grain size will have a higher strength than the single crystal counterpart, following the traditional Hall-Petch behavior.
2. There is no strength difference between the different microstructures, similar to what was found in tantalum [189] at 130 GPa. In tantalum it was found that at these high pressures and strain rates, pressure and strain rate hardening dominate over the grain size effect.
3. In-situ diffraction experiments have reported a reduction in grain size, down to ~10 nm, during the shock-induced α-ϵ phase transformation in iron [51]. This reported grain size is much smaller than the initial nanostructure tested here (~100 nm) so it is possible that due to this phase change, the initial microstructure does not make a difference to the material strength.

Chapter 6, in part, is a reprint of material as it appears in: Righi, G., Lockard, T. E., Rudd, R. E., Meyers, M. A., Park, H.-S. Design of high-pressure iron Rayleigh-Taylor strength experiments for the National Ignition Facility. Journal of Applied Physics 131 145902 (2022). The dissertation author was the primary investigator and author of this paper.

Chapter 7: Omega EP Strength Work

7.1 Experimental Methods

Experiments using the Omega EP laser focused on the determination of iron strength at 100 GPa and various temperatures (1000 – 3000 K). Three of the four EP beams are used to drive the target and the fourth beam is used to illuminate a backlighter (Fig. 7-1a). The target schematic (Fig. 7-1b) is similar to direct drive experiments at the NIF and radiography is also be performed to measure RT ripple growth. Using the unique pulse shaping capability at Omega EP, rippled iron samples were shocked and consequently ramped to the desired pressure (Fig. 7-2a, b). The initial delivered shock raises the temperature and the remaining ramped pulse increases the temperature steadily (Fig.7-2c).

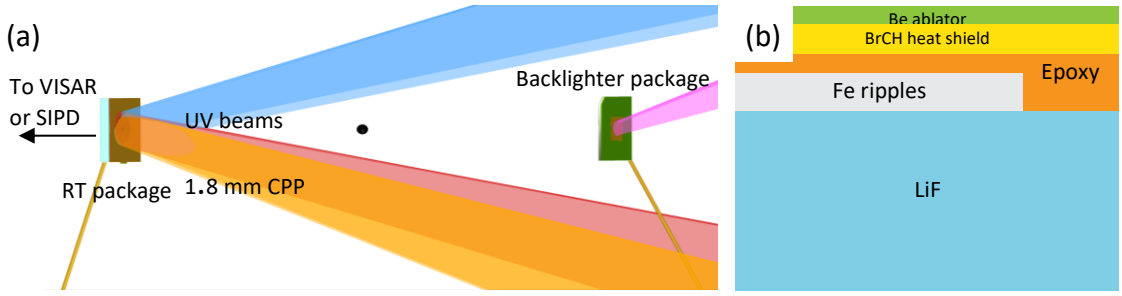

Figure 7-1. (a) VisRad model of experimental set up showing pointing of Omega EP beams on target and backlighter. (b) Target layout for shock/ramp experiments. Iron ripple layout will be similar to NIF design.

7.2 Preliminary Experimental Results

The measured ripple growth will be compared to 2D hydrodynamic simulations that predict the growth, depending on the chosen strength model (Fig. 7-2c). For different strength models (SG, PTW), the yield strength can differ by at least 30% during the ripple

growth for the two pulse shapes, a level these experiments should be able to measure. Yield strength calculations based on the Ping et al. EXAFS experiments show significant disagreement with other models and experiments, predicting strength ~5 times larger [160]. Recent MD simulations indicate that strength at 150 GPa undergo a decrease of 25% at higher temperatures, and also emphasize the effects of the microstructure generated at much lower pressures, due to the α–ε phase transition [190]. The experiments may well find even greater difference than predicted by existing models, an exciting result that would point to the importance of novel deformation mechanisms. By changing the pulse shape for each shot, we would be able to probe different temperature regimes in which deformation mechanisms can change. Herein, the low and high temperature laser drives are referenced as lowT and highT, respectively. These temperatures are approximately, as shown in Fig. 7-2c, 1,500 and 3,500 K. The corresponding growth factor predictions are, respectively, ~2.5 and 3.5 for the ε-PTW model. The strength predictions are 6 GPa for 1,500 K and 10 GPa for 3,500 K. During the shot day, due to changes in the shot sequence, RT measurements were only taken at the high temperature condition. Further proposals will focus on returning to the lower adiabat drive (as shown in Fig. 7-2a) to take RT measurements and complete this strength investigation.

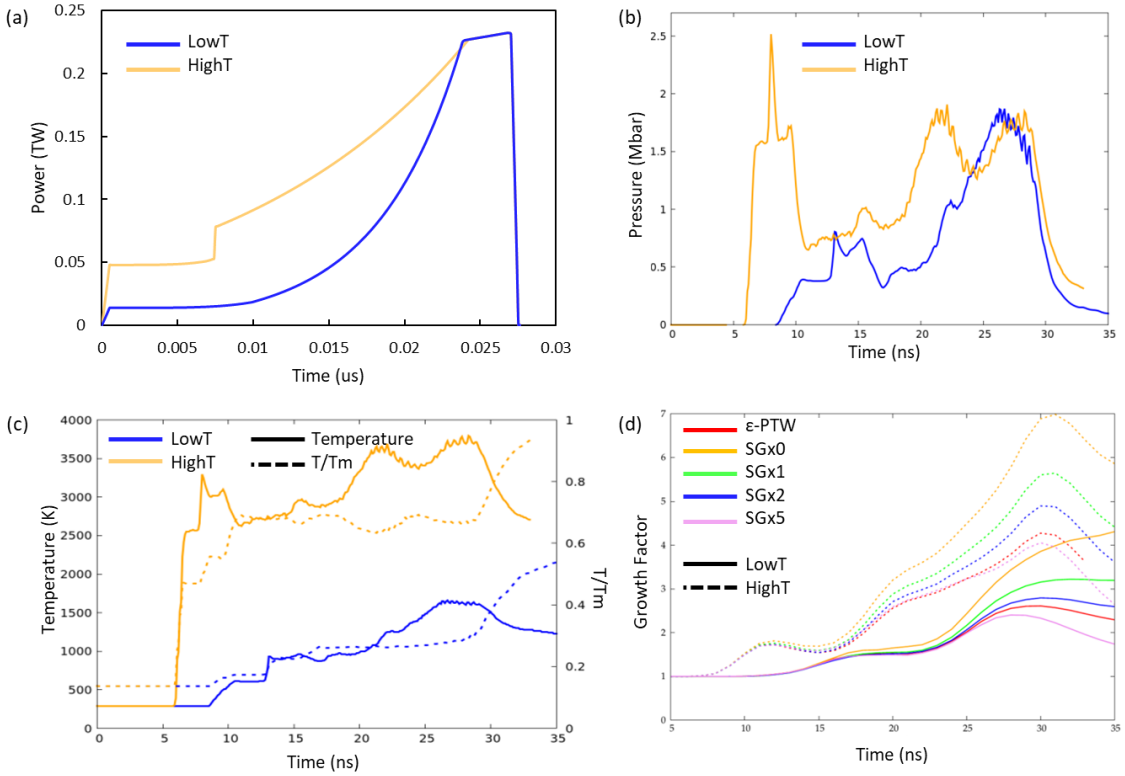

Figure 7-2. Hydrodynamic simulations of the OmegaEP experiments using Hydra: (a) pulse shape with different initial foot to control sample temperatures; (b) predicted pressure profile on iron sample; (c) predicted temperature and T/T_{melt} changes by different pulse shape (indicated by line style); (d) predicted growth factor for different amounts of strength (indicated by line color) for high and low temperature drives (indicated by line style).

The first shots of the day were used to confirm the laser drive using special drive targets (with thin aluminum (Al) coating instead of iron) and the VISAR diagnostic. The highT drive was stitched together fairly well, with minimal power spikes between the stitched pulses (Fig. 7-3a). The aluminum coating functioned as expected and provided velocity data at the Al-LiF interface. The peak particle velocity was ~5.5 km/s (Fig. 7-3b), which corresponds to a pressure of ~200 GPa. In reality, this is not solely on-Hugoniot

shock compression so simulations need to be used to determine accurate conditions achieved by ramp compression. Post-shot Hydra simulations calculate peak pressure of ~250 GPa and 4500 – 5000 K.

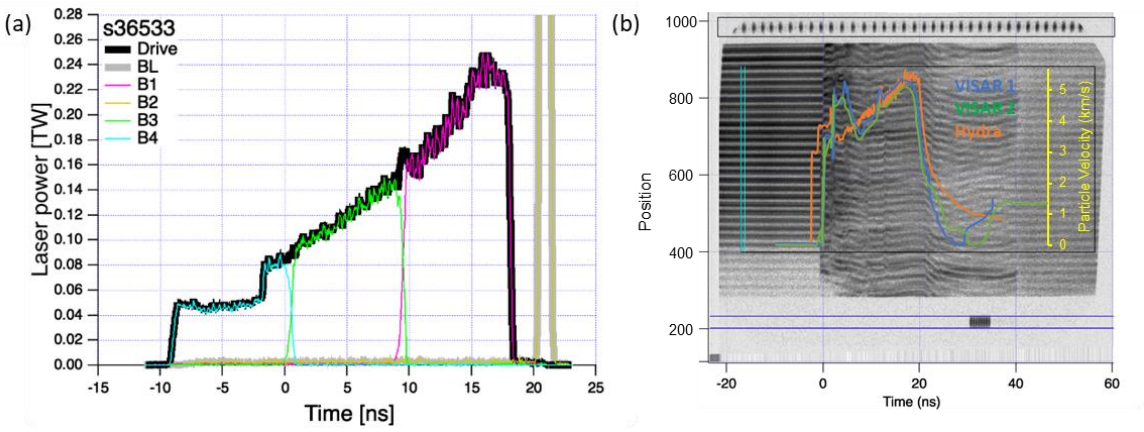

Figure 7-3. (a) Laser drive for s36533 where colored lines represent individual beams stitched together for the total drive pulse (black line). Backlighter fired at 20.3 ns which, due to beam delay, corresponds to delay time of 31 ns. (b) Measured free surface velocity from both VISAR systems compared to 1-D radiation-hydrodynamic simulations. Velocity behavior is similar between experiment and simulations.

The remaining shots were focused on RT measurements of driven iron foils (as seen in Fig. 7-1). Data was taken at 4 different delay times to best capture the evolution of ripple growth, between 25 and 33 ns. Data quality was overall excellent considering this was the first ironRT campaign to use a long pulse (1 ns) slit-backlighter configuration. This type of backlighter, as opposed to the more commonly used micro-flag, provided a more monochromatic x-ray source for imaging. This helped in improving ripple contrast for iron, since it is a low-Z element, but a certain level of spatial resolution was also lost. Fig. 7-4

shows the four images that were taken, which include driven rippled iron, undriven rippled iron as a reference, and various calibration features (steps and knife edge).

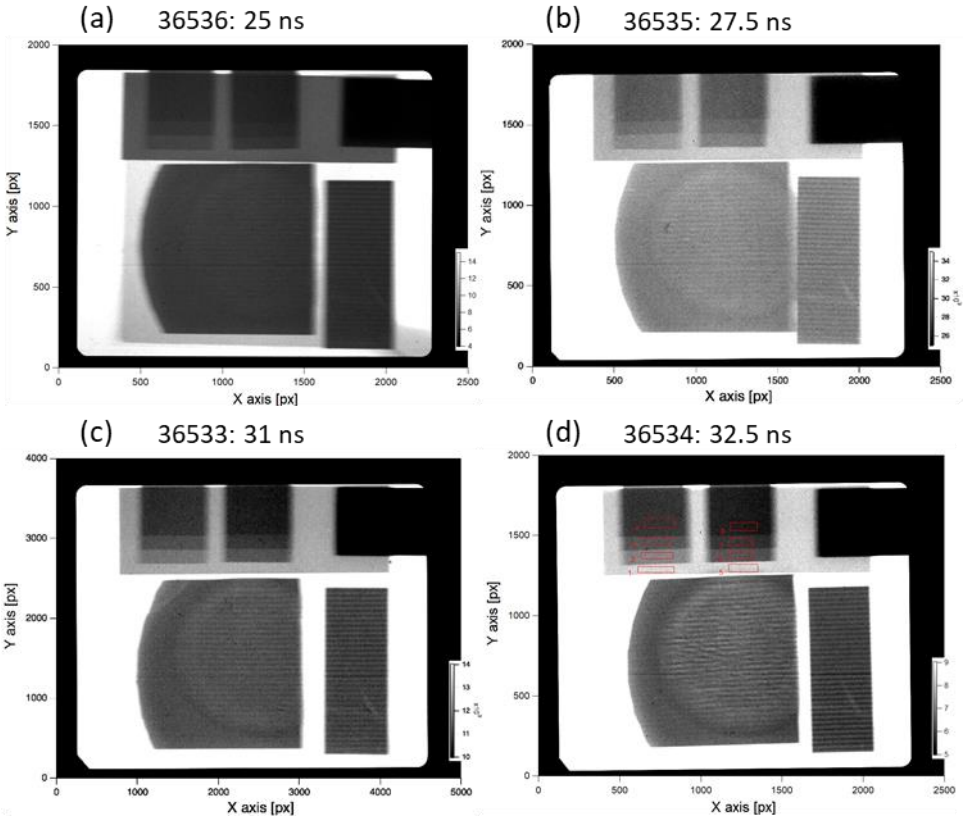

Figure 7-4. Experimental radiography data at different backlighter delay times.

There are various methods to calculate the growth factor of ripples: (i) driven vs. undriven, (ii) modulation transfer function (MTF), and (iii) step calibration. For method (i), the larger rippled iron portion is split into a driven area (1.8 mm diameter) and undriven regions. For this campaign, there was not enough area around the driven circle to calculate growth factor (GF) using this method. Method (ii) uses the gold knife edge (top right black rectangle in Fig. 7-4a-d) to adjust the GF calculation with the backlighter diagnostic spatial

resolution (described in Section 6.4). Due to the loss of spatial resolution from the slit-backlighter design, this method did not produce robust results. In method (iii), the iron steps (top of the target in Fig. 7-4a-d) are used to create a calibration curve of amplitude in PSL (photostimulated luminescence – the intensity units of the raw radiography data) vs amplitude in microns. This method produced robust results. Fig. 7-5 shows the measured data points compared to growth predictions for the ε-PTW strength model with different amounts of epoxy. The experiments were modeled this way due to how the target was built. Data is consistently higher than the curves, suggesting strength is weaker than is predicted by the PTW strength model (< 10 GPa). The differences between the experimental and simulated growth factors could be attributed to: (1) the high temperature is allowing for easier deformation and weaker material, (2) the iron is unintentionally melting, meaning the hydro simulations are not modeling this physics correctly, or (3) the constitutive model used in this case is not accurate and needs further development.

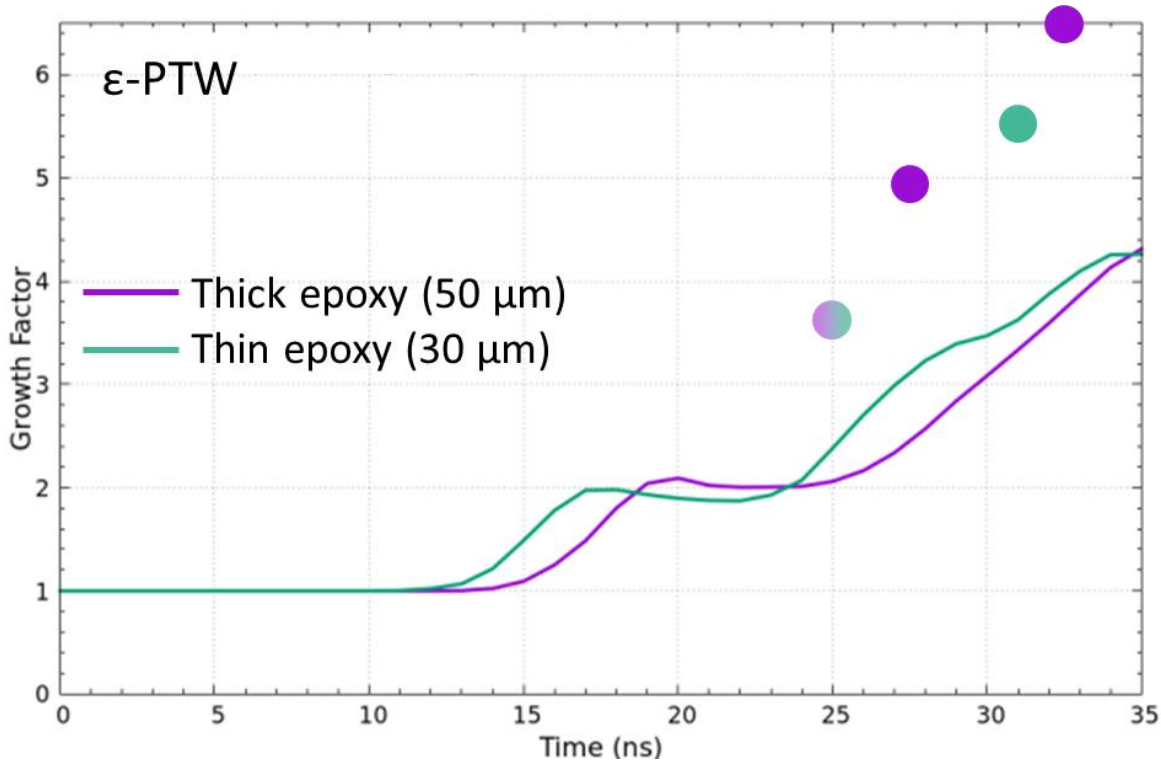

Figure 7-5. Measured (circles) and predicted growth according to ε-PTW model (lines) of iron ripples. Colors correspond to different amounts of epoxy. Growth is higher than expected meaning strength is lower than is calculated from the constitutive model.

Chapter 8: Summary and Conclusions

Iron is the basis for many structural materials such as steels and high entropy alloys. Earth's core is mostly pure iron but many other geophysical objects are also iron-based or made of an iron alloy. Thus, understanding the dynamic behavior of iron is a vital step in developing an understanding of the behavior of the many iron-based materials. Iron also undergoes high pressure phase transformations and the effect of such transformations is still unclear. Shock compression is a dynamic deformation process on the timescale of nanoseconds that is caused by the steepening of infinitesimally small shocks. These types of experiments can be carried out in a variety of methods, but laser-induced shock generally occurs at the highest strain rates and can achieve the highest pressures. There are various facilities that are able to perform these types of experiments, among which the NIF is the largest laser laboratory in the world. Laser shock can be used to induce plastic flow, amorphization, phase transitions, and even failure. Spallation is a failure dynamic failure process induced by the interactions of shock waves with a free surface. This type of failure behavior can be affected by microstructure, similar to material strength. However, in contrast to strength in conventional low strain-rate experiments, spall strength is generally higher in single crystal material. This behavior is due to failure being dominated by defects, like grain boundaries of which nanocrystalline material has plenty. The grain size effect on the strength of materials at ambient conditions can be described by the Hall-Petch relationship but at higher strain rates, other constitutive models are more accurate. For

example, the PTW model can be used to describe the flow stress for strain rates of 10^{-3} – 10^{12} s^{-1}. These constitutive relationships are used to simulate the growth of Rayleigh-Taylor (RT) instabilities for ultra-high-pressure experiments.

Quasistatic compression at strain rates of 10^{-4} s^{-1} and 10^{-1} s^{-1} were performed to determine the mechanical properties of iron at lower pressures. Under uniaxial compression the strength of iron clearly follows the Hall-Petch effect, with the yield strength increasing from 200 MPa to 1100 MPa with a grain size reduction to 100 nm.

Under laser shock compression, spall in iron was studied to determine grain size and strain rate effects. The Janus laser was used to drive thin iron samples to ~80 GPa pressure and 10^{6} s^{-1} – 10^{7} s^{-1} strain rates. The spall strength was calculated based on free surface velocity and was found to increase with grain size – opposite to the Hall-Petch effect. In all microstructure cases (single, poly, and nano), spall failure was dominated by voids. In single crystal iron, voids nucleate at intersections of shock-induced twins while grain boundaries are preferentially void nucleation sites in smaller grained samples. The subsequent void growth and coalescence causes ductile failure that was corroborated with MD simulations. The large dislocation density around voids (10^{15} m^{-2} from experiments, 10^{16} m^{-2} from MD, 10^{17} m^{-2} from analytical modeling) was also found to potentially increase the local temperature to near-melt.

A laser shock campaign at the DCS was used to study phase transitions during iron spall. Similar trend of spall strength and grain size was found at these slightly lower strain

rates. The α-ε phase transition was observed during shock compression as well as the reverse phase transition, ε-α, during release prior to complete spall. This reverse transition occurred within ~8 ns which was in close agreement with Molecular Dynamic simulation of the experiment. At peak pressure the grain size was found to be dramatically reduced, which is in agreement with previous work on the subject.

A large collaboration has been taking place for two NIF campaigns that study iron strength at Earth core conditions. A total of six shots were allocated, four of which have been performed and their analysis is also ongoing. The first shot discovered that ripple growth was lower than expected and therefore, strength should be higher than is predicted by analytical constitutive models. The subsequent two shots used the simultaneous VISAR platform that allowed for the exact determination of the pressure state – 360 GPa. Unfortunately, there is not a validated temperature diagnostic so simulations are used to determine temperature. Ares predicted a relatively low temperature of 2000 K which is much lower than the core state. The additional problem of gold plasma obscuring the radiography data led to the need for a direct-drive design for iron experiments. These novel direct-drive iron experiments were designed using two hydrodynamic codes – Hydra and Ares. These codes were used in conjunction to design the uniquely long NIF laser pulse and the layered target as well as predict the growth behavior at Earth core pressure and temperature. Each target layer and portion of the laser pulse was modified to determine a generalized effect on the final pressure/temperature state. For the experiments, the ideal

combination was determined to reach 350 GPa and 5000 K – making these shots the closest to the Earth's core that have been conducted. This new design will be tested in upcoming NIF shots that will complete the two Discovery Science campaigns. The data from the first test of the new design is still under analysis, with preliminary results showing agreement to some of the available constitutive models.

Lastly, a LaserNetUS campaign at Omega EP studied iron strength behavior at elevated pressure and temperature. Since Omega EP is a smaller laser facility, the conditions that can be achieved are lower than those achievable at the NIF, but the highly adjustable pulse shape allowed for unique experiments. Similar design techniques (as previously described) were used to perfect the pressure and temperature for further work on iron strength. By varying the strength of a shock at the front of the pulse shape, different temperatures can be achieved and so, temperature dependence on high-pressure strength can be investigated. A large factor of this campaign is also to validate constitutive models for high-pressure solid-state physics. During the experimental day, however, only the higher temperature case was probed. Preliminary results of these experiments find that iron is weaker than is predicted by the commonly used PTW model. This behavior is contradictory to the findings of the NIF iron RT, but still require further post-shot simulations.

References

[1] Iron, Wikipedia. (2021). https://en.wikipedia.org/w/index.php?title=Iron&oldid=1011923294 (accessed March 15, 2021).

[2] F. Oeters, M. Ottow, Iron, 5. Production of Pure and High-Purity Iron, in: Ullmann's Encyclopedia of Industrial Chemistry, Wiley-VCH Verlag GmbH & Co. KGaA, Weinheim, Germany, 2011: p. o14_o04. https://doi.org/10.1002/14356007.o14_o04.

[3] R.H. Tupkary, V.R. Tupkary, Modern Iron Making Handbook, (n.d.). https://app.knovel.com/hotlink/toc/id:kpMIMH0001/modern-iron-making-handbook/modern-iron-making-handbook.

[4] H. Mao, J. Shu, G. Shen, R.J. Hemley, B. Li, A.K. Singh, Elasticity and rheology of iron above 220 GPa and the nature of the Earth's inner core, Nature. 396 (1998) 741–743. https://doi.org/10.1038/25506.

[5] R. Abbaschian, L. Abbaschian, R. Reed-Hill, Physical Metallurgy Principles, 4th ed., Cengage Learning, Stamford, CT, 2009.

[6] J.R. Davis, A.S.M.I.H. Committee, Stainless Steels, ASM International, 1994. https://books.google.com/books?id=OrlG98AHdoAC.

[7] A.P.L. Blog, Role of steel in the aerospace industry, APL Apollo. (2020). https://aplapollo.com/role-of-steel-in-the-aerospace-industry/ (accessed April 28, 2021).

[8] NASA, Shuttle main engine test firing, 1981.

[9] I. Lehmann, P', Publications Du Bureau Central Séismologique International. 14 (1936) 87–115.

[10] B.A. Buffett, Earth's Core and the Geodynamo, Science. 288 (2000) 2007–2012. https://doi.org/10.1126/science.288.5473.2007.

[11] R. Jeanloz, The Nature of the Earth's Core, Annual Review of Earth and Planetary Sciences. 18 (1990) 357–86.

[12] C. Emiliani, Planet Earth: Cosmology, Geology, and the Evolution of Life and Environment, Cambridge University Press, Cambridge, UK, 1992.

[13] https://jpl.nasa.gov, Psyche, NASA Jet Propulsion Laboratory (JPL). (n.d.). https://www.jpl.nasa.gov/missions/psyche (accessed March 15, 2021).

[14] New candidate for "missing element" in Earth's core, BBC News. (2017). https://www.bbc.com/news/science-environment-38561076 (accessed March 15, 2021).

[15] D. Berry, Wrecking Worlds, Making Moons, n.d.

[16] W.J.M. Rankine, On the thermodynamic theory of waves of finite longitudinal disturbances, Philosophical Transactions of the Royal Society of London. 160 (1870) 277–288.

[17] H. Hugoniot, Mémoire sur la propagation des mouvements dans les corps et spécialement dans les gaz parfaits, Journal de l'Ecole Polytechnique. 57 (1889) 3–97.

[18] J. Colvin, J. Larsen, Extreme Physics: Properties and Behavior of Matter at Extreme Conditions, Cambridge University Press, Cambridge, UK, 2013.

[19] M.A. Meyers, Dynamic Behavior of Materials, John Wiley & Sons, 1994.

[20] P.O.K. Krehl, The classical Rankine-Hugoniot jump conditions, an important cornerstone of modern shock wave physics: ideal assumptions vs. reality, EPJ H. 40 (2015) 159–204. https://doi.org/10.1140/epjh/e2015-50010-4.

[21] H.-S. Park, B.A. Remington, R.C. Becker, J.V. Bernier, R.M. Cavallo, K.T. Lorenz, S.M. Pollaine, S.T. Prisbrey, R.E. Rudd, N.R. Barton, Strong stabilization of the Rayleigh–Taylor instability by material strength at megabar pressures, Physics of Plasmas. 17 (2010) 056314. https://doi.org/10.1063/1.3363170.

[22] B. Hopkinson, A Method of Measuring the Pressure Produced in the Detonation of High Explosives or by the Impact of Bullets, The Royal Society. 89 (1914).

[23] Laser Facilities, (n.d.). https://jlf.llnl.gov/laser-facilities (accessed March 17, 2021).

[24] Omega Laser Facility – Laboratory for Laser Energetics, (n.d.). https://www.lle.rochester.edu/index.php/omega-laser-facility-2/ (accessed March 17, 2021).

[25] NIF and Photon Science, (n.d.). https://lasers.llnl.gov/ (accessed March 17, 2021).

[26] Overview | Advanced Photon Source, (n.d.). https://www.aps.anl.gov/About/Overview (accessed March 25, 2021).

[27] The Dynamic Compression Sector | Washington State University, (n.d.). https://dcs-aps.wsu.edu/ (accessed March 25, 2021).

[28] MEC - Matter in Extreme Conditions, Linac Coherent Light Source. (2017). https://lcls.slac.stanford.edu/instruments/mec (accessed March 25, 2021).

[29] Linac Coherent Light Source, Linac Coherent Light Source. (n.d.). https://lcls.slac.stanford.edu/ (accessed March 25, 2021).

[30] L.M. Barker, R.E. Hollenbach, Laser interferometer for measuring high velocities of any reflecting surface, Journal of Applied Physics. 43 (1972) 4669–4675. https://doi.org/10.1063/1.1660986.

[31] P.M. Celliers, D.K. Bradley, G.W. Collins, D.G. Hicks, T.R. Boehly, W.J. Armstrong, Line-imaging velocimeter for shock diagnostics at the OMEGA laser facility, Review of Scientific Instruments. 75 (2004) 4916–4929. https://doi.org/10.1063/1.1807008.

[32] J. Kilkenny, H. Chen, X-ray back-lighting diagnostics, (2020).

[33] M. de Graef, M.E. McHenry, Structure of Materials: An introduction to crystallography, diffraction, and symmetry, 2nd ed., Cambridge University Press, Cambridge, UK, 2012.

[34] Z.M.M. Sternberger, Determining Strength of Materials Under Dynamic Loading Conditions Using Hydrodynamic Instabilities, California Institute of Technology, 2016.

[35] T.H. Judge, P.J. Buttkus, Ballistic and Spall Tests for Aircrew Body Armor, 1972.

[36] H.J. Melosh, Impact Ejection, Spallation, and the Origin of Meteorites, (1984) 27.

[37] NASA, Meteroroid Damage Assessment, Space Vehicle Design Criteria. (1970).

[38] T. Antoun, ed., Spall fracture, Springer, New York, 2003.

[39] M.A. Meyers, C. Taylor Aimone, Dynamic fracture (spalling) of metals, Progress in Materials Science. 28 (1983) 1–96. https://doi.org/10.1016/0079-6425(83)90003-8.

[40] G. Avramovic-Cingara, Ch.A.R. Saleh, M.K. Jain, D.S. Wilkinson, Void Nucleation and Growth in Dual-Phase Steel 600 during Uniaxial Tensile Testing, Metall and Mat Trans A. 40 (2009) 3117–3127. https://doi.org/10.1007/s11661-009-0030-z.

[41] Y. Fan, A. Kushima, S. Yip, B. Yildiz, Mechanism of Void Nucleation and Growth in bcc Fe: Atomistic Simulations at Experimental Time Scales, PHYSICAL REVIEW LETTERS. 106 (2011) 125501.

[42] B. Margolin, G. Karzov, V. Shvetsova, V. Kostylev, MODELLING FOR TRANSCRYSTALLINE AND INTERCRYSTALLINE FRACTURE BY VOID NUCLEATION AND GROWTH, Fatigue & Fracture of Engineering Materials & Structures. 21 (1998) 123–137. https://doi.org/10.1046/j.1460-2695.1998.00474.x.

[43] R.E. Rudd, Void growth in bcc metals simulated with molecular dynamics using the Finnis–Sinclair potential, Philosophical Magazine. 89 (2009) 3133–3161. https://doi.org/10.1080/14786430903222529.

[44] E.T. Seppala, J.F. Belak, R.E. Rudd, Effect of stress triaxiality on void growth in dynamic fracture of metals: A molecular dynamics study, Physical Review B. 69 (2004) 134101.

[45] D. Bancroft, E.L. Peterson, S. Minshall, Polymorphism of Iron at High Pressure, Journal of Applied Physics. 27 (1956) 291–298. https://doi.org/10.1063/1.1722359.

[46] Zurek, Anna K., M.A. Meyers, Microstructural aspects of dynamic failure, in: High-Pressure Shock Compression of Solids II, Springer, New York, NY, 1996: pp. 25–70.

[47] J.O. Erkman, Smooth Spalls and the Polymorphism of Iron, Journal of Applied Physics. 32 (1961) 939–944. https://doi.org/10.1063/1.1736137.

[48] L.M. Barker, R.E. Hollenbach, Shock wave study of the α ⇄ ε phase transition in iron, Journal of Applied Physics. 45 (1974) 4872–4887. https://doi.org/10.1063/1.1663148.

[49] T. de Rességuier, M. Hallouin, Effects of the α − ε phase transition on wave propagation and spallation in laser shock-loaded iron, Phys. Rev. B. 77 (2008) 174107. https://doi.org/10.1103/PhysRevB.77.174107.

[50] N. Gunkelmann, E.M. Bringa, H.M. Urbassek, Influence of phase transition on shock-induced spallation in nanocrystalline iron, Journal of Applied Physics. 118 (2015) 185902. https://doi.org/10.1063/1.4935452.

[51] J.A. Hawreliak, D.H. Kalantar, J.S. Stölken, B.A. Remington, H.E. Lorenzana, J.S. Wark, High-pressure nanocrystalline structure of a shock-compressed single crystal of iron, Phys. Rev. B. 78 (2008) 220101. https://doi.org/10.1103/PhysRevB.78.220101.

[52] H. Shu, X. Huang, H. Pan, J. Ye, F. Zhang, G. Jia, Z. Fang, Y. Tu, Z. Xie, S. Fu, Plastic behavior of steel and iron in high strain rate regime, Int J Fract. 206 (2017) 81–93. https://doi.org/10.1007/s10704-017-0202-6.

[53] J. Wang, F. Coppari, R.F. Smith, J.H. Eggert, A.E. Lazicki, D.E. Fratanduono, J.R. Rygg, T.R. Boehly, G.W. Collins, T.S. Duffy, X-ray diffraction of molybdenum under shock compression to 450 GPa, Phys. Rev. B. 92 (2015) 174114. https://doi.org/10.1103/PhysRevB.92.174114.

[54] S.I. Ashitkov, P.S. Komarov, M.B. Agranat, G.I. Kanel, V.E. Fortov, Achievement of ultimate values of the bulk and shear strengths of iron irradiated by femtosecond laser pulses, Jetp Lett. 98 (2013) 384–388. https://doi.org/10.1134/S0021364013200022.

[55] W.H. Bragg, W.L. Bragg, The reflection of X-rays by crystals, Proc. R. Soc. Lond. A. 88 (1913) 428–438. https://doi.org/10.1098/rspa.1913.0040.

[56] P. Scherrer, Nachr Ges wiss goettingen, Math. Phys. 2 (1918) 98–100.

[57] B.E. Warren, B.L. Averbach, The Effect of Cold-Work Distortion on X-Ray Patterns, Journal of Applied Physics. 21 (1950) 595–599. https://doi.org/10.1063/1.1699713.

[58] R.B. Von Dreele, S.M. Clarke, J.P.S. Walsh, `Pink'-beam X-ray powder diffraction profile and its use in Rietveld refinement, J Appl Crystallogr. 54 (2021) 3–6. https://doi.org/10.1107/S1600576720014624.

[59] M. Ashby, H. Shercliff, D. Cebon, Materials engineering, science, processing, and design, 2nd ed., Elsevier/Butterworth-Heinemann, 2010.

[60] D. Hull, D.J. Bacon, Introduction to dislocations, 5th ed., Elsevier/Butterworth-Heinemann, Amsterdam, 2011.

[61] E.O. Hall, The Deformation and Ageing of Mild Steel: III Discussion of Results, Proc. Phys. Soc. B. 64 (1951) 747–753. https://doi.org/10.1088/0370-1301/64/9/303.

[62] Z.C. Cordero, B.E. Knight, C.A. Schuh, Six decades of the Hall–Petch effect – a survey of grain-size strengthening studies on pure metals, International Materials Reviews. 61 (2016) 495–512. https://doi.org/10.1080/09506608.2016.1191808.

[63] E. Voce, The relationship between stress and strain for homogeneous deformation, J. Inst. Met. 74 (1948) 537.

[64] F.J. Zerilli, R.W. Armstrong, Dislocation-mechanics-based constitutive relations for material dynamics calculations, Journal of Applied Physics. 61 (1987) 1816–1825. https://doi.org/10.1063/1.338024.

[65] G.R. Johnson, W.H. Cook, A constitutive model and data for metals subjected to large strains, high strain rates and high temperatures, Proceedings of the 7th International Symposium on Ballistics. (1983) 541–547.

[66] D.J. Steinberg, S.G. Cochran, M.W. Guinan, A constitutive model for metals applicable at high-strain rate, Journal of Applied Physics. 51 (1980) 1498–1504. https://doi.org/10.1063/1.327799.

[67] D.J. Steinberg, C.M. Lund, A constitutive model for strain rates from 10^{-4} to 10^{6} s^{-1}, Journal of Applied Physics. 65 (1989) 1528.

[68] D.L. Preston, D.L. Tonks, D.C. Wallace, Model of plastic deformation for extreme loading conditions, Journal of Applied Physics. 93 (2003) 211–220. https://doi.org/10.1063/1.1524706.

[69] D.J. Steinberg, Equation of State and Strength Properties of Selected Materials, Lawrence Livermore National Laboratory, Livermore, CA, 1996.

[70] R. Kishore, T.K. Sinha, Analysis of the stress-strain curves of a modified 9Cr-1Mo steel by the voce equation, MMTA. 27 (1996) 3340–3343. https://doi.org/10.1007/BF02663885.

[71] J.L. Belof, R.M. Cavallo, R.T. Olson, R.S. King, G.T. Gray, Rayleigh-Taylor strength experiments of the pressure-induced a->e->a', AIP Conf. Proc. 1426, 1521 (2012).

[72] L.J.W.S. Rayleigh, Investigation of the Character of the Equilibrium of an Incoming pressibly Heavy Fluid of Variable Density, Proceedings of the London Mathematical Society. 14 (1883) 170–177.

[73] G.I. Taylor, The instability of liquid surfaces when accelerated in a direction perpendicular to their planes. I, Proc. R. Soc. Lond. A. 201 (1950) 192–196. https://doi.org/10.1098/rspa.1950.0052.

[74] C.M. Huntington, J.L. Belof, K.J.M. Blobaum, R.M. Cavallo, N.B. Kostinski, B.R. Maddox, H.-S. Park, C. Plechaty, S.T. Prisbrey, R. Rudd, D.W. Swift, R.J. Wallace, S.V. Weber, C. Wehrenberg, M.J. Wilson, B.A. Remington, Investigating iron material strength up to 1 Mbar using Rayleigh-Taylor growth measurements, in: Tampa Bay, Florida, USA, 2017: p. 110007. https://doi.org/10.1063/1.4971670.

[75] Lawrence Livermore National Lab., CA (United States), Inertial Confinement Fusion quarterly report, April--June 1995. Volume 5, No. 3, 1995. https://doi.org/10.2172/187252.

[76] G. Bazan, ASCI code calculations of supernova hydrodynamic instabilities, Livermore, CA, 1998.

[77] E.N. Hahn, T.C. Germann, R.J. Ravelo, J.E. Hammerberg, M.A. Meyers, Non-equilibrium molecular dynamics simulations of spall in single crystal tantalum, in: Tampa Bay, Florida, USA, 2017: p. 070006. https://doi.org/10.1063/1.4971594.

[78] E.N. Hahn, T.C. Germann, R. Ravelo, J.E. Hammerberg, M.A. Meyers, On the ultimate tensile strength of tantalum, Acta Materialia. 126 (2017) 313–328. https://doi.org/10.1016/j.actamat.2016.12.033.

[79] B.L. Holian, Plasticity Induced by Shock Waves in Nonequilibrium Molecular-Dynamics Simulations, Science. 280 (1998) 2085–2088. https://doi.org/10.1126/science.280.5372.2085.

[80] P. Hirel, Atomsk: A tool for manipulating and converting atomic data files, Computer Physics Communications. 197 (2015) 212–219. https://doi.org/10.1016/j.cpc.2015.07.012.

[81] N. Amadou, T. de Resseguier, A. Dragon, E. Brambrink, Coupling between plasticity and phase transition in shock- and ramp-compressed single-crystal iron, Phys. Rev. B. 98 (2018) 024104. https://doi.org/10.1103/PhysRevB.98.024104.

[82] N. Gunkelmann, E.M. Bringa, D.R. Tramontina, C.J. Ruestes, M.J. Suggit, A. Higginbotham, J.S. Wark, H.M. Urbassek, Shock waves in polycrystalline iron: Plasticity and phase transitions, Phys. Rev. B. 89 (2014) 140102. https://doi.org/10.1103/PhysRevB.89.140102.

[83] N. Amadou, T.D. Resseguier, A. Dragon, E. Brambrink, Effects of orientation, lattice defects and temperature on plasticity and phase transition in ramp-compressed single crystal iron, Computational Materials Science. 172 (2020) 109318. https://doi.org/10.1016/j.commatsci.2019.109318.

[84] N. Gunkelmann, D.R. Tramontina, E.M. Bringa, H.M. Urbassek, Morphological changes in polycrystalline Fe after compression and release, Journal of Applied Physics. 117 (2015) 085901. https://doi.org/10.1063/1.4913622.

[85] N. Gunkelmann, Interplay of plasticity and phase transformation in shock wave propagation in nanocrystalline iron, New J. Phys. (2014) 13.

[86] H.-T. Luu, R.G.A. Veiga, N. Gunkelmann, Atomistic Study of the Role of Defects on $\alpha \rightarrow \epsilon$ Phase Transformations in Iron under Hydrostatic Compression, Metals. 9 (2019) 1040. https://doi.org/10.3390/met9101040.

[87] N. Gunkelmann, E.M. Bringa, K. Kang, G.J. Ackland, C.J. Ruestes, H.M. Urbassek, Polycrystalline iron under compression: Plasticity and phase transitions, Phys. Rev. B. 86 (2012) 144111. https://doi.org/10.1103/PhysRevB.86.144111.

[88] S. Plimpton, Fast Parallel Algorithms for Short- Range Molecular Dynamics, (n.d.) 44.

[89] A. Stukowski, Visualization and analysis of atomistic simulation data with OVITO–the Open Visualization Tool, Modelling Simul. Mater. Sci. Eng. 18 (2010) 015012. https://doi.org/10.1088/0965-0393/18/1/015012.

[90] A. Stukowski, Structure identification methods for atomistic simulations of crystalline materials, Modelling Simul. Mater. Sci. Eng. 20 (2012) 045021. https://doi.org/10.1088/0965-0393/20/4/045021.

[91] P.M. Larsen, S. Schmidt, J. Schiøtz, Robust structural identification via polyhedral template matching, Modelling Simul. Mater. Sci. Eng. 24 (2016) 055007. https://doi.org/10.1088/0965-0393/24/5/055007.

[92] A. Stukowski, Computational Analysis Methods in Atomistic Modeling of Crystals, JOM. 66 (2014) 399–407. https://doi.org/10.1007/s11837-013-0827-5.

[93] A. Stukowski, K. Albe, Extracting dislocations and non-dislocation crystal defects from atomistic simulation data, Modelling Simul. Mater. Sci. Eng. 18 (2010) 085001. https://doi.org/10.1088/0965-0393/18/8/085001.

[94] D. Curran, Dynamic failure of solids, Physics Reports. 147 (1987) 253–388. https://doi.org/10.1016/0370-1573(87)90049-4.

[95] A.E. Mayer, Dynamic shear and tensile strength of iron: Continual and atomistic simulation, Mech. Solids. 49 (2014) 649–656. https://doi.org/10.3103/S0025654414060065.

[96] S.I. Ashitkov, V.V. Zhakhovsky, N.A. Inogamov, P.S. Komarov, M.B. Agranat, G.I. Kanel, The behavior of iron under ultrafast shock loading driven by a femtosecond laser, in: Tampa Bay, Florida, USA, 2017: p. 100035. https://doi.org/10.1063/1.4971660.

[97] D.E. Grady, The spall strength of condensed matter, Journal of the Mechanics and Physics of Solids. 36 (1988) 353–384. https://doi.org/10.1016/0022-5096(88)90015-4.

[98] T.P. Remington, E.N. Hahn, S. Zhao, R. Flanagan, J.C.E. Mertens, S. Sabbaghianrad, T.G. Langdon, C.E. Wehrenberg, B.R. Maddox, D.C. Swift, B.A. Remington, N. Chawla, M.A. Meyers, Spall strength dependence on grain size and strain rate in tantalum, Acta Materialia. 158 (2018) 313–329. https://doi.org/10.1016/j.actamat.2018.07.048.

[99] H. Jarmakani, B. Maddox, C.T. Wei, D. Kalantar, M.A. Meyers, Laser shock-induced spalling and fragmentation in vanadium, Acta Materialia. 58 (2010) 4604–4628. https://doi.org/10.1016/j.actamat.2010.04.027.

[100] E.B. Zaretsky, G.I. Kanel, Yield stress, polymorphic transformation, and spall fracture of shock-loaded iron in various structural states and at various temperatures, Journal of Applied Physics. 117 (2015) 195901. https://doi.org/10.1063/1.4921356.

[101] J. Wang, R.F. Smith, J.H. Eggert, D.G. Braun, T.R. Boehly, J. Reed Patterson, P.M. Celliers, R. Jeanloz, G.W. Collins, T.S. Duffy, Ramp compression of iron to 273 GPa, Journal of Applied Physics. 114 (2013) 023513. https://doi.org/10.1063/1.4813091.

[102] S.V. Razorenov, G.I. Kanel, V.E. Fortov, Iron at high negative pressures, Jetp Lett. 80 (2004) 348–350. https://doi.org/10.1134/1.1825120.

[103] G.V. Garkushin, N.S. Naumova, S.A. Atroshenko, S.V. Razorenov, Influence of the reversible α–ε phase transition and preliminary shock compression on the spall strength of armco iron, Tech. Phys. 61 (2016) 84–90. https://doi.org/10.1134/S1063784216010102.

[104] W. Pantleon, Resolving the geometrically necessary dislocation content by conventional electron backscattering diffraction, Scripta Materialia. 58 (2008) 994–997. https://doi.org/10.1016/j.scriptamat.2008.01.050.

[105] W. Cai, W.D. Nix, Materials Research Society, Imperfections in crystalline solids, 2016.

[106] C.H. Lu, B.A. Remington, B.R. Maddox, B. Kad, H.S. Park, S.T. Prisbrey, M.A. Meyers, Laser compression of monocrystalline tantalum, Acta Materialia. 60 (2012) 6601–6620. https://doi.org/10.1016/j.actamat.2012.08.026.

[107] C.H. Lu, B.A. Remington, B.R. Maddox, B. Kad, H.S. Park, M. Kawasaki, T.G. Langdon, M.A. Meyers, Laser compression of nanocrystalline tantalum, Acta Materialia. 61 (2013) 7767–7780. https://doi.org/10.1016/j.actamat.2013.09.016.

[108] E.N. Hahn, S.J. Fensin, T.C. Germann, The role of grain boundary orientation on void nucleation in tantalum, in: St. Louis, MO, USA, 2018: p. 050008. https://doi.org/10.1063/1.5044791.

[109] M.F. Ashby, The deformation of plastically non-homogeneous materials, The Philosophical Magazine: A Journal of Theoretical Experimental and Applied Physics. 21 (1970) 399–424. https://doi.org/10.1080/14786437008238426.

[110] M.F. Ashby, L. Johnson, On the generation of dislocations at misfitting particles in a ductile matrix, Philosophical Magazine. 20 (1969) 1009–1022. https://doi.org/10.1080/14786436908228069.

[111] M.F. Ashby, S.H. Gelles, L.E. Tanner, The stress at which dislocations are generated at a particle-matrix interface, Philosophical Magazine. 19 (1969) 757–771. https://doi.org/10.1080/14786436908216332.

[112] V.A. Lubarda, M.S. Schneider, D.H. Kalantar, B.A. Remington, M.A. Meyers, Void growth by dislocation emission, Acta Materialia. 52 (2004) 1397–1408. https://doi.org/10.1016/j.actamat.2003.11.022.

[113] T.P. Remington, C.J. Ruestes, E.M. Bringa, B.A. Remington, C.H. Lu, B. Kad, M.A. Meyers, Plastic deformation in nanoindentation of tantalum: A new mechanism for prismatic loop formation, Acta Materialia. 78 (2014) 378–393. https://doi.org/10.1016/j.actamat.2014.06.058.

[114] Y. Tang, E.M. Bringa, B.A. Remington, M.A. Meyers, Growth and collapse of nanovoids in tantalum monocrystals, Acta Materialia. 59 (2011) 1354–1372. https://doi.org/10.1016/j.actamat.2010.11.001.

[115] C.J. Ruestes, E.M. Bringa, A. Stukowski, J.F. Rodríguez Nieva, Y. Tang, M.A. Meyers, Plastic deformation of a porous bcc metal containing nanometer sized voids, Computational Materials Science. 88 (2014) 92–102. https://doi.org/10.1016/j.commatsci.2014.02.047.

[116] R.E. Rudd, E.T. Seppälä, L.M. Dupuy, J. Belak, Void coalescence processes quantified through atomistic and multiscale simulation, J Computer-Aided Mater Des. 14 (2007) 425–434. https://doi.org/10.1007/s10820-007-9054-0.

[117] N. Urabe, J. Weertman, Dislocation mobility in potassium and iron single crystals, Materials Science and Engineering. 18 (1975) 41–49.

[118] Y.B. Zel’dovich, Y.P. Raizer, Physics of Shock Waves and High-Temperature Hydrodynamic Phenomena, Courier Corporation, 2002.

[119] E. Orowan, Problems of plastic gliding, Proc. Phys. Soc. 52 (1940) 8–22. https://doi.org/10.1088/0959-5309/52/1/303.

[120] H. Quinney, G.I. Taylor, The emission of the latent energy due to previous cold working when a metal is heated, Proc. R. Soc. Lond. A. 163 (1937) 157–181. https://doi.org/10.1098/rspa.1937.0217.

[121] Z. Li, S. Zhao, B. Wang, S. Cui, R. Chen, R.Z. Valiev, M.A. Meyers, The effects of ultra-fine-grained structure and cryogenic temperature on adiabatic shear localization in titanium, Acta Materialia. 181 (2019) 408–422. https://doi.org/10.1016/j.actamat.2019.09.011.

[122] S. Nemat-Nasser, J.B. Isaacs, M. Liu, Microstructure of High-Strain-Rate Deformed Tantalum, Acta Materialia. 46 (1998) 1307–1325.

[123] K.M. Davoudi, J.J. Vlassak, Dislocation evolution during plastic deformation: Equations vs. discrete dislocation dynamics study, Journal of Applied Physics. 123 (2018) 085302. https://doi.org/10.1063/1.5013213.

[124] H. Mecking, U.F. Kocks, Kinetics of flow and strain-hardening, Acta Metallurgica. 29 (1981) 1865–1875. https://doi.org/10.1016/0001-6160(81)90112-7.

[125] D.C. Wallace, Nature of the process of overdriven shocks in metals, Phys. Rev. B. 24 (1981) 5607–5615. https://doi.org/10.1103/PhysRevB.24.5607.

[126] X.Y. Wu, K.T. Ramesh, T.W. Wright, The effects of thermal softening and heat conduction on the dynamic growth of voids, International Journal of Solids and Structures. 40 (2003) 4461–4478. https://doi.org/10.1016/S0020-7683(03)00214-2.

[127] G. Righi, C.J. Ruestes, C.V. Stan, S.J. Ali, R.E. Rudd, M. Kawasaki, H.-S. Park, M.A. Meyers, Towards the ultimate strength of iron: spalling through laser shock, Acta Materialia. 215 (2021) 117072. https://doi.org/10.1016/j.actamat.2021.117072.

[128] C. Prescher, V.B. Prakapenka, DIOPTAS: a program for reduction of two-dimensional X-ray diffraction data and data exploration, High Pressure Research. 35 (2015) 223–230. https://doi.org/10.1080/08957959.2015.1059835.

[129] J.C. Boettger, D.C. Wallace, Metastability and dynamics of the shock-induced phase transition in iron, Phys. Rev. B. 55 (1997) 2840–2849. https://doi.org/10.1103/PhysRevB.55.2840.

[130] K. Kadau, T.C. Germann, P.S. Lomdahl, B.L. Holian, Atomistic simulations of shock-induced transformations and their orientation dependence in bcc Fe single crystals, Phys. Rev. B. 72 (2005) 064120. https://doi.org/10.1103/PhysRevB.72.064120.

[131] B.J. Jensen, G.T. Gray, R.S. Hixson, Direct measurements of the α-ϵ transition stress and kinetics for shocked iron, Journal of Applied Physics. 105 (2009) 103502. https://doi.org/10.1063/1.3110188.

[132] S. Merkel, A. Lincot, S. Petitgirard, Microstructural effects and mechanism of bcc-hcp-bcc transformations in polycrystalline iron, Phys. Rev. B. 102 (2020) 104103. https://doi.org/10.1103/PhysRevB.102.104103.

[133] A. Dewaele, C. Denoual, S. Anzellini, F. Occelli, M. Mezouar, P. Cordier, S. Merkel, M. Véron, E. Rausch, Mechanism of the α − ε phase transformation in iron, Phys. Rev. B. 91 (2015) 174105. https://doi.org/10.1103/PhysRevB.91.174105.

[134] H. Hwang, E. Galtier, H. Cynn, I. Eom, S.H. Chun, Y. Bang, G.C. Hwang, J. Choi, T. Kim, M. Kong, S. Kwon, K. Kang, H.J. Lee, C. Park, J.I. Lee, Y. Lee, W. Yang, S.-H. Shim, T. Vogt, S. Kim, J. Park, S. Kim, D. Nam, J.H. Lee, H. Hyun, M. Kim, T.-Y. Koo, C.-C. Kao, T. Sekine, Y. Lee, Subnanosecond phase transition dynamics in laser-shocked iron, Sci. Adv. 6 (2020) eaaz5132. https://doi.org/10.1126/sciadv.aaz5132.

[135] H.M. Rietveld, A profile refinement method for nuclear and magnetic structures, J Appl Crystallogr. 2 (1969) 65–71. https://doi.org/10.1107/S0021889869006558.

[136] B.H. Toby, R.B. Von Dreele, GSAS-II: the genesis of a modern open-source all purpose crystallography software package, J Appl Crystallogr. 46 (2013) 544–549. https://doi.org/10.1107/S0021889813003531.

[137] W. Johnson, R. Mehl, Reaction kinetics in processes of nucleation and growth, Trans. Metal. Soc. 135 (1939) 416–442.

[138] M. Avrami, Kinetics of Phase Change. I General Theory, The Journal of Chemical Physics. 7 (1939) 1103–1112. https://doi.org/10.1063/1.1750380.

[139] A.N. Kolmogorov, On the statistical theory of the crystallization of metals, Bull. Acad. Sci. USSR, Math. Ser. 1 (1937) 355–359.

[140] M.G. Gorman, D. McGonegle, S.J. Tracy, S.M. Clarke, C.A. Bolme, A.E. Gleason, S.J. Ali, S. Hok, C.W. Greeff, P.G. Heighway, K. Hulpach, B. Glam, E. Galtier, H.J. Lee, J.S. Wark, J.H. Eggert, J.K. Wicks, R.F. Smith, Recovery of a high-pressure phase formed under laser-driven compression, Phys. Rev. B. 102 (2020) 024101. https://doi.org/10.1103/PhysRevB.102.024101.

[141] A.E. Gleason, C.A. Bolme, E. Galtier, H.J. Lee, E. Granados, D.H. Dolan, C.T. Seagle, T. Ao, S. Ali, A. Lazicki, D. Swift, P. Celliers, W.L. Mao, Compression Freezing Kinetics of Water to Ice VII, Phys. Rev. Lett. 119 (2017) 025701. https://doi.org/10.1103/PhysRevLett.119.025701.

[142] M. Avrami, Kinetics of Phase Change. II Transformation-Time Relations for Random Distribution of Nuclei, The Journal of Chemical Physics. 8 (1940) 212–224. https://doi.org/10.1063/1.1750631.

[143] D.H. Kalantar, J.F. Belak, G.W. Collins, J.D. Colvin, H.M. Davies, J.H. Eggert, T.C. Germann, J. Hawreliak, B.L. Holian, K. Kadau, P.S. Lomdahl, H.E. Lorenzana, M.A. Meyers, K. Rosolankova, M.S. Schneider, J. Sheppard, J.S. Stölken, J.S. Wark, Direct Observation of the α − ε Transition in Shock-Compressed Iron via Nanosecond X-Ray Diffraction, Phys. Rev. Lett. 95 (2005) 075502. https://doi.org/10.1103/PhysRevLett.95.075502.

[144] A.H. Cottrell, Commentary. A brief view of work hardening, in: F.R.N. Nabarro, M.S. Duesbery (Eds.), Elsevier, 2002: pp. vii–xvii. https://doi.org/10.1016/S1572-4859(02)80002-X.

[145] H.-S. Park, K.T. Lorenz, R.M. Cavallo, S.M. Pollaine, S.T. Prisbrey, R.E. Rudd, R.C. Becker, J.V. Bernier, B.A. Remington, Viscous Rayleigh-Taylor Instability Experiments at High Pressure and Strain Rate, Phys. Rev. Lett. 104 (2010) 135504. https://doi.org/10.1103/PhysRevLett.104.135504.

[146] H.-S. Park, N. Barton, J.L. Belof, K.J.M. Blobaum, R.M. Cavallo, A.J. Comley, B. Maddox, M.J. May, S.M. Pollaine, S.T. Prisbrey, B. Remington, R.E. Rudd, D.W. Swift, R.J. Wallace, M.J. Wilson, A. Nikroo, E. Giraldez, Experimental

results of tantalum material strength at high pressure and high strain rate, AIP Conference Proceedings. 1426 (2012) 1371–1374. https://doi.org/10.1063/1.3686536.

[147] S. Fujioka, A. Sunahara, K. Nishihara, N. Ohnishi, T. Johzaki, H. Shiraga, K. Shigemori, M. Nakai, T. Ikegawa, M. Murakami, K. Nagai, T. Norimatsu, H. Azechi, T. Yamanaka, Suppression of the Rayleigh-Taylor Instability due to Self-Radiation in a Multiablation Target, Phys. Rev. Lett. 92 (2004) 195001. https://doi.org/10.1103/PhysRevLett.92.195001.

[148] L. Masse, Stabilizing Effect of Anisotropic Thermal Diffusion on the Ablative Rayleigh-Taylor Instability, Phys. Rev. Lett. 98 (2007) 245001. https://doi.org/10.1103/PhysRevLett.98.245001.

[149] A. Sunahara, J.A. Delettrez, C. Stoeckl, R.W. Short, S. Skupsky, Time-Dependent Electron Thermal Flux Inhibition in Direct-Drive Laser Implosions, Phys. Rev. Lett. 91 (2003) 095003. https://doi.org/10.1103/PhysRevLett.91.095003.

[150] E. Ott, D.A. Russell, Diffuse-Boundary Rayleigh-Taylor Instability, Phys. Rev. Lett. 41 (1978) 1048–1051. https://doi.org/10.1103/PhysRevLett.41.1048.

[151] A.B. Bud'ko, M.A. Liberman, Suppression of the Rayleigh-Taylor instability by convection in ablatively accelerated laser targets, Phys. Rev. Lett. 68 (1992) 178–181. https://doi.org/10.1103/PhysRevLett.68.178.

[152] V. Lobatchev, R. Betti, Ablative Stabilization of the Deceleration Phase Rayleigh-Taylor Instability, Phys. Rev. Lett. 85 (2000) 4522–4525. https://doi.org/10.1103/PhysRevLett.85.4522.

[153] R. Betti, V.N. Goncharov, R.L. McCrory, C.P. Verdon, Self-consistent cutoff wave number of the ablative Rayleigh–Taylor instability, Physics of Plasmas. 2 (1995) 3844–3851. https://doi.org/10.1063/1.871083.

[154] H. Takabe, K. Mima, L. Montierth, R.L. Morse, Self-consistent growth rate of the Rayleigh–Taylor instability in an ablatively accelerating plasma, Phys. Fluids. 28 (1985) 3676. https://doi.org/10.1063/1.865099.

[155] J.F. Barnes, P.J. Blewett, R.G. McQueen, K.A. Meyer, D. Venable, Taylor instability in solids, Journal of Applied Physics. 45 (1974) 727–732. https://doi.org/10.1063/1.1663310.

[156] S.M. Gol'berg, A.L. Velikovich, Suppression of Rayleigh–Taylor instability by the snowplow mechanism, Physics of Fluids B: Plasma Physics. 5 (1993) 1164–1172. https://doi.org/10.1063/1.860974.

[157] C.M. Huntington, J.L. Belof, K.J.M. Blobaum, R.M. Cavallo, N.B. Kostinski, B.R. Maddox, H.-S. Park, C. Plechaty, S.T. Prisbrey, R. Rudd, D.W. Swift, R.J. Wallace, S.V. Weber, C. Wehrenberg, M.J. Wilson, B.A. Remington, Investigating iron material strength up to 1 Mbar using Rayleigh-Taylor growth measurements, in: Proceedings of the Conference of the American Physical Society Topical Group on Shock Compression of Condensed Matter, Tampa Bay, Florida, USA, 2017: p. 110007. https://doi.org/10.1063/1.4971670.

[158] V. Gandhi, S. Ravindran, G. Ravichandran, Dynamic Strength of Iron at High Pressures and Strain Rates, Phys. Rev. Lett. 128 (2022) 015705. https://doi.org/10.1103/PhysRevLett.128.015705.

[159] A.E. Gleason, W.L. Mao, Strength of iron at core pressures and evidence for a weak Earth's inner core, Nature Geosci. 6 (2013) 571–574. https://doi.org/10.1038/ngeo1808.

[160] Y. Ping, F. Coppari, D.G. Hicks, B. Yaakobi, D.E. Fratanduono, S. Hamel, J.H. Eggert, J.R. Rygg, R.F. Smith, D.C. Swift, D.G. Braun, T.R. Boehly, G.W. Collins, Solid Iron Compressed Up to 560 GPa, Phys. Rev. Lett. 111 (2013) 065501. https://doi.org/10.1103/PhysRevLett.111.065501.

[161] S. Merkel, S. Hok, C. Bolme, D. Rittman, K.J. Ramos, B. Morrow, H.J. Lee, B. Nagler, E. Galtier, E. Granados, A. Hashim, W.L. Mao, A.E. Gleason, Femtosecond Visualization of hcp-Iron Strength and Plasticity under Shock Compression, Phys. Rev. Lett. 127 (2021) 205501. https://doi.org/10.1103/PhysRevLett.127.205501.

[162] J. Lindl, Development of the indirect-drive approach to inertial confinement fusion and the target physics basis for ignition and gain, Physics of Plasmas. 2 (1995) 3933–4024. https://doi.org/10.1063/1.871025.

[163] J.D. Moody, D.A. Callahan, D.E. Hinkel, P.A. Amendt, K.L. Baker, D. Bradley, P.M. Celliers, E.L. Dewald, L. Divol, T. Döppner, D.C. Eder, M.J. Edwards, O. Jones, S.W. Haan, D. Ho, L.B. Hopkins, N. Izumi, D. Kalantar, R.L. Kauffman, J.D. Kilkenny, O. Landen, B. Lasinski, S. LePape, T. Ma, B.J. MacGowan, S.A. MacLaren, A.J. Mackinnon, D. Meeker, N. Meezan, P. Michel, J.L. Milovich, D.

Munro, A.E. Pak, M. Rosen, J. Ralph, H.F. Robey, J.S. Ross, M.B. Schneider, D. Strozzi, E. Storm, C. Thomas, R.P.J. Town, K.L. Widmann, J. Kline, G. Kyrala, A. Nikroo, T. Boehly, A.S. Moore, S.H. Glenzer, Progress in hohlraum physics for the National Ignition Facility, Physics of Plasmas. 21 (2014) 056317. https://doi.org/10.1063/1.4876966.

[164] B.A. Remington, H.-S. Park, D.T. Casey, R.M. Cavallo, D.S. Clark, C.M. Huntington, C.C. Kuranz, A.R. Miles, S.R. Nagel, K.S. Raman, V.A. Smalyuk, Rayleigh–Taylor instabilities in high-energy density settings on the National Ignition Facility, Proc Natl Acad Sci USA. 116 (2019) 18233–18238. https://doi.org/10.1073/pnas.1717236115.

[165] A. Krygier, P.D. Powell, J.M. McNaney, C.M. Huntington, S.T. Prisbrey, B.A. Remington, R.E. Rudd, D.C. Swift, C.E. Wehrenberg, A. Arsenlis, H.-S. Park, P. Graham, E. Gumbrell, M.P. Hill, A.J. Comley, S.D. Rothman, Extreme Hardening of Pb at High Pressure and Strain Rate, Phys. Rev. Lett. 123 (2019) 205701. https://doi.org/10.1103/PhysRevLett.123.205701.

[166] L.C. Chhabildas, J.W. Swegle, Dynamic pressure-shear loading of materials using anisotropic crystals, Journal of Applied Physics. 51 (1980) 4799–4807. https://doi.org/10.1063/1.328312.

[167] R.M. More, K.H. Warren, D.A. Young, G.B. Zimmerman, A new quotidian equation of state (QEOS) for hot dense matter, Phys. Fluids. 31 (1988) 3059. https://doi.org/10.1063/1.866963.

[168] D.A. Young, E.M. Corey, A new global equation of state model for hot, dense matter, Journal of Applied Physics. 78 (1995) 3748–3755. https://doi.org/10.1063/1.359955.

[169] G.I. Kerley, Multiphase equation of state for iron, 1993. https://doi.org/10.2172/6345571.

[170] C.J. Wu, LEOS 263, Unpublished. (2021).

[171] G. Shen, H. Mao, R.J. Hemley, T.S. Duffy, M.L. Rivers, Melting and crystal structure of iron at high pressures and temperatures, Geophys. Res. Lett. 25 (1998) 373–376. https://doi.org/10.1029/97GL03776.

[172] A.B. Belonoshko, T. Lukinov, J. Fu, J. Zhao, S. Davis, S.I. Simak, Stabilization of body-centred cubic iron under inner-core conditions, Nature Geosci. 10 (2017) 312–316. https://doi.org/10.1038/ngeo2892.

[173] Y. Ma, M. Somayazulu, G. Shen, H. Mao, J. Shu, R.J. Hemley, In situ X-ray diffraction studies of iron to Earth-core conditions, Physics of the Earth and Planetary Interiors. 143 (2004) 455–467.

[174] Y. Kuwayama, K. Hirose, N. Sata, Y. Ohishi, Phase relations of iron and iron–nickel alloys up to 300 GPa: Implications for composition and structure of the Earth's inner core, Earth and Planetary Science Letters. 273 (2008) 379–385. https://doi.org/10.1016/j.epsl.2008.07.001.

[175] S. Tateno, K. Hirose, Y. Ohishi, Y. Tatsumi, The Structure of Iron in Earth's Inner Core, Science. 330 (2010) 359–361. https://doi.org/10.1126/science.1194662.

[176] B. Branch, B.J. Jensen, Dynamic x-ray diffraction to study the shock-induced α-ε phase transition in iron, in: St. Louis, MO, USA, 2018: p. 040001. https://doi.org/10.1063/1.5044779.

[177] A. Denoeud, N. Ozaki, A. Benuzzi-Mounaix, H. Uranishi, Y. Kondo, R. Kodama, E. Brambrink, A. Ravasio, M. Bocoum, J.-M. Boudenne, M. Harmand, F. Guyot, S. Mazevet, D. Riley, M. Makita, T. Sano, Y. Sakawa, Y. Inubushi, G. Gregori, M. Koenig, G. Morard, Dynamic X-ray diffraction observation of shocked solid iron up to 170 GPa, Proc Natl Acad Sci USA. 113 (2016) 7745–7749. https://doi.org/10.1073/pnas.1512127113.

[178] J.A. Hawreliak, S.J. Turneaure, Probing the lattice structure of dynamically compressed and released single crystal iron through the alpha to epsilon phase transition, Applied Physics. (2021) 18.

[179] B. Yaakobi, T.R. Boehly, D.D. Meyerhofer, T.J.B. Collins, B.A. Remington, P.G. Allen, S.M. Pollaine, H.E. Lorenzana, J.H. Eggert, EXAFS Measurement of Iron bcc-to-hcp Phase Transformation in Nanosecond-Laser Shocks, Phys. Rev. Lett. 95 (2005) 075501. https://doi.org/10.1103/PhysRevLett.95.075501.

[180] S.J. Turneaure, S.M. Sharma, Y.M. Gupta, Crystal Structure and Melting of Fe Shock Compressed to 273 GPa: In Situ X-Ray Diffraction, PHYSICAL REVIEW LETTERS. (2020) 6.

[181] G. Morard, S. Boccato, A.D. Rosa, S. Anzellini, F. Miozzi, L. Henry, G. Garbarino, M. Mezouar, M. Harmand, F. Guyot, E. Boulard, I. Kantor, T. Irifune, R. Torchio, Solving Controversies on the Iron Phase Diagram Under High Pressure, Geophys. Res. Lett. 45 (2018). https://doi.org/10.1029/2018GL079950.

[182] S. Anzellini, A. Dewaele, M. Mezouar, P. Loubeyre, G. Morard, Melting of Iron at Earth's Inner Core Boundary Based on Fast X-ray Diffraction, Science. 340 (2013) 464–466. https://doi.org/10.1126/science.1233514.

[183] R. Boehler, Temperatures in the Earth's core from melting-point measurements of iron at high static pressures, Nature. 363 (1993) 534–536. https://doi.org/10.1038/363534a0.

[184] J. Li, Q. Wu, J. Li, T. Xue, Y. Tan, X. Zhou, Y. Zhang, Z. Xiong, Z. Gao, T. Sekine, Shock Melting Curve of Iron: A Consensus on the Temperature at the Earth's Inner Core Boundary, Geophys. Res. Lett. 47 (2020). https://doi.org/10.1029/2020GL087758.

[185] M. Harmand, A. Ravasio, S. Mazevet, J. Bouchet, A. Denoeud, F. Dorchies, Y. Feng, C. Fourment, E. Galtier, J. Gaudin, F. Guyot, R. Kodama, M. Koenig, H.J. Lee, K. Miyanishi, G. Morard, R. Musella, B. Nagler, M. Nakatsutsumi, N. Ozaki, V. Recoules, S. Toleikis, T. Vinci, U. Zastrau, D. Zhu, A. Benuzzi-Mounaix, X-ray absorption spectroscopy of iron at multimegabar pressures in laser shock experiments, Phys. Rev. B. 92 (2015) 024108. https://doi.org/10.1103/PhysRevB.92.024108.

[186] K.O. Mikaelian, Design of a Rayleigh–Taylor experiment to measure strength at high pressures, Physics of Plasmas. 17 (2010) 092701. https://doi.org/10.1063/1.3478987.

[187] J.F. Seely, G.E. Holland, L.T. Hudson, A. Henins, X-ray modulation transfer functions of photostimulable phosphor image plates and scanners, Appl. Opt. 47 (2008) 5753. https://doi.org/10.1364/AO.47.005753.

[188] J.L. Belof, R.M. Cavallo, R.T. Olson, R.S. King, G.T. Gray III, D. Holtkamp, S.-R. Chen, R.E. Rudd, N. Barton, A. Arsenlis, B. Remington, H.-S. Park, S.T. Prisbrey, P. Vitello, G. Bazan, K.O. Mikaelian, A.J. Comley, B. Maddox, M.J. May, Rayleigh-Taylor strength experiments of the pressure-induced α→ε→α′ phase transition in iron, in: Proceedings of the Conference of the American

Physical Society Topical Group on Shock Compression of Condensed Matter, Chicago, Illinois, 2012: pp. 1521–1524. https://doi.org/10.1063/1.3686572.

[189] H.-S. Park, R.E. Rudd, R.M. Cavallo, N.R. Barton, A. Arsenlis, J.L. Belof, K.J.M. Blobaum, B.S. El-dasher, J.N. Florando, C.M. Huntington, B.R. Maddox, M.J. May, C. Plechaty, S.T. Prisbrey, B.A. Remington, R.J. Wallace, C.E. Wehrenberg, M.J. Wilson, A.J. Comley, E. Giraldez, A. Nikroo, M. Farrell, G. Randall, G.T. Gray, Grain-Size-Independent Plastic Flow at Ultrahigh Pressures and Strain Rates, Phys. Rev. Lett. 114 (2015) 065502. https://doi.org/10.1103/PhysRevLett.114.065502.

[190] E.M. Bringa, C.J. Ruestes, Private communication, 2020.